

# **ON-CHIP NANOPHOTONIC STRUCTURES FOR BIOSENSING DEVICES**

**A THESIS**

*Submitted in partial fulfilment of the  
requirements for the award of degree*

*of*

**DOCTOR OF PHILOSOPHY**

By

**SULABH**

**Under the guidance of:**

**Dr. Mukesh Kumar**



**DISCIPLINE OF ELECTRICAL ENGINEERING  
INDIAN INSTITUTE OF TECHNOLOGY INDORE**

**April 2021**





## INDIAN INSTITUTE OF TECHNOLOGY INDORE

### CANDIDATE'S DECLARATION

I hereby certify that the work which is being presented in the thesis entitled **On-Chip Nanophotonic Structures For Biosensing Devices** in the partial fulfilment of the requirements for the award of the degree of **Doctor Of Philosophy** and submitted in the **Discipline Of Electrical Engineering, Indian Institute of Technology Indore**, is an authentic record of my own work carried out during the time period from **March 2016 to April 2021** under the supervision of **Dr. Mukesh Kumar**, Associate Professor, Electrical Engineering IIT Indore and **Dr. Suchandan Pal**, Sr Principal Scientist, CEERI Pilani,

The matter presented in this thesis has not been submitted by me for the award of any other degree of this or any other institute.

*Sulabh*  
09/04/2021

Signature of the student with date  
(Sulabh)

-----  
-----  
This is to certify that the above statement made by the candidate is correct to the best of our knowledge.

*Mukesh Kumar*

(09/04/2021)

Signature of Thesis Supervisor #1 with date  
(**Dr. Mukesh Kumar**)

*Suchandan Pal*

(12/04/2021)

Signature of Thesis Supervisor #2 with date  
(**Dr. Suchandan Pal**)

-----  
**Sulabh** has successfully given his/her Ph.D. Oral Examination held on

Signature of Chairperson (OEB)  
Date:

Signature of External Examiner  
Date:

Signature(s) of Thesis Supervisor(s)  
Date:

Signature of PSpC Member #1  
Date:

Signature of PSpC Member #2  
Date:

Signature of Convener, DPGC  
Date:

Signature of Head of Discipline  
Date:

## ACKNOWLEDGEMENTS

I would like to express my deep sense of gratitude to my supervisor **Dr. Mukesh Kumar** for his outstanding mentorship and support provided throughout these years. Under his guidance and encouragement, I successfully surpassed many difficulties and learned a lot.

I am extremely grateful to my co-supervisor **Dr. Suchandan Pal**, Sr Principal Scientist, CEERI Pilani and doctoral committee members **Prof. Vimal Bhatia** and **Dr. Bhupesh K Lad** for giving me valuable advice on my research and kindly going through my dissertation.

I would like to thank Electron microscopy lab at **RRCAT** Indore, **SIC** at IIT Indore and **Optoelectronics Lab, CEERI Pilani** for providing partial technical support, characterization, and fabrication facilities. I would like to thank the **Hybrid Nanodevice Research Group (HNRG)** for their partial technical support with characterization equipment.

I would like to thank my colleagues and friends including **Lalit Singh, Sourabh Jain, Vishal Kaushik, Swati Rajput, Suresh Pandey, Rahul Dev Mishra and Prem Babu** for their moral support, best wishes, and unforgettable days we spent together. I am grateful to all of you for providing a stimulating and fun environment.

I am thankful to **my beloved wife Gaelle** for her continuous moral support during this journey.

Last, but far from least, I must thank to my father **Mr. Sudhir Kr. Srivastava**, my mother **Smt. Kiran Srivastava** and my sister **Siddhi**, for their love and support throughout this journey. I owe a lot to them.

*Dedicated to  
My Dear Mother & Father*

## List of Publications

### (A) Publications from PhD thesis work

#### Patent

1. **Sulabh**, et.al, “A biochemical sensor with engineered nanophotonic structure, the process of preparation and use thereof”, patent is filed.

#### A1. Published in journals for PhD work:

1. **Sulabh**, Vishal Kaushik, Lalit Singh, Swati Rajput, Mukesh Kumar,” Nanophotonic Waveguide based on Engineered Horizontal-vertical Slots for Polarization Independent Biochemical Sensing”, **J. Opt. Soc. Am. B** 38, 749-757 (2021) **(IF 2.180)**
2. **Sulabh**, Lalit Singh, Sourabh Jain, Mukesh Kumar, “Nanophotonic Device based on Fano Resonance in Engineered Slot Waveguide for Optical Detection of Viral Infections” **IEEE Sensors Journal**, vol. 21, no. 3, pp. 2805-2812, 1 Feb.1, 2021 **(IF 3.076)**.
3. **Sulabh**, Singh, L., Jain, S., Kumar, M. “Optical Slot Waveguide with Grating-Loaded Cladding of Silicon and Titanium Dioxide for Label-Free Bio-Sensing” **IEEE Sensors Journal**, vol. 19, no. 15, pp. 6126-6133, 1 Aug.1, 2019. **(IF 3.076)**
4. **Sulabh**, Lalit Singh, Vishal Kaushik, Swati Rajput, Sourabh Jain, Manoj. K. Pal, Mukesh Kumar” Electrically controlled nanophotonic slot structure based on photocatalytic nanocomposite for optical detection of foodborne pathogens” **Journal of Lightwave Technology**, under review, 2021 **(IF 4.162)**

## **B1. Other publication in journals during PhD**

1. V. Kaushik, S Rajput, Sulabh, S. Jain, L. Singh, and M. Kumar, “Efficient Sub-bandgap Photodetection via Two-dimensional Electron Gas in ZnO Based Heterojunction,” **Journal of Lightwave Technology**, 2020. (IF 4.162)
2. S. Jain, Sulabh, S. Rajput, L. Singh, P. Tiwari, A. Shrivastava, and M. Kumar, “Thermally stable optical filtering using silicon-based comb-like asymmetric grating for sensing applications,” **IEEE Sensors Journal**, vol.20(7) pp.3529-3535, 2020. (IF 3.076)
3. Sourabh Jain, Swati Rajput, Vishal Kaushik, Sulabh, Mukesh Kumar “Efficient Optical Modulation with High Data-rate in Silicon Based Laterally Split Vertical p-n Junction,” **IEEE Journal of Quantum Electronics** PP(99):1-1 (Impact factor: 2.75)

## **A2. Published in proceedings for PhD work:**

1. Sulabh, M. Kumar, “Slot waveguide with grating based cladding for protein detection”, International Conference on Optics & Electro-Optics (ICOL), Dehradun, 2019.
2. Sulabh, L. Singh, S. Tidke and M. Kumar, "Metal assisted slot waveguide biochemical sensor," 3rd International Conference on Microwave and Photonics (ICMAP), Dhanbad, 2018.
3. Sulabh, Mukesh Kumar, “Optical Slot Waveguide Based On Photonic-Plasmonic Structure For Biosensing Applications” Conference on OSA Biophotonics Congress: Optics in the Life Sciences, accepted, British Columbia, Canada, 2021

## **B2. Other publication in proceedings during PhD:**

1. L. Singh, S. Jain, Sulabh and M. Kumar, “Loss Compensation in Hybrid Plasmonic Waveguide by Controlled Electron Injection,” International Conference on Optics & Electro-Optics, **ICOL-2019**, DRDO Dehradun.
2. L. Singh, P. Babu, Sulabh, S. Rajput and M. Kumar, “Optical Resistive Switch with High Extinction Ratio Using Plasmonic Amplification,” Conference on Laser and Electro-Optics **CLEO-PR-2020**, Sydney, Australia.

## TABLE OF CONTENTS

|                           |       |
|---------------------------|-------|
| TITLE PAGE.....           | i     |
| DECLARATION PAGE.....     | iii   |
| ACKNOWLEDGEMENT.....      | iv    |
| DEDICATION PAGE.....      | v     |
| LIST OF PUBLICATIONS..... | vi    |
| TABLE OF CONTENTS.....    | ix    |
| LIST OF FIGURES.....      | xii   |
| LIST OF TABLES.....       | xxiv  |
| ACRONYMS.....             | xxv   |
| NOMENCLATURE.....         | xxvi  |
| ABSTRACT.....             | xxvii |

### **Chapter 1: Optical Biosensing Technology.....1**

|     |   |    |
|-----|---|----|
| 1.1 | Biosensors.....                             | 1  |
|     | 1.1.1 Operating Principle.....              | 1  |
|     | 1.1.2 Classification of Biosensors.....     | 3  |
| 1.2 | Configuration of Optical Biosensor.....     | 5  |
|     | 1.2.1 Optical Sources.....                  | 5  |
|     | 1.2.2 Label or Label-Free.....              | 6  |
|     | 1.2.3 Biorecognition Elements.....          | 7  |
|     | 1.2.4 Detectors.....                        | 7  |
| 1.3 | Sensor Performance Metrics.....             | 8  |
|     | 1.3.1 Evanescent Field.....                 | 8  |
|     | 1.3.2 Polarization in Silicon.....          | 9  |
|     | 1.3.3 Sensing Parameters.....               | 10 |
| 1.4 | Label Free Optical Biosensors.....          | 12 |
|     | 1.4.1 Surface Plasmon Resonance.....        | 12 |
|     | 1.4.2 Ring Resonators.....                  | 13 |
|     | 1.4.3 Subwavelength Grating Resonators..... | 15 |
|     | 1.4.4 Mach Zander Interferometer.....       | 16 |

|                   |   |           |
|-------------------|---|-----------|
| 1.5               | Nanomaterials for Optical Biosensing.....   | 17        |
| 1.6               | Organization of Thesis.....   | 19        |
| <br>              |   |           |
| <b>Chapter 2:</b> | <b>Nanophotonic Waveguides for Sensing Applications.....</b>                          | <b>22</b> |
| 2.1               | Optical Slot Waveguides.....  | 22        |
| 2.2               | Slot waveguide with Subwavelength Grating Configuration.....                          | 28        |
| 2.3               | Hybrid Plasmonic Waveguides.....  | 32        |
| 2.3.1             | Figure of Merit.....  | 35        |
| 2.4               | Fano Resonance in Periodic Structures.....  | 36        |
| 2.5               | Food Pathogen Detection with Nanocomposites.....                                      | 42        |
| 2.6               | Thesis Objective and Contribution.....  | 45        |
| <br>              |   |           |
| <b>Chapter 3:</b> | <b>Optical Slot Waveguide for detection of Hepatitis B..</b>                          | <b>46</b> |
| 3.1               | Slot Waveguide Based on Grating-Loaded Cladding of Silicon and TiO <sub>2</sub> ..... | 46        |
| 3.2               | Proposed Device Design.....   | 49        |
| 3.3               | Analysis of Deposited Layers.....   | 50        |
| 3.4               | Transmission and Sensing Characteristics.....   | 54        |
| 3.5               | Fabrication Tolerance.....  | 58        |
| 3.6               | Summary.....  | 61        |
| <br>              |   |           |
| <b>Chapter 4:</b> | <b>Engineered Slot Waveguide for Optical Detection of Viral Infections.....</b>       | <b>63</b> |
| 4.1               | Generation of Fano Resonance.....   | 63        |
| 4.2               | Nanophotonic Engineered Slot Waveguide.....   | 65        |
| 4.3               | APTMS Functionalization and Susceptibility.....                                       | 68        |
| 4.4               | Propagation Characteristics.....  | 70        |
| 4.5               | Bulk and Surface Sensing Characteristics.....   | 73        |
| 4.6               | Summary.....  | 81        |

|   |            |
|---|------------|
| <b>Chapter 5: Double Slot Hybrid Plasmonic Waveguide for Biosensing.....</b>                            | <b>83</b>  |
| 5.1 Plasmonic-Photonic Slot Waveguide.....  | 83         |
| 5.2 Engineered Horizontal and Vertical Slot Structure....   | 85         |
| 5.3 Modal Characteristics.....  | 88         |
| 5.4 Bulk and Surface Sensing.....   | 91         |
| 5.5 DNA Hybridization and detection of viral infection...   | 99         |
| 5.6 Summary.....  | 104        |
| <br>  |            |
| <b>Chapter 6: Label Free Nanocomposite Film Biosensor for E. coli Detection.....</b>                    | <b>105</b> |
| 6.1 Nanocomposite for Pathogen Detection.....   | 105        |
| 6.2 Film Preparation and Functionalization.....   | 108        |
| 6.3 Film Morphological Characteristics.....   | 110        |
| 6.4 Ellipsometry Characteristics.....   | 114        |
| 6.5 Photocurrent Sensing Characteristics.....   | 116        |
| 6.6 Summary.....  | 120        |
| <br>  |            |
| <b>Chapter 7: Electrically Controlled Nanocomposite Slot Waveguide for Food Pathogen Detection.....</b> | <b>122</b> |
| 7.1 Detection of Food Borne Pathogen.....   | 122        |
| 7.2 Slot Waveguide Design.....  | 124        |
| 7.3 Fabrication of Slot Waveguide.....  | 126        |
| 7.4 Morphological Characteristics of Nanocomposite...   | 127        |
| 7.5 Photocatalytic Degradation.....   | 131        |
| 7.6 Sensing Characteristics.....  | 133        |
| 7.7 Microfluidic Channel.....   | 139        |
| 7.8 Summary.....  | 140        |
| <br>  |            |
| <b>Chapter 8: Conclusion and Future Scope.....</b>  | <b>142</b> |
| <br>  |            |
| <b>References.....</b>  | <b>145</b> |

## LIST OF FIGURES

| <b>Figure No.</b>  | <b>Caption</b>   | <b>Page No.</b> |
|--------------------|--|-----------------|
| <b>Figure 1.1</b>  | Major components of a biosensor  | 2               |
| <b>Figure 1.2</b>  | Classification of biosensors based on constructive strategies for detection methods  | 3               |
| <b>Figure 1.3</b>  | Configuration of optical biosensor   | 5               |
| <b>Figure 1.4</b>  | (a) Evanescent field in the silicon waveguide (b) Propagation and interaction with analytes of evanescent field in waveguide.  | 8               |
| <b>Figure 1.5</b>  | The electric field and power density profile for the x, y and z direction for the TE mode.   | 9               |
| <b>Figure 1.6</b>  | The electric field and power density profile for the x, y and z direction for the TM mode.   | 9               |
| <b>Figure 1.7</b>  | (a) Wavelength shift for the resonator (b) Spectral shift as a function of refractive index.   | 10              |
| <b>Figure 1.8</b>  | (a) For bulk sensitivity, cladding medium refractive index and concentration is varied. (b) For surface sensitivity, the layer of thickness 't' and density of analyte adsorbed is varied. | 10              |
| <b>Figure 1.9</b>  | (a) Schematic of SPR biosensor based on Krestchman configuration (b) LSPR configuration  | 12              |
| <b>Figure 1.10</b> | Ring resonator configuration (a) off resonance (b) on resonance  | 14              |
| <b>Figure 1.11</b> | (a) 3D view of a straight SWG waveguide without top cladding on SOI chip.  | 15              |

|                    |   |    |
|--------------------|---|----|
| <b>Figure 1.12</b> | Propagation and confinement of optical mode in SWG waveguide.   | 16 |
| <b>Figure 1.13</b> | Mach-Zander interferometer configuration with reference arm and sensing arm.  | 17 |
| <b>Figure 2.1</b>  | (a) Schematic of the slot waveguide. Strip width $W_s$ , strip height $h_s$ , strip refractive index $n_h$ , slot width $W_g$ and slot refractive index $n_l$ are shown. (b) Electric field profile of the TE eigenmode in slot-waveguide at 1550 nm. | 22 |
| <b>Figure 2.2</b>  | Electric field fundamental TE mode of the slot waveguide with silicon as high refractive index material and $\text{SiO}_2$ as bottom cladding. Slot width vary from 50 nm to 200 nm with the thickness of silicon at 220 nm.                          | 23 |
| <b>Figure 2.3</b>  | Schematic of silicon nitride slot waveguide-based ring resonator. (b) Schematic cross-section of slot waveguide.  | 25 |
| <b>Figure 2.4</b>  | Schematic of silicon slot-waveguide-based ring Resonator in silicon on insulator. Top cladding is filled with analyte solution.   | 25 |
| <b>Figure 2.5</b>  | Schematics of (a) 3D single-slot microring with asymmetric rib width (b) 3D double-slot microring with a narrow centre silicon rib.   | 26 |
| <b>Figure 2.6</b>  | Schematic of multi slot-waveguide-based ring Resonator in silicon on insulator. The rib width and slot width is 100 nm each respectively.   | 27 |
| <b>Figure 2.7</b>  | (a) Schematic of SWG waveguide (b) SEM picture of one fabricated ring on SOI chip. Ring radius is 10 $\mu\text{m}$ and SWG period is 250 nm   | 29 |
| <b>Figure 2.8</b>  | (a) Electric field intensity of TE mode in the slot region. (b) A 3D schematic of a slot-waveguide  | 30 |

|                    |   |    |
|--------------------|---|----|
|                    | Bragg grating in fluidic channel.   |    |
| <b>Figure 2.9</b>  | 3D structure of a subwavelength grating slot waveguide. The period, silicon width and slot width are kept at 200 nm, 300 nm and 100 nm.   | 30 |
| <b>Figure 2.10</b> | The schematic of the proposed SWGRTR with slot width of 80 nm and period is 200 nm.. (b) The optical mode confinement in different areas in proposed waveguide.   | 31 |
| <b>Figure 2.11</b> | (a) Schematic of the hollow hybrid plasmonic waveguide with Au layer. (b) Transmission responses of the fabricated MZI structure with a 20 $\mu\text{m}$ hollow HP waveguide infiltrated with different concentrations of IPA.  | 33 |
| <b>Figure 2.12</b> | Cross-section view of the DSHP waveguide covered by test liquid. (b) Mode profile of the DSHP waveguide, where $w_{\text{slot}} = 150\text{nm}$ , $w_{\text{Si}} = 165\text{nm}$ and $h_{\text{WG}} = 250\text{nm}$ . The covering material is 100% IPA   | 34 |
| <b>Figure 2.13</b> | Cross section of HPSW biosensor (b) Confinement in the slot regions for the suggested design at $\lambda = 1.55 \mu\text{m}$  | 35 |
| <b>Figure 2.14</b> | Schematic of the plasmonic-photonic MZI sensor . An Au-based metal stripe serves as the sensing element while a thermo-optic phase shifter and a variable optical attenuator (VOA) are implemented in the reference arm for tuning at the desirable wavelength and power balancing, respectively. | 36 |
| <b>Figure 2.15</b> | Normalized Fano profile for various values of the asymmetry parameter $q$ .   | 37 |
| <b>Figure 2.16</b> | (a) Schematic of the metasurface with one bus and one ring forming the one unit cell.. (b) Schematic of interference between the bright- and dark-mode resonators.  | 39 |

|                    |   |    |
|--------------------|---|----|
| <b>Figure 2.17</b> | Schematic of the dielectric metasurface composed of periodical asymmetric Si nano bar pairs (b) Top view and geometric parameters of a unit cell of the Si bar pairs.   | 39 |
| <b>Figure 2.18</b> | (a) A schematic of the silicon-based chiral metasurface supporting high-Q Fano resonances. (b) The SEM image of the fabricated sample and geometry definitions.   | 40 |
| <b>Figure 2.19</b> | (a) 3-D scheme of binary silicon nanodisk array with particle radii of 1 R and 2 R (b) top view of corresponding SEM image  | 41 |
| <b>Figure 2.20</b> | (a) Schematic of a silicon oligomer with six nanodisk of larger diameter surrounding the central smaller radius nanodisk (b) Electric field profiles at the positions of the main resonances  | 42 |
| <b>Figure 2.21</b> | Methods available for pathogen identification   | 43 |
| <b>Figure 3.1</b>  | Schematic of Grating loaded slot waveguide with overlay layer of TiO <sub>2</sub> . Inset optical mode confinement in slot region.  | 49 |
| <b>Figure 3.2</b>  | Side view of the proposed design with an overlay of 20-nm thick TiO <sub>2</sub> layer. $\Delta$ , Hr and d represents the period, total height and grating depth of the device respectively. Inset shows top view showing optical mode propagation in 100 nm wide slot region. | 50 |
| <b>Figure 3.3</b>  | Process flow for bottom cladding and silicon (a-d). from Fig. 3(e-h) are the process steps to be adopted in near future for the fabrication of final device.  | 51 |
| <b>Figure 3.4</b>  | (a) SEM image showing the interface surface Gold (100 nm thick) deposited by electron beam evaporation over SiO <sub>2</sub> . (b) SEM image of sol-gel derived TiO <sub>2</sub> , thin film grown on intrinsic Si <100> substrate.   | 52 |

|                    |  |    |
|--------------------|--|----|
| <b>Figure 3.5</b>  | (a) SEM image of APTMS over intrinsic Si <100> substrate. (b) SEM image of APTMS over TiO <sub>2</sub> after 3 hours of immersion in solution.   | 53 |
| <b>Figure 3.6</b>  | Simulated transmission spectra of the device with a 100 nm wide: black curve shows only slot waveguide with rib width of 400 nm and rib thickness of 220 nm; red curve shows grating on top of ribs beside slot region with a grating period of 300 nm and thickness of 100 nm; blue curve shows grating with 20 nm thick TiO <sub>2</sub> overlay.    | 55 |
| <b>Figure 3.7</b>  | Shift in resonant peak when refractive index of analyte changes by 0.02. The dotted line shows shift in the peak without TiO <sub>2</sub> overlay and solid line shows shift with TiO <sub>2</sub> overlay on the grating.   | 55 |
| <b>Figure 3.8</b>  | Simulated transmission spectra of the proposed device with TiO <sub>2</sub> overlay in which refractive index of analyte changes from 1.37 to 1.39. The grating period is kept 300 nm with slot width of 100 nm and with the thickness of 220 nm.  | 56 |
| <b>Figure 3.9</b>  | Variation in resonant wavelength with change in refractive index of the analyte. The refractive index is changed from 1.35 to 1.41 with an overall change of 0.06 which is common for bio-samples with various infections. The variation is observed with and without TiO <sub>2</sub> overlay with grating period of 300 nm and slot width of 100 nm. | 57 |
| <b>Figure 3.10</b> | Effect of variation of TiO <sub>2</sub> overlay thickness on the sensitivity of device. The grating period is kept at 300 nm with a slot width of 100 nm   | 59 |
| <b>Figure 3.11</b> | Effect of grating depth on the sensitivity with no TiO <sub>2</sub> overlay. The grating period and silicon rib width are 300 nm and 400 nm, respectively.   | 59 |

|                    |   |    |
|--------------------|---|----|
| <b>Figure 3.12</b> | Effect on resonant wavelength shift on variation of grating period with grating thickness of 100 nm, rib width of 400 nm and slot width of 100 nm.  | 60 |
| <b>Figure 3.13</b> | Effect of variation in silicon rib width on the sensitivity with (solid line) and without TiO <sub>2</sub> (dotted). The grating period is kept at 300 nm with a slot width of 100 nm.  | 61 |
| <b>Figure 4.1</b>  | Schematic of the proposed bio-sensor based on engineered slot waveguide device on SOI substrate. The silicon nano-disk radius, thickness and period are 175-nm, 220-nm and 500 nm respectively. Inset shows optical confinement in slot region  | 65 |
| <b>Figure 4.2</b>  | Electric field intensity of device with viral infection like HBsAg and without any sample. (c) Fano resonant mode propagation in 75 nm slot region  | 66 |
| <b>Figure 4.3</b>  | Side View of proposed device with a simple microfluidic channel.  | 66 |
| <b>Figure 4.4</b>  | Comparing $\partial n_{\text{eff}} / \partial t$ as the thickness of APTMS surface layer on proposed device with conventional slot waveguide.   | 68 |
| <b>Figure 4.5</b>  | SEM image of APTMS over intrinsic Si <100> substrate deposited after 3 hours of immersion in solution.  | 69 |
| <b>Figure 4.6</b>  | Simulated transmission spectra of Bragg grating (red) and Fano structure (black). For Bragg gratings waveguide the width and thickness is 350 nm and 220 nm with period of 500 nm and duty cycle is 60%. For Fano structure Nano-disk radius is 175 nm, grating width is 150 nm, slot width kept at 75 nm and period is 500 nm. | 70 |
| <b>Figure 4.7</b>  | Simulated transmission spectra of proposed device with variation in nano-disk radius from 150 nm to   | 72 |

200 nm. The grating width is kept constant at 150 nm with period of 500nm.

- Figure 4.8** Simulated transmission spectra of the proposed device with refractive index of analyte changes from 1.3377 to 1.3425. The grating period is kept 500 nm and with the thickness of 220 nm. Inset shows zoom in of resonance peaks. 74
- Figure 4.9** Simulated transmission spectra of the proposed device with nano-disk radius, grating width and slot width at 175 nm, 150 nm and 75 nm, in which refractive index of analyte changes from 1.38 to 1.44. The grating period is kept 600 nm and with the thickness. 75
- Figure 4.10** Variation in Fano resonant wavelength with the change in the analyte with different refractive index. The refractive index is changed from 1.38 to 1.44 with overall change of 0.02. The variation is observed with different nano-disk radius. Grating period and slot width kept at 150 nm and 75 nm. Inset shows the Fano peak shift with change in refractive index of 0.0008 for HBsAg sensing. 76
- Figure 4.11** Transmission spectra of proposed device with buffer, albumin and dextran added in albumin with 1% - 2% concentration. 79
- Figure 4.12** Transmission spectra with protein adlayer deposited on device and thickness is varied from 5 – 20 nm 80
- Figure 4.13** Effect of variation in nano-disk radius on the sensitivity. The grating period and grating width is kept at 500 nm and 150 nm. 80
- Figure 5.1** Schematic of nanophotonic double slot waveguide structure with gold clad. The rib width, thickness and slot width of device is 300 nm, 220 nm and 100 nm. Thickness of gold clad is 200 nm.  $S_v$  and  $S_H$  85

are the vertical and horizontal slot widths.

|                    |   |    |
|--------------------|---|----|
| <b>Figure 5.2</b>  | (a) and (b) Optical confinement for Ey field of TE mode and Ez field of TM mode of proposed device.   | 86 |
| <b>Figure 5.3</b>  | Electric field intensity in slot region for TE and TM mode  | 86 |
| <b>Figure 5.4</b>  | (a) Cross-section of proposed device with gold clad and buffer solution. (b) Cross-section of proposed device in buffer solution with adlayer integration   | 87 |
| <b>Figure 5.5</b>  | (a) and (b) Variation in effective refractive index with change in slot width for different rib width of double slot waveguide for TE mode and TM mode  | 89 |
| <b>Figure 5.6</b>  | (a) and (b) Variation in propagation loss with change in slot width for different rib width for TE mode.  | 90 |
| <b>Figure 5.7</b>  | Bulk and Surface sensitivity for TE and TM modes as a function of number of slots.  | 92 |
| <b>Figure 5.8</b>  | Bulk sensitivity for (a) TE mode and (b) TM mode with variation in rib width and for different slot widths.   | 93 |
| <b>Figure 5.9</b>  | Variation of the effective refractive index difference when adlayer thickness changes from 2 nm to 4 nm for TE and TM mode. The rib width is kept at 250 nm and slot width varies from 50 nm to 200 nm. | 95 |
| <b>Figure 5.10</b> | Figure of merit for bulk and surface sensing of proposed device for a wavelength range of 1500 nm to 1600 nm.   | 96 |
| <b>Figure 5.11</b> | (a) Schematic of nanophotonic double slot waveguide structure with grating in gold clad. (b) Optical confinement of TM mode for Ez field.   | 96 |

|                    |  |     |
|--------------------|--|-----|
| <b>Figure 5.12</b> | Bulk sensitivity in TM mode with grating and without grating for the variation of horizontal slot width.   | 97  |
| <b>Figure 5.13</b> | Variation in difference in neff of device with grating and without grating for change in vertical slot width.  | 97  |
| <b>Figure 5.14</b> | Variation in phase surface sensitivity of Protein A adlayer with change in horizontal slot width.  | 98  |
| <b>Figure 5.15</b> | FOM for bulk sensing and surface sensing in TM mode.   | 98  |
| <b>Figure 5.16</b> | (a-c) DNA hybridization processes. The film thickness (t) is fixed.  | 99  |
| <b>Figure 5.17</b> | Variation in effective refractive index difference in DNA hybridization for rib width of 250 nm and 300 nm with change in slot width. The rib thickness is kept at 220 nm. | 100 |
| <b>Figure 5.18</b> | Functionalization of Protein A, ssDNA, BSA and HBsAg antigen on substrate  | 101 |
| <b>Figure 5.19</b> | Variation in effective refractive index of proposed device for Protein A, ssDNA, BSA and HbsAg   | 102 |
| <b>Figure 5.20</b> | Phase surface sensitivity with all layers for HbsAg detection.   | 103 |
| <b>Figure 6.1</b>  | Schematic of prepared ITO/CZT film biosensor with functionalization of APTMS.  | 108 |
| <b>Figure 6.2</b>  | UV-Visible absorbance spectra of DH $\alpha$ E. coli bacterial cells for 10 <sup>5</sup> CFU/ml concentrations.  | 111 |
| <b>Figure 6.3</b>  | Absorbance spectra of sol gel derived nanocomposite CZT. Inset shows transmittance of  | 111 |

spin coated Cu-ZnO/TiO<sub>2</sub> (CZT) film on quartz substrate annealed at 500°C

|                    |  |     |
|--------------------|--|-----|
| <b>Figure 6.4</b>  | Photoluminescence spectra of ITO, CZT/ITO and functionalized ITO/CZT films deposited over quartz substrate.                                  | 112 |
| <b>Figure 6.5</b>  | SEM of sol gel derived nanocomposite CZT thin film over ITO film.  | 112 |
| <b>Figure 6.6</b>  | Energy dispersive analysis of X-ray (EDAX) spectra of CZT thin film deposited over glass substrate.  | 113 |
| <b>Figure 6.7</b>  | SEM of APTMS functionalization over CZT/ITO thin film.   | 114 |
| <b>Figure 6.8</b>  | Spectral response of the Ellipsometry parameters $\Delta$ for ITO thin film and CZT nanocomposite thin film over ITO film.                   | 115 |
| <b>Figure 6.9</b>  | Schematic diagram of band gap, conduction band potential and valence band potential in Cu-ZnO/TiO <sub>2</sub> under UV-VIS radiation.       | 116 |
| <b>Figure 6.10</b> | Photocurrent study of ITO, as prepared CZT/ITO thin film, functionalized top surface and after E. Coli concentration of 10 <sup>3</sup> CFU. | 118 |
| <b>Figure 6.11</b> | Photocurrent response of CZT/ITO film biosensor for varying concentration of E. Coli.  | 118 |
| <b>Figure 6.12</b> | Reproducibility study of CZT/ITO thin film sensor towards E. coli concentration variation  | 119 |
| <b>Figure 6.13</b> | Photocurrent response of CZT/ITO film biosensor  | 120 |
| <b>Figure 7.1</b>  | The schematic of the nanocomposite slot waveguide pathogen biosensor. Inset shows the electric field confinement in slot waveguide.          | 124 |

|                    |   |     |
|--------------------|---|-----|
| <b>Figure 7.2</b>  | Mode field distribution profile of photocatalytic nanocomposite slot waveguide.   | 125 |
| <b>Figure 7.3</b>  | The effect of variation in slot width on the confinement of optical mode is slot region and whole device  | 125 |
| <b>Figure 7.4</b>  | Process steps for the fabrication of slot waveguide   | 127 |
| <b>Figure 7.5</b>  | Bandgap transition energies of $\text{TiO}_2/\text{ZnO}$ and $\text{Cu-ZnO}/\text{TiO}_2$ using Tauc model.   | 128 |
| <b>Figure 7.6</b>  | Transmittance of CZT film deposited on the Pyrex glass substrate.   | 128 |
| <b>Figure 7.7</b>  | Photoluminescence spectra of $\text{ZnO}/\text{TiO}_2$ and $\text{Cu-ZnO}/\text{TiO}_2$ of nanocomposite material deposited on quartz substrate annealed at $500^\circ\text{C}$ .   | 129 |
| <b>Figure 7.8</b>  | Raman spectrum of nanocomposites thin films of $\text{ZnO}/\text{TiO}_2$ and $\text{Cu-ZnO}/\text{TiO}_2$ deposited on silicon substrate.   | 130 |
| <b>Figure 7.9</b>  | AFM morphology of $\text{Cu-ZnO}/\text{TiO}_2$ thin film spin coated on silicon substrate and calcined at $500^\circ\text{C}$ .   | 130 |
| <b>Figure 7.10</b> | UV-VIS absorption spectra of MO (Methyl Orange) with $\text{ZnO}/\text{TiO}_2$ , $\text{Cu-ZnO}/\text{TiO}_2$ nanocomposites solutions.   | 132 |
| <b>Figure 7.11</b> | Plot of $C/C_0$ with different irradiated time using nanocomposites solution under UV-VIS irradiation in 10 ml $\text{ZnO}/\text{TiO}_2$ , $\text{Cu-ZnO}/\text{TiO}_2$ nanocomposites solutions. Degradation of MO dye is shown dark orange solution (before irradiation) and light-yellow transparent nanocomposites solutions (after irradiation). | 132 |
| <b>Figure 7.12</b> | Experimental setup for E. coli sensor   | 133 |

|                    |  |     |
|--------------------|--|-----|
| <b>Figure 7.13</b> | Photocurrent of ZT and CZT slot waveguide when bias potential is applied.  | 134 |
| <b>Figure 7.14</b> | Photocurrent and dark current in CZT slot waveguide when bias potential is applied.  | 134 |
| <b>Figure 7.15</b> | Photocurrent variation as a function of voltage in ZnO/TiO <sub>2</sub> (ZT) nanocomposite with LB media and E. coli.  | 135 |
| <b>Figure 7.16</b> | Photocurrent variation as a function of voltage in Cu-ZnO/TiO <sub>2</sub> (CZT) nanocomposite with LB media and E. coli.                                    | 136 |
| <b>Figure 7.17</b> | Photocurrent response of CZT nanocomposite biosensor for varying concentration of E. Coli.   | 137 |
| <b>Figure 7.18</b> | Photocurrent response of CZT nanocomposite biosensor with E. coli and with mixed culture.  | 138 |
| <b>Figure 7.19</b> | 3D sketch of microfluidic channel over the slot waveguide. (b) Cross-section view of all layers in the sensing device (c) Dimension of microfluidic channel. | 139 |
| <b>Figure 7.20</b> | Process steps for fabrication of PDMS microfluidic channel   | 140 |

## LIST OF TABLES

| <b>Table No.</b> | <b>Caption</b>   | <b>Page No.</b> |
|------------------|--|-----------------|
| <b>Table 3.1</b> | Comparison of sensitivity (s) reported in various sensors                        | 58              |
| <b>Table 4.1</b> | Comparison of various reported nanophotonic biosensors with the proposed device. | 77              |
| <b>Table 6.1</b> | The weight% and atomic % of materials in CZT nanocomposite                       | 113             |

## ACRONYM

|                  |  |
|------------------|--|
| Ag               | <i>Silver</i>                                      |
| APTMS            | <i>3- Aminepropyltrimethoxysilane</i>              |
| Au               | <i>Gold</i>  |
| CFU              | <i>Colony Forming Unit</i>                         |
| Cu               | <i>Copper</i>                                      |
| CMOS             | <i>Complementary Metal Oxide<br/>Semiconductor</i> |
| CZT              | <i>Cu doped ZnO/TiO<sub>2</sub></i>                |
| DI               | <i>De-Ionized</i>                                  |
| DL               | <i>Limit of Detection</i>                          |
| EDX              | <i>Energy Dispersive X-ray<br/>Spectroscopic</i>   |
| eV               | <i>Electron Volt</i>                               |
| FDTD             | <i>Finite Difference Time Domain</i>               |
| FOM              | <i>Figure of Merit</i>                             |
| FWHM             | <i>Full Width Half Maximum</i>                     |
| HBsAg            | <i>Hepatitis B Antigen</i>                         |
| HPW              | <i>Hybrid Plasmonic Waveguide</i>                  |
| MZI              | <i>Mach Zander Interferometer</i>                  |
| MO               | <i>Methyl Orange</i>                               |
| ng               | <i>nanogram</i>                                    |
| NIR              | <i>Near Infra-Red</i>                              |
| PIC              | <i>Photonic Integrated Circuit</i>                 |
| pM               | <i>picomolar</i>                                   |
| RIU              | <i>Refractive index Unit</i>                       |
| SEM              | <i>Scanning Electron Microscopy</i>                |
| SOI              | <i>Silicon on Insulator</i>                        |
| SPP              | <i>Surface Plasmon Polariton</i>                   |
| TiO <sub>2</sub> | <i>Titanium dioxide</i>                            |
| UV               | <i>Ultraviolet</i>                                 |
| ZnO              | <i>Zinc Oxide</i>                                  |
| ZT               | <i>ZnO/TiO<sub>2</sub></i>                         |

## NOMENCLATURE

|            |                               |
|------------|-------------------------------|
| $\epsilon$ | <i>Dielectric Constant</i>    |
| $E_a$      | <i>Activation Energy</i>      |
| $m_0$      | <i>Electron Mass</i>          |
| $\lambda$  | <i>Wavelength</i>             |
| $h\nu$     | <i>Photon Energy</i>          |
| $E_c$      | <i>Conduction Band Energy</i> |
| $E_v$      | <i>Valance Band Energy</i>    |
| $g$        | <i>Energy Band gap</i>        |

# **ABSTRACT**

## **On-Chip Nanophotonic Structures for Biosensing Devices**

by

**Sulabh**

Optoelectronic Nanodevice Research Laboratory,  
Discipline of Electrical Engineering,  
Indian Institute of Technology Indore

Supervisor: Dr. Mukesh Kumar

Label-free optical biosensors which are capable of detecting small changes in the refractive index of analyte are widely used in viral disease detection, environmental monitoring, and biochemical application. Light can be confined in a high refractive index or low refractive index waveguide or by creating deformity states in a periodic structure. One of the finest examples of guiding light in low refractive index media is the slot waveguide which has been utilized to realize the number of photonic functionalities for a variety of applications. The grating waveguide supports a low-loss optical mode that propagates in the wave-guiding region and enhances the field overlaps with analytes and suppresses reflection. The optical detection method is based on a change in effective refractive index, a shift in narrow resonance peak and a change in photocurrent.

This dissertation focuses on the design, fabrication and characterization of engineered nanophotonic slot waveguides for applications in optical biosensors. The optical biosensor depends on the wavelength shift of the cavity and the sharpness of the resonant peak. The slot waveguide configuration explored includes one-dimensional silicon–air grating, a combination of dielectric and plasmonic waveguiding and nanocomposites. The introduction of silicon grating in the slot-based waveguide can enhance the sensitivity of the label-free biosensors. The waveguide grating usually composed

of silicon blocks or in disk shape are arranged in a periodic manner in the direction of propagation having a period smaller than the operating wavelength. By optimizing the pitch, width and duty cycle of the grating, the effective index of the medium can be engineered. The grating loaded nanophotonic waveguide is based on the introduction of grating with TiO<sub>2</sub> overlay on slot waveguide. The effect of TiO<sub>2</sub> as an overlay on the grating of the device is to enhance the sensitivity. The proposed device is numerically showing to detect principal marker of hepatitis-B viral infection, with a high sensitivity of 1200 nm/RIU with a figure of merit of 300. To improve the sensing performance the combination of nano-disk with a grating in engineered optical slot waveguide is designed for the detection of viral infections using Fano resonance. APTMS layer is synthesized as a functionalized layer to support the immobilization of antibodies to bind antigens. The proposed sensor device manifests bulk sensitivity of 1463 nm/RIU for 0.02 refractive index change of analyte and limit of detection of  $1.02 \times 10^{-3}$  RIU<sup>-1</sup>. The proposed device can detect the virus analytes with the smallest refractive index change of 0.0008 in serum medium.

To enhance the sensing performance, nanophotonic slot waveguides with subwavelength grating structures are designed on SOI technology. Due to the diffraction limit, the footprints of SOI waveguide devices cannot be decreased. To design more compact devices for subwavelength optical confinement hybrid plasmonic waveguide is designed. Hybrid plasmonic devices support the combination of photonic and plasmonic modes with confinement in the subwavelength region and relatively low losses. To confine optical mode in horizontal as well as vertical slot regions, a hybrid plasmonic waveguide was designed for polarization-independent bio chemical sensing. The bulk sensitivity in TM mode is increased by 1.5 times with gold cover compare to TE mode. The bulk sensitivity for TE and TM modes are reported to be 1.024 nm<sup>-1</sup> and 0.95 nm<sup>-1</sup> respectively. Surface sensitivity is investigated numerically for DNA hybridization and Hepatitis surface antigen detection.

Food borne bacterial pathogens are an important cause of a variety of human diseases. A biosensing platform with a high-throughput mechanism, free from complex fabrication processes and highly selective to bacterial contamination is required in medicine, food and water safety. Nanocomposite materials are synthesized for the development of optical biosensors because of their biocompatibility, tunable conduction characteristics and large surface area for adsorption of biomolecules. Cu ZnO/TiO<sub>2</sub> nanocomposite based photocatalytic biosensor is used in the detection of food borne pathogens due to their high stability and excellent charge transfer characteristics. The label-free photocurrent biosensing platform based on ITO/CZT nanocomposite thin film for the detection of E. coli in buffer was investigated. The biosensor is based on the interaction of E. coli with the functionalized surface of copper doped ZnO /TiO<sub>2</sub> (CZT) film over ITO thin film. A change of 20 μA is detected with a change in concentration of E. coli on the application of 4 volts. To improve the sensor performance a slot based nanophotonic structure with electric control based on photocatalytic nanocomposite is proposed to realize. The fabricated nanocomposite slot waveguide exhibits a measured photocurrent difference of 9 μA with E. coli in LB media solution. The limit of detection of E. coli bacteria concentrations is 5000 CFU/ml. The slot waveguide provides 10 times higher current density compared to thin film for the detection of food pathogens. The proposed methods carry a great potential for on-chip and off-chip nanoscale optical devices and sensors.



# Chapter 1

## Optical Biosensing Technology

Medical diagnostics play a crucial role in healthcare by providing early diagnosis of diseases, improving outcomes by taking appropriate care, targeted therapy and bring down healthcare costs. Diagnostic systems have been designed to fulfil all the requirements of a medical laboratory. The development of advanced biosensors is the most favourable approach to satisfy the increasing demand for effective medical diagnostic technologies [1]–[3]. Conventional diagnostic methods are like ELISA, culture-based, ATP bioluminescence, flow cytometry and PCR. To perform detection from these methods, follow certain steps like enrichment, serological verification, plating, and biochemical screening [4], [5]. These methods suffer from complexity, are time-consuming, required specific facilities, produce biological waste and are tedious. Early and rapid detection of diseases are required with high sensitivity to identify disease in the starting stage. New advancements in biosensors carry the potential in the early detection of diseases with high sensitivity and selectivity and their fast and low-cost methods [6]–[8]. By 2020, it is predicted that the global biosensors market size will reach USD 21.17 billion.

### 1.1 Biosensors

Biosensors are devices that measure a biological analyte, biomolecule or microorganism by generating a signal proportional to the concentration. Biosensors consist of the following parts: a bioreceptor that recognizes the analyte, a transducer that produces a signal, and a signal conditioning electronic circuitry.

#### 1.1.1 Operating Principle

The basic function of a biosensor is to generate a measurable signal which is proportional to the concentration of a substance (analyte). Fig. 1.1 shows the basic components of a biosensor. Biosensors are able to detect the biomolecules in a sample by converting the chemical or

physical signal to a desired output readout signal which can be further processed for analytical or graphical information [9], [10]. The biosensor can use various biological molecules as a bio-recognition element like enzymes, antibodies, nucleic acids, aptamers, receptors, whole cells, proteins and peptides of viruses [11].



*Figure 1.1. Major components of a biosensor*

The selection of these bio-recognition elements is important for the type of information is required and ease in deposition over devices or samples. The signal of interest generated by the bio-recognition event is interpreted and detected by the transducer, and the process of converting this signal into the recordable signal is called transduction[12]. The transducer converts the biophysical or biochemical signal into a recognizable physical signal also known as sensors.

Characteristics of a Biosensor:

1. **Linearity:** It is the accuracy of the measured signal. It is also related to the range of analyte concentration and resolution of the biosensor.
2. **Sensitivity:** It is the ratio between the output signal and the measured property. It is the highest response per unit analyte concentration.
3. **Selectivity:** The sensor response in the presence of other interfering chemicals or foreign materials. It is the minimal chemical interference with the target analyte. It should be able to detect a specific analyte in the solution.
4. **Stability:** It is the same response measured at the output of the sensor over a period of time. This shows the susceptibility of the sensor to disturbances in the biosensor system.

5. **Limit-of-detection:** The lowest quantity of a analyte that can be determined from the solution.

### 1.1.2 Classification of Biosensors

Based on the transduction mechanism, the biosensors are classified according to their construction, principle and type of response of the application. As is shown in Fig.1.2, light, electricity, heat, sound, and force, all these physical dimensions have been available to be used as the target property for developing a biosensor. Biosensors transduction mechanism is based on different operations have can both advantages and disadvantages to analyze various kinds of targets.

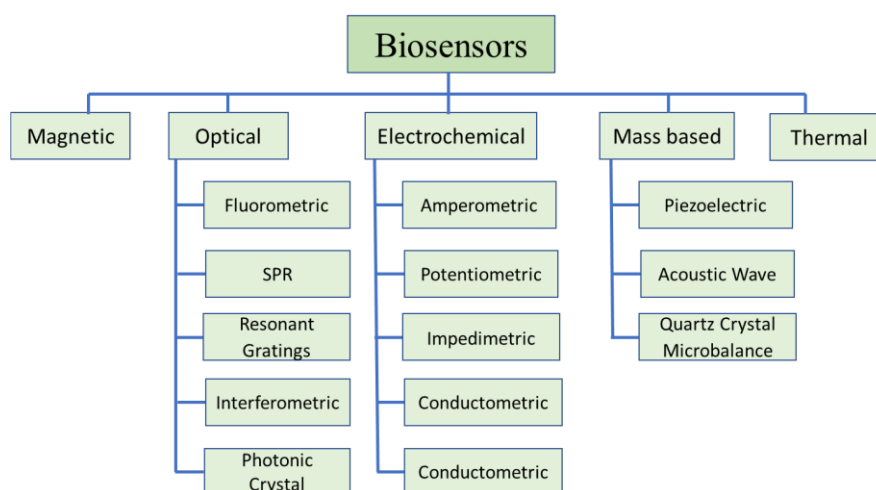


**Figure 1.2.** Classification of biosensors based on constructive strategies for detection methods.

The common type of transduction mechanisms are i) Electrochemical ii) mass-based and iii) Optical. The electrochemical transducer detects the change in current, voltage and resistance at the output. These changes could be positive or negative depending upon the type of properties of bio-recognition events [13]. Mechanical transducers are generally piezoelectric transducers that use piezoelectric effects to measure physical parameters like pressure, temperature, strain and acceleration and output is generated are usually an electrical signal proportional to input signal [14]. Piezoelectric biosensors are based on the principle that they can generate and transmit acoustic waves of

crystal oscillating at the natural resonance frequency. The decrease in resonant frequency signifies the increasing weight of layer on transducer surface depending on the interaction between biorecognition element and analyte. Mass-based sensors use cantilever or microbalance sensors which measures the change in force, stress, and deflection [15]. Optical biosensor works on the interaction of the optical field with the bio-recognition element, where a generated signal is translated into a measurable signal. It is based on the process of measuring photons rather than electrons.

Electrochemical and optical biosensors are used widely because of numerous possibilities of detection with high selectivity and sensitivity. Electrochemical sensors can be different types like amperometric, voltametric and potentiometric depending on the type of detection mechanism [16]. In electrochemical biosensors, the analyte interacts with the bio-recognition elements interacts or with enzymes that are attached to the sensor surface and produce a change in current, voltage or impedance at surface electrodes [17]. With the discovery of the photoelectric effect, photoelectrochemical sensors are developed. In a photoelectrochemical sensor, chemical energy is converted into an electrical signal when illuminated by a light source under applied bias [18]. Photovoltaics, photocatalysis and biosensing are the main applications. Photoelectrochemical sensors are capable to detect biomolecules by generating the photocurrent from oxidation-reduction reactions. It involves the charge separation and charge transfer reactions between photoactive material, analyte and electrodes when illuminated by light [19], [20].

Optical biosensors have exploited the interaction of analyte to the optical field. An optical biosensor integrates a bio-recognition element with a transducer and the optical signal observed is directly proportional to the concentration of the analyte [21]. Optical signal has properties like low noise, stability, low power and immunity to other disturbances makes it suitable for designing high sensitivity optical biosensors. Optical detection mechanism based on the reflectance, fluorescence, absorbance, luminescence, scattering and refractive

index through the spectral range of UV, visible and Infra-red regions. Fluorescence enhancement or quenching is produced by a fluorophore in the presence of the target molecule when it is excited at an adequate wavelength, typically in the blue or ultraviolet spectral regions. Surface plasmon resonance (SPR), fluorescence and optical waveguides utilize the evanescent field in close proximity to the biosensor surface to detect the interaction of the biorecognition element with the analyte.

## 1.2 Configuration of Optical Biosensor

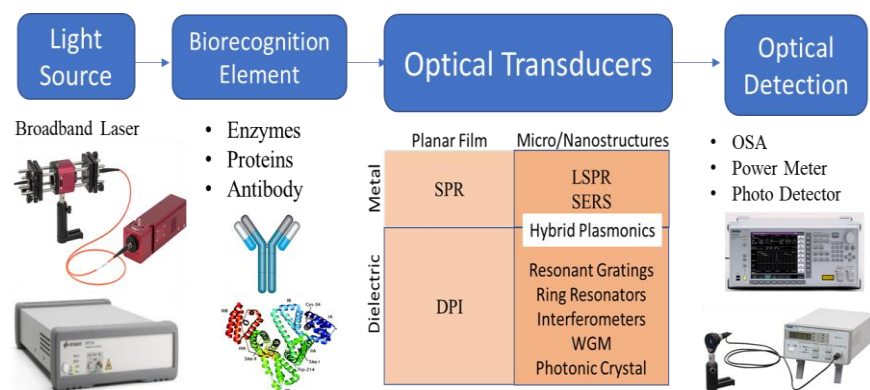


*Figure 1.3. Configuration of optical biosensor*

The basic objective of an optical biosensor is to produce a signal which is proportionate to the concentration of a measured substance (analyte). The SOI platform is appealing since it offers the potential of optical component integration onto the same substrate. The configuration of an optical biosensor is shown in Fig.1.3. The major components are a sensing unit and signal-transducing and processing units.

### 1.2.1 Optical Sources:

It is important to select the right optical source for illuminating or probing an optical biosensor. The optical source covers the spectral range from UV, visible to Infra-red regions depend on the type of transducer and material used in the sensing device. The optical source is either a continuous wave laser of fixed wavelength or a led laser source for broadband wavelength range. For high refractive index material waveguides like silicon, the optical source of fixed

wavelength should be in the telecommunication wavelength range of 1310 nm or 1550 nm where the propagation loss is very small [22]. Broadband laser sources can be used for absorbance, reflectance, fluorescence and transmission sensing strategies. The optical source should provide light with stable intensity with low background noise and should be compatible with optical fibres.

### **1.2.2 Label or Label-Free**

There are two types of optical biosensors employed in sensing i.e. label based detection method and label-free detection method. In label based sensing an extra biomolecule is covalently attached to the immobilized surface to enhance the quantitative signal. The optical signal generated by labels attached to the analyte can be fluorescent, luminescent and colorimetric. In general, a label is attached to analytes and upon optical excitation, the fluorescence emitted from labels is measured in terms of change in wavelength [23]. This method estimates the binding of analytes and recognizes the presence of a particular analyte. Irradiation by one optical wavelength excites the secondary wavelength at enzyme, dye molecule (chromophore) or fluorescent tag binding sites. The labelling process requires the selection and pairing of a sophisticated molecule or reagent to an analyte and also includes purification and synthesis of a reagent which affects the intrinsic properties of the target molecule or probes. The label-free optical biosensors use the property like refractive index and molecular weight for monitoring of target analyte and allowing more reliability with minimum assay development [24], [25]. Label-free biosensors do not require the use of a label to monitor the binding event.

### **1.2.3 Biorecognition Elements**

Enzymes are used to attach with specific biomolecules in affinity-based biosensors and enhances selectivity and sensitivity [26]. An enzyme is commonly used in biosensors to generate the local electron-hole donors, have a low shelf life, is very expensive and with low

stability. A common example of an enzyme is glucose oxidase which is used in amperometric based biosensors to detect glucose levels. Upon irradiation, the enzymes convert the specific bio-catalytic events into electrical signals when the semiconductor species interacts with the bio-catalyzed reaction chain [27]. Nucleic acid biosensors are also known as DNA sensors. These are more stable and highly selective to interact with complementary chains of polynucleotides [28]. Antibodies are large Y shape proteins used by immunosensors to attach with viruses and bacteria. The nature of antibodies is non-covalent with strong affinity [29]. Large antibodies like protein are covalently bound to one surface through a spacer like  $-\text{COOH}$ ,  $\text{NH}_2$ , isothiocyanate groups, or boronic acid. They form a covalent bond with thiol, amino groups or carboxyl groups of antibodies.

#### **1.2.4 Detectors**

Silicon and InP/InGaAs photodiodes are commonly used in different applications. The wavelength range of silicon photodiode is 950 nm and InP photodiodes work in the NIR range of 1.6  $\mu\text{m}$ . These photodiodes have high internal quantum efficiency to realize spectral responsivity. The important characteristics of a photodiode are response time which is characterized by FWHM, responsivity which is a ratio of current out to the detector to the incident optical power, and sensitivity which is defined as the optical power which generates an electrical signal equal to that due to noise of the diode. [30]. An Optical Spectrum Analyzer is a precision instrument to measure and display the distribution of power of an optical source over a specified wavelength span. It displays power on the vertical scale and the wavelength on the horizontal scale. It covers a wide range of wavelength from 700 nm to 1600 nm with a resolution between 0.1 nm and 5 nm. Ge-based PDs, however, have superior characteristics [31]. Recently [32] Ge on Si PDs with a high responsivity of 0.74 A/W and dark currents of 4 nA is reported.

### 1.3 Sensor Metrics

Various merits are used to evaluate the performance of a biosensor like sensitivity, selectivity, Q-factor, Full Width Half Maximum and detection of limit.

#### 1.3.1 Evanescent Field

For the SOI platform, silicon photonics biosensors rely on near infra-red light confined in the nanoscale region to sense molecular interactions. The portion of the light electric field travelling outside of the waveguide is called the evanescent field which interacts with the surrounding medium to create an external refractive index sensitive region as shown in Fig. 1.4 (a) and (b).

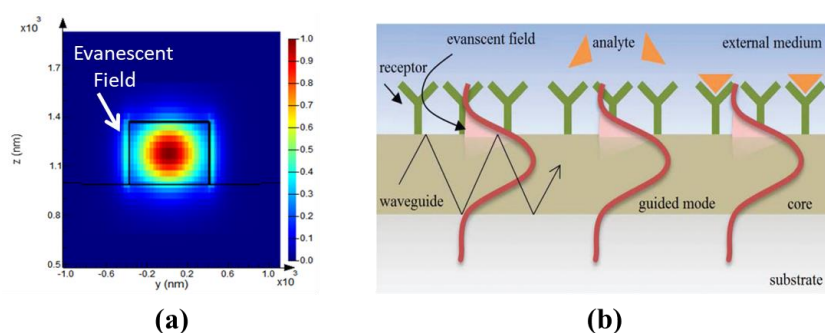


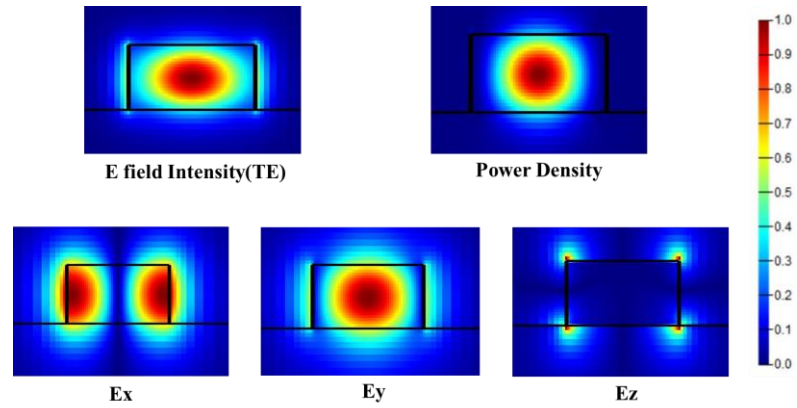
**Figure 1.4.** (a) Evanescent field in the silicon waveguide (b) Propagation and interaction with analytes of evanescent field in waveguide [33].

The principal detection method of optical biosensors is based on evanescent field detection. Within the evanescent field, receptors are already immobilized onto the surface of the waveguide and therefore it affects the guiding properties of the waveguide and the effective refractive index of the waveguide is shifted [33]. The variation of effective refractive index can be used for optical properties of waveguide like phase, amplitude and resonant momentum.

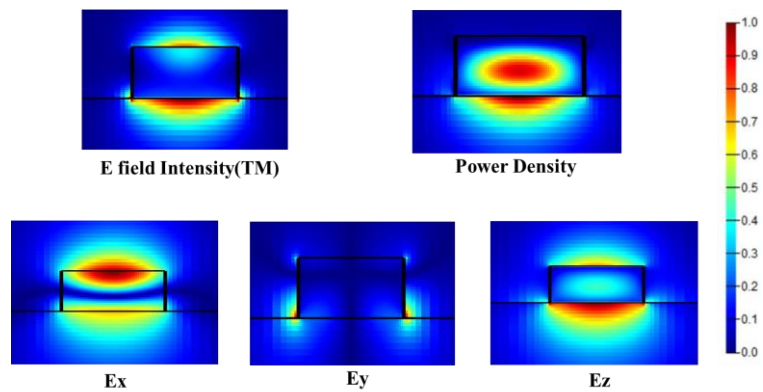
#### 1.3.2 Polarization in Silicon

Modal and polarization properties are two fundamental concern in waveguide design. Multimode waveguides are undesirable in optical communications as they cause interference which results in

degradation of device performance. The waveguide geometry of 500 nm x 220 nm two modes of different polarization can propagate with an effective index of 2.38 for TE mode and 1.58 for TM mode.



**Figure 1.5.** The electric field and power density profiles for the x, y and z direction for the TE mode.



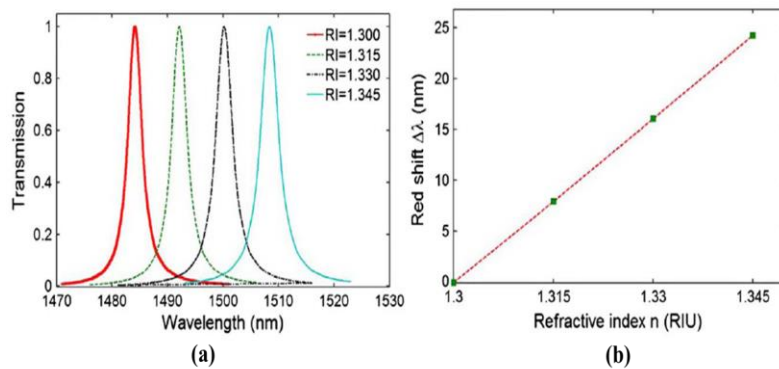
**Figure 1.6.** The electric field and power density profiles for the x, y and z direction for the TM mode.

Fig. 1.5 shows the electric field and power density profile of TE polarization in silicon waveguide and three electric field components. The TE mode propagates in the centre of the waveguide with strong interaction with sidewalls. Fig. 1.6 shows the electric field of TM mode for the same waveguide. While the TE mode propagates in the centre of the waveguide, the TM is much less confined in the centre and stretches in the vertical direction, which results in a lower effective refractive index. The TM mode strongly interacts with the upper and

lower cladding of the waveguide, so it is more affected by the silicon dioxide layer and by any metallic or semiconductor layer that is deposited on the top of the cladding.

### 1.3.3 Sensing Parameters

Sensitivity is determined by the strength of interaction between matter and evanescent field in an aqueous solution or at the sensor surface.



**Figure 1.7** (a) Wavelength shift for the resonator (b) Spectral shift as a function of refractive index [30].

It is variation in transduction magnitude measured as a function of the concentration of the target analyte. The magnitude is defined in terms of spectral position of resonance i.e transmission as a function of wavelength as in Fig.1.7 (a). It can be described as resonance displacement as a function of RIU change of the biosensor as in Fig.1.7 (b). There are two types of sensitivity defined in optical biosensing applications: bulk sensitivity and surface sensitivity.

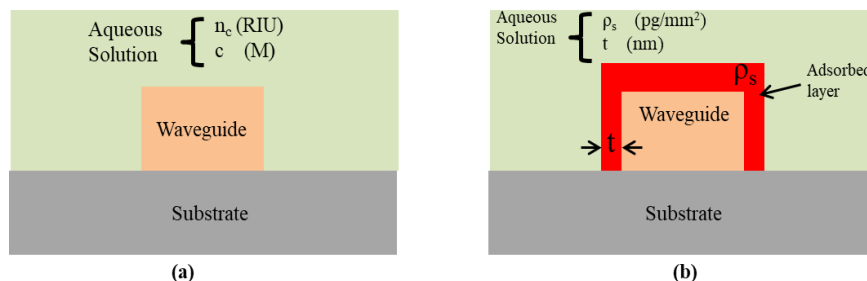


**Figure 1.8.** (a) For bulk sensitivity, cladding medium refractive index and concentration is varied. (b) For surface sensitivity, the layer of thickness 't' and density of analyte adsorbed is varied [35].

Bulk sensitivity takes account of change in cladding refractive index and defined as the ratio of change in effective refractive index for planar waveguide or change in resonant wavelength and the change in cladding refractive index as in Fig 1.8 (a).

$$S_{\text{bulk}} = \frac{\Delta\lambda_r}{\Delta n_c} \text{ or } \frac{\Delta n_{\text{eff}}}{\Delta n_c} \quad (1.1)$$

where  $\Delta\lambda_r$  is the change in resonant wavelength,  $n_c$  is the change in RI of the analyte solution, and  $n_{\text{eff}}$  is the effective refractive index [34]. Surface sensitivity defined as the ratio of the effective refractive index or change in resonant wavelength with respect to variation in the thickness of adsorbed molecular (adlayer) deposited over the sensor surface as shown in Fig. 1.8 (b).

$$S_{\text{surf}} = \frac{\Delta\lambda_r}{\Delta t} \text{ or } \frac{\Delta n_{\text{eff}}}{\Delta t} \quad (1.2)$$

where  $\Delta\lambda_r$  is the change in resonant wavelength,  $\Delta t$  is the change in thickness of adlayer over the sensor surface, and  $n_{\text{eff}}$  is an effective refractive index. The bulk and surface sensitivity are depending on the geometry of the sensing waveguide. The figure of Merit is defined by  $S/\text{FWHM}$  and Q factor calculated by  $Q = \lambda/\text{FWHM}$ , where FWHM is a full-width half maximum of the resonance spectrum. The detection limit defined as the minimum RI change necessary to cause a detectable change in the output signal.

The intrinsic detection of limit is defined by

$$iDL = \frac{\lambda}{Q * S} \quad (1.3)$$

where S is the bulk sensitivity, Q is a quality factor and  $\lambda$  is the resonant wavelength. [35] This is given in units for functionalization in ng/ml, pg/ml and for bulk sensing in RIU-1. This parameter gives information about the whole sensing process of refractometric process, functionalization of surfaces and affinity of biomolecular reaction.

## 1.4 Label-Free Optical Biosensors

Optical transducers are known as photonic biosensors. Over past decades many types of micrometre scale structures are fabricated on-chip on various materials like silicon, silicon nitride, gold and germanium for label-free optical detection. There are different types of label-free optical sensors are reported for biochemical applications based on planar film waveguide and nanostructures.

### 1.4.1 Surface Plasmon Resonance

The changes in evanescent field due to variation in the refractive index of the surrounding medium of the device are called evanescent field biosensors such as Surface Plasmon resonance sensors in Fig.1.9 (a). This optical technique measures the refractive index changes in the vicinity of thin metal layers (*i.e.*, gold or silver) in response to biomolecular interactions. SPR biosensors employ propagating surface plasmons that oscillate collectively on a planar metal-dielectric interface [36], [37].

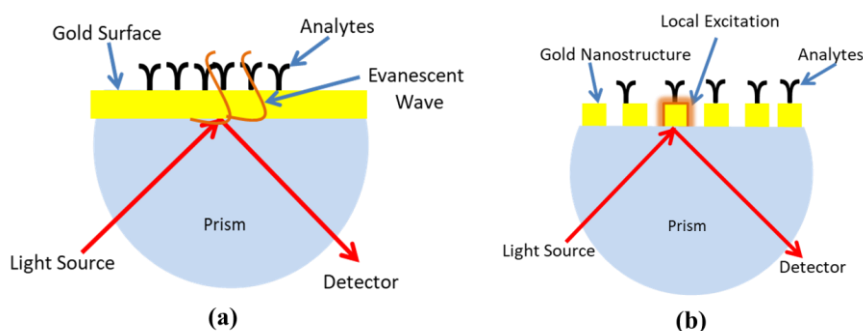


**Figure 1.9.** (a) Schematic of SPR biosensor based on Kretschman configuration (b) LSPR configuration [18]

Surface polaritons are the oscillations that occur when material vibrations interact with electromagnetics. Surface Plasmon polaritons can exist at a metal-dielectric interface and supported by TM mode [38]. When a metal surface *i.e.* gold is illuminated by polarized light with a specific angle surface SPR phenomenon occurs at the interface

of two dielectric media. After incidence an evanescent field at media couples through the electrons in the metal surface [11]. This generates surface plasmons and they propagate parallel through the surface. A portion of the reduced intensity of light is reflected at a specified angle known as reflectance angle which is proportional to the mass on the surface. New technological advancement in plasmonics sensing with miniaturization and multiplexing techniques is the use of sophisticated nanostructured metal films or nano-plasmonic structures which is smaller than the wavelength of incident light. In these nanoplasmonic structures, surface plasmons are confined in three-dimensional space inducing a non-propagating collective electron charge oscillation known as local surface plasmon resonance (LSPR) [21][39]. The local Surface polariton which is non-propagating surface polaritons is localized on the small region near particle surface and the local surface plasmon resonance property can be tailored by shape, size and material of nanostructure as shown in Fig. 1.9 (b) [40]. The local confinement provokes an increment in the EM field near nanostructures that rapidly decreases with distance and minimized susceptibility to disturbance produced by external media like temperature and enhances the sensitivity of very small analyte concentrations.

#### **1.4.2 Ring Resonators**

Ring resonators plays the important role in silicon photonics as silicon provides the high index contrast and miniaturization of photonic devices. A ring resonator consists of a circular looped optical waveguide and a bus waveguide as access waveguide which couples with circular loop waveguide as shown in Fig 1.10. Resonance condition appears when optical round trip length in circular waveguide is became equal to integer multiple of wavelength and maximum input optical power circulates in the optical loop ring waveguide. In case of no resonance all power transmits passes by through port[41], [42]. Resonant optical mode forms in ring resonator due to total internal reflections at the curved boundary. Ring resonators supports multiple resonances and spacing between the resonance peaks is called free

spectral range which depends on the resonator length of the sensor. A high extinction ratio is achieved when ring resonator achieved critical coupling between resonant cavity and waveguide bus.

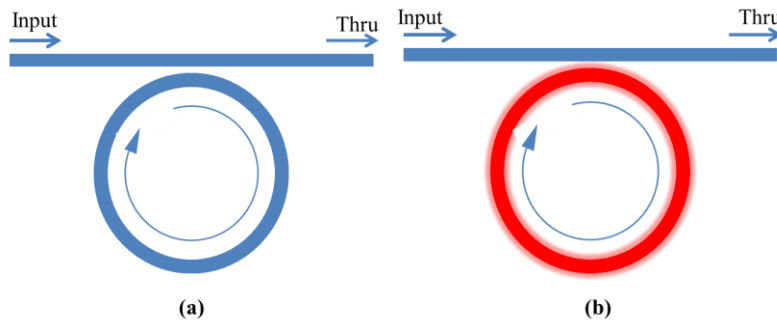


**Figure 1.10.** Ring resonator configuration (a) off resonance (b) on resonance [43]

Critical coupling is the condition when the power coupled to the ring is equal to the power loss in the ring. This coupling can be achieved by optimizing the gap between ring and waveguide [43]. Small dimensions of rings have the advantage of large FSR which is preferred in sensing applications. Thus for designing of compact ring resonator requires rings of small radius (few nanometres) which is possible by help of high contrast waveguides. The resonant wavelength of ring resonator is defined as  $\lambda = 2\pi r n_{\text{eff}}/m$ , where  $r$  is the radius of ring,  $n_{\text{eff}}$  is the effective refractive index of optical mode,  $m$  is the integer number. The resonant optical mode resonates around the circular ring has evanescent field of hundreds of nanometers which reaches into cladding medium and interacts with analytes near ring resonator surface.

The light analyte interaction length of the sensor is the physical length of device but in case of ring resonator creates very long effective length by the circulating nature of the resonant mode, which is defined by

$$L_{\text{eff}} = \frac{Q\lambda}{2\pi n} \quad (1.4)$$

where  $Q$  is the Quality factor,  $n$  is the refractive index of resonator and  $\lambda$  is the resonant wavelength [44]. For sensing applications, the surface of the ring should not cover by oxide which allows the evanescent wave to interact with external medium to detect any change in the refractive index. The  $Q$  factor is limited to 104 due to side wall scattering losses, bend radiation and mode mismatch, although highest  $Q$  factor are also reported. The advantage of ring resonator are high sensing performance due to more effective length, small footprint, high multiplexing capability and lower detection limit.

### 1.4.3 Sub Wavelength Grating Resonators

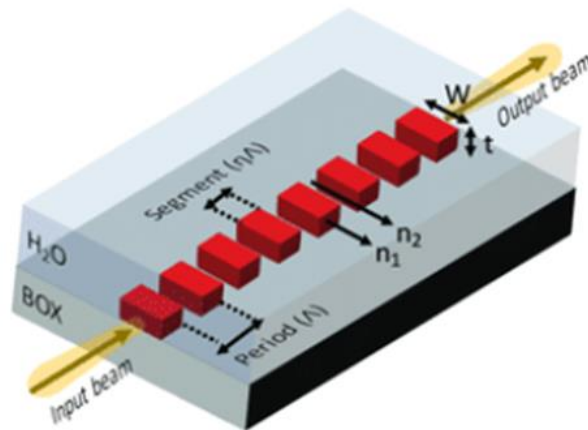


**Figure 1.11.** 3D view of a straight SWG waveguide without top cladding on SOI chip. [40]

To optimize the optical properties of planar waveguide, subwavelength grating was the introduced. The homogenous planar waveguide is divided into number of periodic silicon blocks as shown in Fig. 1.11. Subwavelength gratings are recognized by having a period  $\Lambda$ , that is sufficiently small than the wavelength of the incident light. The geometrical parameters to define subwavelength waveguide are width of silicon waveguide, silicon layer thickness, period and duty cycle [45]. The effective refractive index of the waveguide can be tailored by the subwavelength gratings. The period and duty cycle of the periodic arrangement can be optimized to adjust the effective refractive index for a given application. The duty cycle defines as DC

$= a/\Lambda$ . In SWG the silicon blocks are designed as small interleaving blocks (with length only few hundred nanometers) with air or SiO<sub>2</sub> as second refractive index material, so the waveguide core is made up of silicon and air. The optical properties of waveguide can be altered and tuned

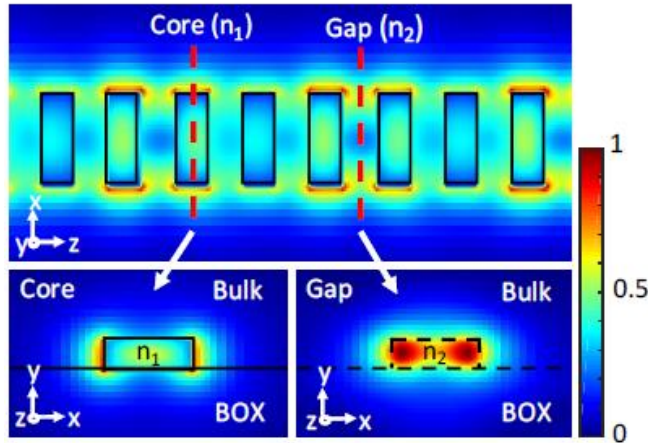


**Figure 1.12.** Propagation and confinement of optical mode in SWG waveguide [40].

by varying the filling fraction of two materials in one subwavelength period. The subwavelength grating waveguide support low-loss optical modes that propagates in the wave-guiding region and enhances the field overlaps with analytes and suppresses reflection [46]. The subwavelength waveguide operates in three regimes depending on the period and wavelength (i) subwavelength  $\Lambda < \lambda/2n_{\text{eff}}$  where period is small to suppress the effects of diffraction and waveguide operates as lossless waveguide, (ii) Bragg waveguide  $\Lambda = \lambda/2n_{\text{eff}}$ , where incoming light is reflected backwards completely (iii) and diffraction  $\Lambda > \lambda/2n_{\text{eff}}$  where light is scattered and gradually radiated in atmosphere as light propagates in periodic structure [47]. The wave propagates in subwavelength waveguide similar to conventional waveguide, but the interaction between light and analyte as cladding is greatly enhanced due to periodicity in waveguide as shown in Fig.1.12. The shape of electric field distribution of optical mode propagating in SWG changes periodically.

#### 1.4.4 Mach Zander Interferometer

In interferometric sensor the guided light is split by Y junction into two single mode waveguide arms, one arm is covered with analyte consider as sensing arm and other arm is without any sample is reference arm as

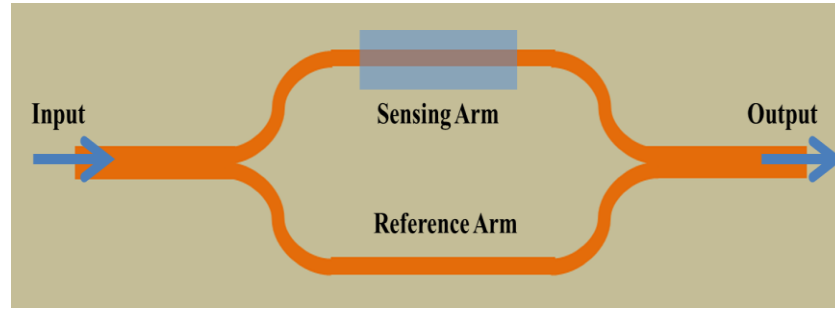


*Figure 1.13. Mach-Zander interferometer configuration with reference arm and sensing arm [48]*

shown in Fig.1.13. After travelling certain distance the single waveguides combine again by Y junction and constructive and destructive interference are recorded at output [48], [49]. The interferometer waveguide biosensors work on principle of phase shift in guided mode when mode in waveguide interacts with ambient cladding medium [48]. This phase change can be directly converted into change in output power detected by photodetector. The change in phase difference is calculated by

$$\Delta\Phi = \frac{2\pi L n_{eff}}{\lambda} \quad (1.5)$$

where,  $\lambda$  is the operating wavelength,  $n_{eff}$  is the difference in effective refractive index of two arms and  $L$  is the effective length of sensing arm. The effective length  $L$  is factor which improves sensitivity of a sensor. Different configurations with a variety of fabrication materials including  $\text{Si}_3\text{N}_4$  [50],  $\text{SiO}_2$  [51], and  $\text{Si}$  [52], were demonstrated with a detection of limit from  $10^{-2}$  to  $10^{-7}$  RIU. Chip-integrated interferometers have also shown the ability of biomolecule detection comparable limit of detection to the MZI sensor.

## 1.5 Nanomaterials for Biosensing

Technological advancement in different disciplines have provided the required techniques to work at nanoscale. Matter behaves differently in nanoscale than macroscale with new possibilities and properties. The size of nanomaterials is in range of 1 to 100nm. The properties of nanomaterial are that they have large surface-to-volume ratio, the different shapes, composition and binding characteristics [53]. The broad possibilities and applications of nanomaterials in improving the existing technologies are confirmed by many researchers. Major applications of nanomaterials are like energy conversion and storage, catalysis, optical sensors, signal amplification, heavy metal detection immobilization of biomolecules, as mediators, amplification of signal, detection nanoprobe and electroactive species [16]. Depending on the transducer operation such as optical, electrochemical, thermoelectric, etc. in biosensors, nanomaterials are being utilized. Nanomaterial's compositions are like single material, core-shell alloys, metals, carbon-based particles and polymers [54]. The properties shown by nanomaterials can be tuned by changing parameters of the nanoparticles such as: size, shape and composition.

Nanomaterials can be defined as 0-D where dimension of nanomaterials exist in nanoscale like nanoparticles of gold, platinum or quantum dots. Nanomaterial in 1-D are which have one direction in macroscale and other in nanoscale like nanofibers, nanorods and nanotubes. 2-D have two dimensions in macroscale and one in nanoscale like nanofilms, nanosheets and nano walls and 3-D are the bulk materials [16]. New functionalities and properties can be developed in nanoparticles by modifying different chemical and biological molecules on the surface [55]. Nanomaterials such as nanorods, nanoparticles, nanosheets and 3D-nanostructures have demonstrated remarkable advantages in sensing applications. Recent advancements in nanotechnology have enabled new techniques for rapid and sensitive detection of pathogen [56]. Nanomaterials can be

utilized for conjugation of the antibodies, peptides, proteins, oligonucleotides and bioactive molecules to specifically determine target receptors on infected cells [18]. The 3-D nanostructured metal nanoparticles (silver and gold), semiconductors (ZnO, TiO<sub>2</sub>, CeO<sub>2</sub>, SnO<sub>2</sub>, etc.), and carbon-based materials like graphene and fullerene are finding applications in the development of biosensor devices.

## **1.6 Organization of Thesis**

The aim and scope of this thesis is to demonstrate full design, fabrication and characterization of nanophotonic slot waveguide biosensors. The introduction of the silicon grating in the slot-based waveguide and nanocomposites are exploited to enhance the sensitivity of the label free biosensors. The thesis is divided into 8 chapters with an introduction of optical biosensors, a literature survey, three major chapters consisting of original research work followed by a conclusion and future scope.

**Chapter 2.** Nanophotonic waveguide-based optical biosensors: The second chapter covers the concept and background of nanophotonic devices like slot waveguide, subwavelength grating and hybrid plasmonic waveguides and their applications in optical biosensing. The role of Fano resonance in periodic structures as a label free sensing platform is investigated. An overview of the use of nanocomposites in different point of care tools like pathogen detection is discussed.

**Chapter 3.** Optical Slot Waveguide for detection of Hepatitis B: In this chapter, the proposed nanophotonic waveguide is based on introduction of grating with TiO<sub>2</sub> overlay on slot waveguide. The gold layer under top SiO<sub>2</sub> is used to suppress the leaky mode in bottom cladding region. Morphological properties of as deposited APTMS and TiO<sub>2</sub> layers are studied. The effect of TiO<sub>2</sub> as overlay on grating of device is also discussed. The proposed device is numerically showing to detect principal marker of hepatitis-B viral infection, with a high sensitivity of 1200 nm/RIU with a figure of merit of 300. The chapter also discussed the fabrication tolerance of proposed design.

**Chapter 4:** Optical Slot waveguide for detection of viral infections: To improve sensing characteristics a biosensing device is proposed for the detection of viral infections which was based on Fano resonance. This chapter focuses on Fano resonance based engineered nanophotonic biosensing platform for the detection of viral infections. APTMS layer is synthesized as a functionalized layer to support immobilization of antibodies to bind antigens. The proposed sensor device manifests bulk sensitivity of 1463 nm/RIU for 0.02 refractive index change of analyte and limit of detection of  $1.02 \times 10^{-3}$  RIU<sup>-1</sup>. The proposed device can detect the virus analytes with the smallest refractive index change of 0.0008 in serum medium.

**Chapter 5.** Double slot hybrid plasmonic waveguide for biosensing: In this chapter nanophotonic waveguide based on engineered horizontal and vertical slots is proposed. The double slot region supports the guidance of quasi-TE mode while the quasi-TM mode is guided under the top gold layer in form of SPP mode. The bulk sensitivity in TM mode is increased by 1.5 times with gold cover. The bulk sensitivity for TE and TM mode is reported to be 1.024 nm<sup>-1</sup> and 0.95 nm<sup>-1</sup> respectively. Surface sensitivity is investigated numerically for DNA hybridization and Hepatitis surface antigen detection.

**Chapter 6.** Label-free nanocomposite film based biosensor for E. coli detection: The chapter describes the biosensor based on the interaction of E. coli with the functionalized surface of copper doped ZnO /TiO<sub>2</sub> (CZT) film over ITO thin film. The generation of photocurrent on the application of a voltage and light on ITO/CZT nanocomposite thin films was measured to detect E. coli in buffer solution. Proposed ITO/CZT thin film exhibits photocurrent for a linear range of 10<sup>3</sup> CFU/ml to 10<sup>5</sup> CFU/ml. A change of 20 μA is detected with a change in the concentration of E. coli on the application of 4 volts.

**Chapter 7.** Electrically controlled nanocomposite slot waveguide for food pathogen detection: In this chapter, a nanophotonic structure with electric control based on photocatalytic nanocomposite is proposed to

realize label-free optical detection of foodborne pathogens. The photocatalytic response of Cu-ZnO/TiO<sub>2</sub> (CZT) nanocomposite, in terms of the photocurrent, is utilized to detect E. coli in LB media solution. The fabricated nanocomposite slot waveguide exhibits a measured photocurrent difference of 9  $\mu$ A with E. coli in LB media solution. The limit of detection of E. coli bacteria concentrations is 5000 CFU/ml. The slot waveguide provides 10 times higher current density compared to thin film for the detection of food pathogen.

**Chapter 8.** Conclusion and Future scope: In this chapter all the contributions are summarized and the relevant future scope of the work is discussed.

## Chapter 2

### Nanophotonic Waveguides for Sensing Applications

#### 2.1 Optical Slot Waveguide

The slot waveguide is able to confine and guide the light in nanometer width of low refractive index region by using total internal reflection. The waveguide structure composed of two high refractive index strips, like silicon ( $n=3.45$ ) separated by low index region like air ( $n=1$ ), water ( $n=1.33$ ) or silicon oxide ( $n=1.45$ ). The slot waveguide enhances the light intensity in the slot region compared to the conventional strip waveguide [57]. The fundamental eigenmodes of two high refractive index slabs interact to generate the eigenmodes of slot waveguide.

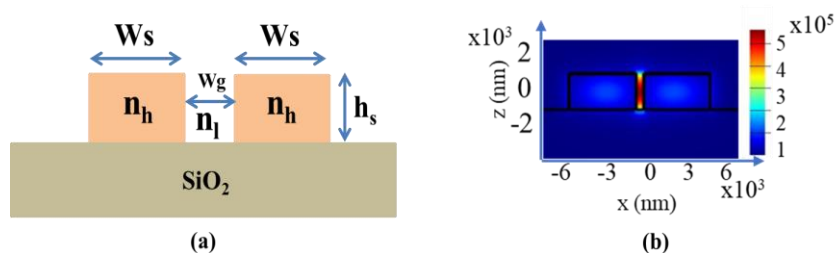


**Figure 2.1.** (a) Schematic of the slot waveguide. Strip width  $W_s$ , strip height  $h_s$ , strip refractive index  $n_h$ , slot width  $W_g$  and slot refractive index  $n_l$  are shown. (b) Electric field profile of the TE eigenmode in slot-waveguide at 1550 nm.

The slot waveguide is designed on silicon-on-insulator (SOI) substrate shown in Fig 2.1 (a), where the bottom cladding is low refractive index  $\text{SiO}_2$ , which helps in better confinement of optical energy in slot region. SOI technology platform provides many benefits like CMOS compatible technology, high core (Si) and cladding refractive index contrast, integration of lab-on-chip system and enabling more compact devices.

Slot waveguide structure supports quasi-TE and quasi-TM mode which are highly confined in slot regions. These modes are not entirely TE or TM due to the subwavelength dimensions of the waveguide [58]. They are largely TE or TM so they are called ‘quasi’ TE and TM modes. The fundamental mode of silicon waveguide i.e quasi-TE mode

where transverse electric field component is parallel to the substrate and other is a quasi-TM mode where transverse magnetic field component is parallel to substrate. For TE polarization electric field exist at sidewalls for vertical slot waveguide structure while for TM polarization electric field exist at top and bottom of the waveguide for horizontal slot waveguide structure. These TE and TM modes have different effective refractive indices. The principle of the slot is based on the discontinuity of the electric (E) field at a normal boundary between two materials. For an electromagnetic wave propagating in the x-direction, the major E-field component of the quasi-TE eigenmode (which is aligned in the y-axis) undergoes a discontinuity at the perpendicular rails/slot interfaces [59]. The discontinuity can be determined by using Maxwell equations

$$\frac{E_S}{E_H} = \left( \frac{n_H^2}{n_S^2} \right) \quad (2.1)$$

where  $E_S$  and  $E_H$  are the electric field in the slot and high refractive index region,  $n_H$  and  $n_S$  are the refractive index of slot and high refractive index regions.

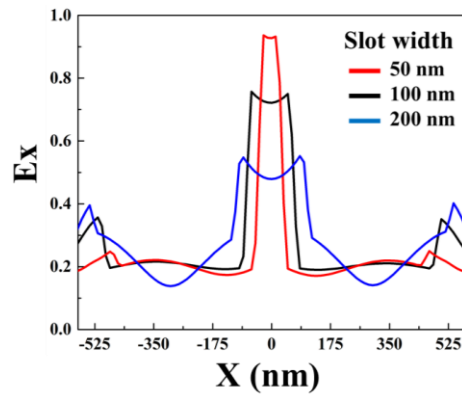


**Figure 2.2.** Electric field fundamental TE mode of the slot waveguide with silicon as high refractive index material and  $\text{SiO}_2$  as bottom cladding. Slot width vary from 50 nm to 200 nm with thickness of silicon at 220 nm.

The electric field is much stronger in the low refractive index region  $E_S > E_H$  when  $n_H$  is much larger than  $n_S$ . The eigenmode between the two high refractive index region is shown in Fig. 2.2. The decay length of the electric field is comparable to the width of the

slot waveguide, which means the electric field remains high in the low refractive index slot region and the power density is high in the refractive index region.

The confinement factor in the slot region and the cladding medium (including the slot region) is defined as follows in Eq. (2.2)

$$\Gamma = \frac{\iint_G |E(X,Y)|^2 dx dy}{\iint_{\infty} |E(X,Y)|^2 dx dy} \quad (2.2)$$

The integrals are calculated inside the slot region and the entire clad region. The optical confinement factor considering the electric field of the x component because high-contrast waveguides such as silicon slot waveguides have a large electric field of x component. The slot waveguide shows confinement of ~ 70% for quasi-TE mode and ~ 50% for quasi-TM mode. Higher confinement in slot waveguide can be achieved by narrow slot regions. Slot waveguide mode profile can be tailored by bringing variations in dimensions and materials of slot waveguides, which can be used for controlling the propagation of optical energy via a waveguide.

Applications of the slot waveguide are optical modulators [60], biosensors [61], optofluidic [62], directional couplers [63], beam splitters [64] and one-dimensional photonic crystal [65]. Slot waveguides structures are integrated with microfluidics to deliver fluids and provide better control on mode profile. Slot waveguide was first introduced by Almeida in 2004 [57]. The use of slot waveguide for sensing was described by Dell'Olivo and Passaro [59], presents the detailed study of silicon slot waveguide biosensors. They show that conventional slot waveguides have been very sensitive to cover medium refractive index change when a quasi-TE mode is considered. Dell'Olivo also calculates the waveguide sensitivity and compared it with that exhibited by other silicon nanometer guiding structures.

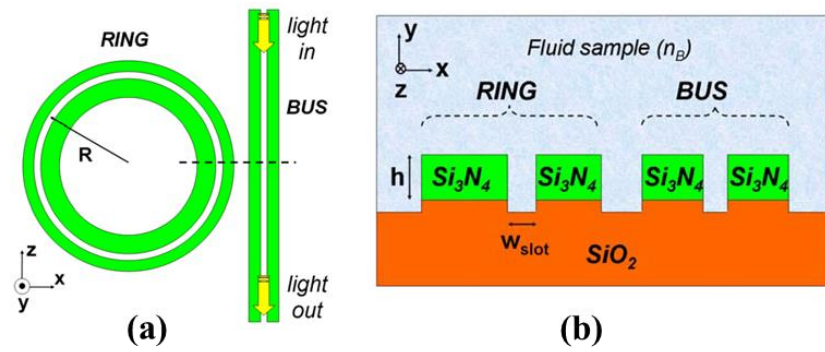


**Figure 2.3.** (a) Schematic of silicon nitride slot waveguide ring resonator. (b) Schematic cross-section of slot waveguide [58]

Barrios reviewed the application of slot waveguide in biosensing in Fig. 2.3. The optical biosensor based on silicon (SOI) ring resonator has shown a sensitivity of 70 nm/RIU. Barrios *et al.* [58] have demonstrated label-free detection by designing an integrated biosensor based on a  $\text{Si}_3\text{N}_4/\text{SiO}_2$  slot waveguide to detect the Bovine serum albumin (BSA) and anti-BSA molecular binding with sensitivity of 1.8 and 2.3 nm/(ng/mm<sup>2</sup>), respectively. A slot-waveguide based ring resonator for biosensing with  $\text{Si}_3\text{N}_4$  on  $\text{SiO}_2$  with  $140 \mu\text{m} \times 140 \mu\text{m}$  footprint and a 200 nm-wide slot region with 212 nm/RIU sensitivity is demonstrated. Claes *et al.* [41] have presented label-free biosensor based on slot waveguide with ring resonator for protein sensing with sensitivity of 298 nm/RIU as shown in Fig.2.4.

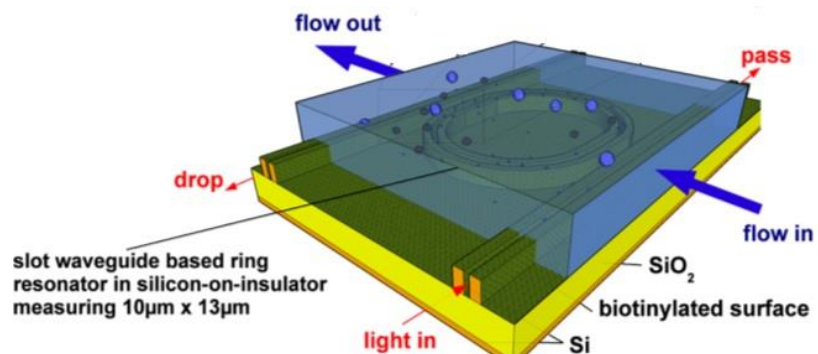


**Figure 2.4.** Schematic of silicon slot-waveguide-based ring Resonator in silicon on insulator. Top cladding is filled with analyte solution [41]

Rong Sun *et.al* [61] experimentally demonstrated the optical transmission at 1550 nm of the fundamental quasi-TM modes in single

and multiple horizontal slot waveguides and ring resonators. The horizontal slot waveguides have low propagation loss of 6 ~ 7 dB/cm. [67]. Sun et al. presented a polymer-based multiple slot structure as a

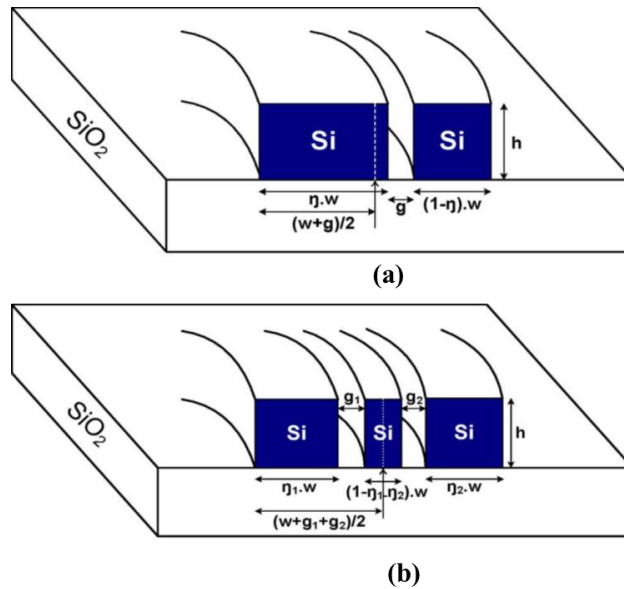


**Figure 2.5.** Schematics of (a) single-slot microring with asymmetric rib width (b) double-slot microring with a narrow center silicon rib [68]

biosensor. The structure consisted of four strips of SU-8 resist waveguides 2 μm tall by 500nm wide, and three slots of 200nm. The structure shows maximum bulk sensitivity of 244 nm/RIU. The achieved performance of these multiple-slot waveguides is less than a single-slot waveguide which is mainly due to the fact that low-contrast refractive index dielectric structures were used rather than high-refractive-index silicon. Hence a multiple-slot waveguide based on SOI and use a systematic approach to optimize a biochemical sensor for maximum sensitivity is designed.

The waveguide sensitivity of silicon slot microring sensors and single- and double-slot microrings Fig 2.5, is analyzed by Kargar in 2011 [66]. They investigate the sensing properties of slot waveguide under a variety of geometries and obtain the trend of waveguide sensitivity on each geometrical parameter. They found that the use of small dimension waveguides significantly increases resonator loss due to large E field at sidewall surfaces, degrading the Q factor and detection limit. They deduce that waveguide width needs to be selected

together with taking into consideration the impact from the surface roughness scattering due to the trade-off between waveguide sensitivity and detection limit.

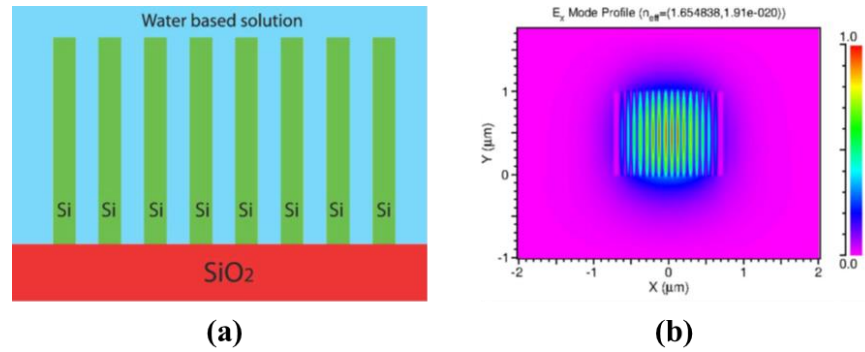


**Figure 2.6.** Schematic of multi slot-waveguide-based ring Resonator in silicon on insulator. The rib width and slot width is 100 nm respectively. [69]

Iman Khodadad et. al [67] analyses and optimize the multiple silicon slot waveguides for optical biochemical sensor, in Fig 2.6. They optimize the slot width, ridge width, number of slots, and the effect of residual silicon left at the bottom of the slot region to achieve the highest bulk and surface sensitivity when there is changes in the upper cladding of the sensor. They find that the width of the silicon waveguides can be chosen to be in the range of 70–110 nm for maximum bulk and surface sensitivities. They illustrate that increasing the slot width would increase the bulk sensitivity and when the slot width is increased, the surface sensitivity decreases due to lower field confinement in the slot region. Guohui Yuan et.al [68]demonstrates a label-free photonic biosensor with double slots based on a micro-ring resonator with a footprint of less than  $25 \mu\text{m} \times 15 \mu\text{m}$ . They consider an asymmetric structure for the ring waveguide in order to improve the sensor’s bending efficiency. The analysis shows that the sensitivity of the double-slot micro-ring resonator sensor with a radius of  $5 \mu\text{m}$  is 708 nm/RIU with a quality factor of 580 and the free spectral range (FSR) of 33 nm. Ishizaka *et al.* [69] have also presented a metal-assisted silicon slot waveguide for gas detection with a sensitivity of 458 nm/RIU. In the slot waveguide design, a metal layer is inserted in the bottom cladding to suppress the light confinement, which leads to

strong light confinement in the slot region. Hybrid plasmonic waveguides based on metal coating of dielectric ridges have been reported for sensing applications. [71]

Slot waveguide can be configured in different ways for biosensing applications. The metal layer can be used to provide confinement in slot region. Silicon ribs of slot waveguide can be arranged in the periodic form to obtain resonance peaks for analyte detection. Silicon gratings can be inserted inside and outside of the slot region for high sensitivity, quality factor and low FWHM [70]. Two types of slot waveguide configurations are presented here. The first one is to insert a gold layer in the lower cladding of the slot waveguide to obtain high confinement and sensitivity. In another approach, the silicon rib is arranged periodically with low refractive index material to form a grating structure.

## **2.2 Slot Waveguide in Subwavelength Grating Configuration**

In SWG the silicon blocks are designed as small interleaving blocks (with length only a few hundred nanometres) with air or SiO<sub>2</sub> as the second refractive index material, so the waveguide core is made up of silicon and air. The optical properties of the waveguide can be altered and tuned by varying the filling fraction of two materials in one subwavelength period. The subwavelength waveguide operates in three regimes depending on the period and wavelength (i) subwavelength  $\Lambda < \lambda/2n_{\text{eff}}$ , where the period is small to suppress the effects of diffraction and waveguide, operates as lossless waveguide, (ii) Bragg waveguide  $\Lambda = \lambda/2n_{\text{eff}}$ , where incoming light is reflected backwards completely (iii) and diffraction  $\Lambda > \lambda/2n_{\text{eff}}$  where light is scattered and gradually radiated in the atmosphere as light propagates in the periodic structure. The wave propagates in a subwavelength waveguide similar to the conventional waveguide, but the interaction between light and analyte as cladding is greatly enhanced due to periodicity in the waveguide. The shape of the electric field distribution of optical mode propagating in SWG is changing periodically.

Pérez et al. [71] in 2014 proposed the application of SWG waveguides for biosensing and analyze the sensing performance by varying the duty cycle, achieving sensitivities of 0.83 RIU/RIU for bulk sensing. After that, Chen's [72]–[74] and Chrostowski's groups [75]–[77] initiate the development of SWG waveguide-based biosensors in the SOI platform.

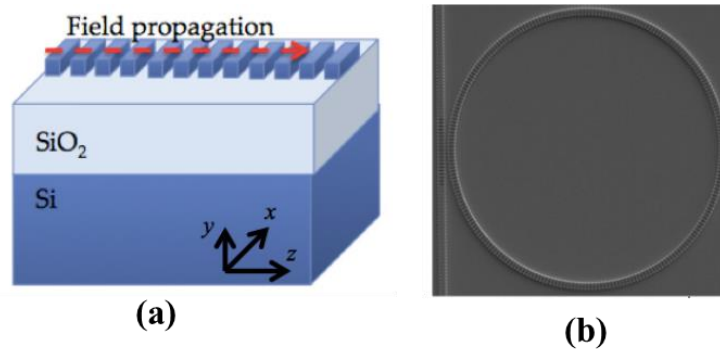


**Figure 2.7** (a) Schematic of SWG waveguide (b) SEM of fabricated ring on SOI chip. Ring radius is 10  $\mu\text{m}$  and SWG period is 250 nm [78]

Donzella et al. [78] demonstrated SOI-based subwavelength waveguide optical micro ring resonators in Fig. 2.7, showing the first time that SWG-based resonators can achieve sensitivities up to 383 nm/RIU in water and 270 nm/RIU in air. The rib thickness is 220 nm and the duty cycle are 50%. The period of all grating is kept at 400 nm. They observed that SWG rings can offer is decreased light confinement in the waveguide core which improves the resonator's sensitivity to changes in the cladding refractive index, making the rings ideal for refractive index sensing applications. Donzella et al. [75] demonstrates that directional couplers, tapers and bends are compatible with SWG straight waveguides, and can be used to build up more complex SWG based devices. They analysed that SWG directional couplers have a wavelength flattened response of more than 40 nm, bends have a loss around 1 dB per bend, and tapers have a loss lower than 0.8 dB per taper. They also illustrate that the effective refractive index of waveguide can be adjusted by choosing the period and duty cycle of the sub-wavelength grating and therefore can be optimized for a given application.

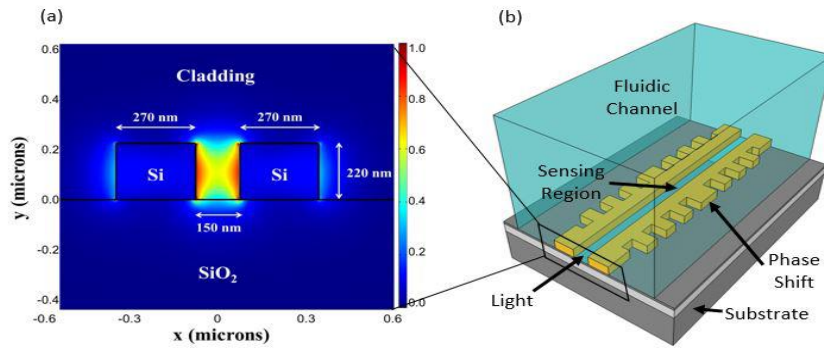


**Figure 2.8** (a) Electric field intensity of TE mode in the slot region. (b) A 3D schematic of a slot-waveguide Bragg grating in fluidic channel.[77]

Flueckiger et.al [77] designed phase-shifted slot Bragg gratings in Fig.2.8, with the slot width of 150 nm between two corrugated waveguides (arms) of width 270 nm, strongly guides the fundamental TE mode in the low-index region and results in high sensitivity and quality factor. The NaCl solution is used as an analyte to tracking the peak location in the stopband. The observed shifts resulted in a sensitivity of 340 nm/RIU and quality factor of 15,000 with iLoD for this device is  $3.04 \times 10^{-4}$  RIU. Lately, they report a follow-up work [76] by introducing NaCl solutions and a protein assay to the SWG microring resonator sensor, achieving a bulk sensitivity of 490 nm/RIU with a system DL of  $2 \times 10^{-6}$  RIU. Standard strip (or channel) waveguides for the 1550 nm telecommunication window have a rectangular cross-section (220 nm high and 500 nm wide), supporting TE and TM polarized fundamental modes.



**Figure 2.9** 3D structure of a subwavelength grating slot waveguide. The period, silicon rib width and slot width are kept at 200 nm, 300 nm, and 100 nm. [82]

Ruan et.al [79] characterizes a waveguide Fig 2.9, by combining a slot structure and a subwavelength grating. The mode guiding mechanism relies on the combination of slot mode in a slot waveguide and Bloch mode in an SWG waveguide. They illustrate that the subwavelength grating slot (SWGS) waveguide shows the lowest nonlinearity compares to strip waveguide, slot waveguide and SWG waveguide, because of more delocalization of light from silicon region. They also found that the mode confinement factor increases with the silicon width and decreases with the increase of slot width. They also propose SWGS for sensing applications because of the tight concentration of broadband light.

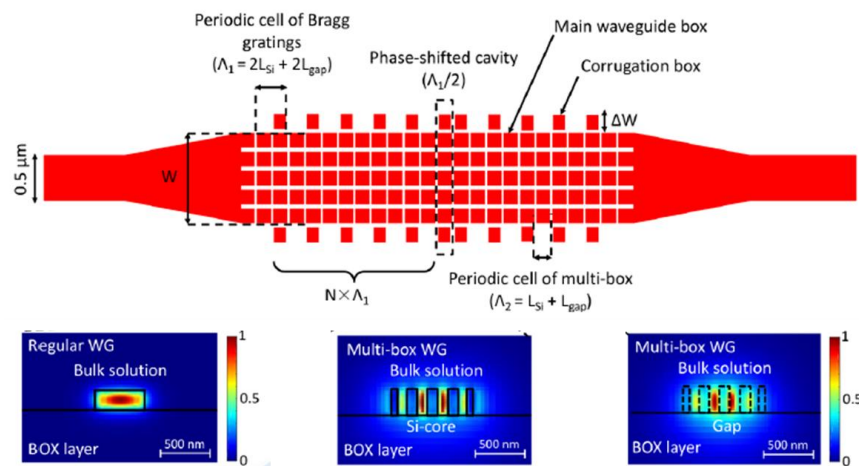


**Figure 2.10** (a) The schematic of the proposed SWGRTR with slot width of 80 nm and period is 200 nm. (b) The optical mode confinement in different regions of proposed device.[80]

Luan et al. [77] developed a sensitivity enhanced SWG-based multi-box waveguide biosensors by merging slot and SWG structures in Fig.2.10. The length of each silicon box and gap is optimized to 180 nm and 60 nm, to minimize the optical leakage into the substrate. The optical mode and the large surface area for analyte interactions offer a strong light-matter interaction at the sensor surface, thus resulting in a bulk sensitivity of 580 nm/RIU and surface sensitivity of 1900 pm/nm. The multi-box PSBG sensor presents an improved quality factor of 8000 with a minimum detectable concentration of biotin of  $2.28 \times 10^{-8}$  M. Johannes Milvich et.al [80] have performed a comparative study of

different waveguide types for application in label-free detection of chemical or biological analytes that specifically bind to functionalized waveguide surfaces. They use silicon nitride and silicon-on-insulator (SOI) and analyze a variety of waveguide types, like strips, slot and double slot structures, as well as sub-wavelength gratings (SWG). For optimum sensitivity, the waveguide should be optimized to mediate maximum influence of the surface layer on the effective refractive index of the guided mode.

### **2.3 Hybrid Plasmonic Waveguides**

Surface plasmons are the special type of oscillations called polaritons which generates from the interaction of electromagnetic waves and material vibrations. Surface plasmons are highly localized to metal surfaces and any changes that occur to the metal surface affects the property of plasmons [81]. This change in plasmonic property is used in the designing of highly sensitive biosensors. Coupling of glass prism with surface plasmon is the most successful approach in optical biosensing [82]. Surface plasmon waveguiding needs surface plasmon and index guiding. Free electrons in SPP are tightly bound to the metal surface which causes high absorption in metal [38]. Dielectric waveguides are lossless but mode size is limited by diffraction and plasmonic waveguide can compress light far below the diffraction limit at the cost of high propagation loss. A new guiding mechanism is a combination of dielectric and plasmonic waveguiding known as a hybrid plasmonic waveguide (HPW) shown in Fig 2.11 (a) [83]. The hybrid plasmonic waveguide provides a better compromise between loss and confinement compared to plasmonic waveguides and compatible with silicon on insulator technology [84]. HPW has the ability to guide mode in low index region and can support highly confined mode. Hybrid plasmonic waveguides can support a combination of plasmonic and photonic modes, and allow for sub-wavelength confinement with relative low propagation losses [85].

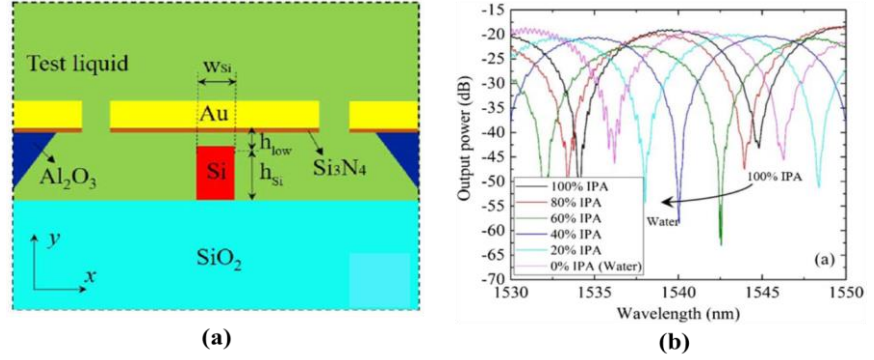


**Figure 2.11** (a) Schematic of the hollow hybrid plasmonic waveguide with Au layer (b) Transmission responses of the fabricated MZI structure of hollow HP waveguide filled with different concentrations of IPA [56].

Hybrid plasmonic waveguide can be used as biosensors which are highly sensitive, compact and provide more information about analyte compare to plasmonic waveguides. HPWG can support both TM and TE modes, the contributions from bulk and surface sensitivities. The power of TE and TM modes in hybrid plasmonic waveguide are concentrated in two different materials, their properties can be controlled by changing the material properties and waveguide dimensions of the layers [86]. The variation of bulk index of the fluid ( $\Delta n_c$ ) in Fig 2.11 (b) and the variation of thickness of adlayer ( $\Delta a$ ) are related to the change of the effective index for the fundamental TE mode (TE<sub>0</sub>) and for the fundamental TM mode (TM<sub>0</sub>). The HPWG biosensor can be implemented in many different configurations; for example, using a Mach-Zehnder interferometer (MZI) [87], grating or prism coupling.

### 2.3.1 Figure of Merit

The surface sensitivity is an important parameter for a biosensor; a small surface sensitivity does not imply a small limit of detection. The limit of detection can be defined in terms of following figure of merit

$$G = \frac{\frac{\partial n_{eff}}{\partial a}}{k_{eff}} \quad (2.3)$$

for hybrid plasmonic waveguides. The [88] detection of limit for surface sensing was shown to be inversely proportional to  $G$ . Therefore, both surface sensitivity  $\frac{\partial n_{eff}}{\partial a}$  and the imaginary part of effective mode index  $k_{eff}$  plays equally important roles in determining limit of detection of a biosensor [82]. Surface sensitivity is directly proportional to field confinement in the waveguide. For any kind of plasmonic waveguide, there is a compromise between loss and confinement i.e., one can increase the mode confinement (with a corresponding increase in surface sensitivity) but this is always accompanied by an increase in propagation loss of the guided mode. Therefore, surface sensitivity is not a true measure of DL for an affinity sensor, and  $G$  should be used instead of surface sensitivity as the figure of merit for surface sensing. The figure of merit for bulk sensing is

$$H = \frac{\frac{\partial n_{eff}}{\partial n_c}}{k_{eff}} \quad (2.4)$$

DL for bulk sensing is inversely proportional to  $H$ .

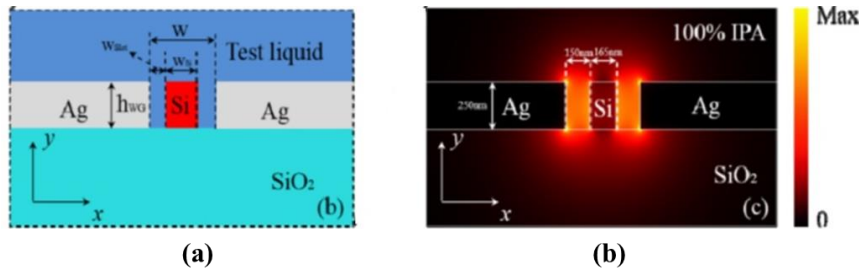


**Figure 2.12** (a) Cross-section view of the DSHP waveguide covered by test liquid. (b) Mode profile of the DSHP waveguide, where  $w_{slot} = 150nm$ ,  $w_{Si} = 165nm$  and  $h_{WG} = 250nm$ . The covering material is 100% IPA.[90]

In 2015, Sun et al. [89] developed a MZI sensor employing an ultra-compact double-slot hybrid plasmonic (DSHP) waveguide as an active sensing arm. By introducing a DSHP as shown in Fig 2.12, waveguide with two open nano-slots between a high-index Si ridge and two silver strips, a high optical confinement with low propagation loss was

achieved, showing a sensitivity as high as 1061 nm/RIU. M. A. Butt et.al [90] proposed a refractive index sensor which is the combination of silicon strip waveguide and a hybrid plasmonic microring resonator. The hybrid waveguide is made up of a metal-air-silicon waveguide structure, where the electric field is significantly enhanced in the narrow air gap between ring and strip waveguide. The sensor has the best sensitivity of 401 nm/RIU and 690 nm/RIU with a FoM of 40 and 98, for biosensing and gas sensing applications, respectively. Mohamed Farhat et.al [91] investigates a hybrid plasmonic slot-waveguide (HPSW) biosensor based on silicon-on-insulator for DNA hybridization detection shown in Fig. 2.13. The design consists of two silicon nanowires close to each other depositing on a gold layer of thickness and sandwiched between two gold rails. They report biosensor has high sensitivity of 1890.4 nm/RIU with a detection limit of  $2.65 \times 10^{-6}$  RIU.

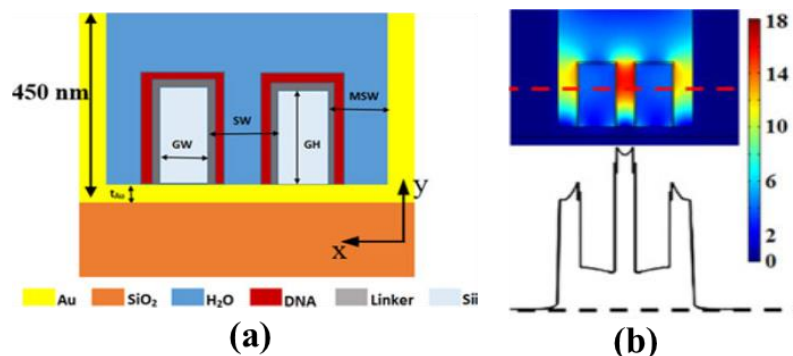


**Figure 2.13** (a) Cross section of the suggested HPSW biosensor (b) Confinement in the slot regions for the suggested design at  $\lambda = 1.55 \mu\text{m}$  [91]

Chen et.al [92] in 2017 proposed a hybrid plasmonic waveguide with nano slots with silicon as a rib waveguide and silver as cladding integrated with MZI. The sensor detects the HepV binding to the silicon and metal with functionalization of streptavidin and biotinylated heparin. Sun [87] in 2017 proposes a Mach-Zehnder interferometer (MZI)-based liquid refractive index sensor, utilizing a hollow hybrid plasmonic (HP) waveguide as the sensing element. The waveguide sensitivity, is demonstrated to be 0.64, with a propagation loss-less than 0.25 dB/ $\mu\text{m}$  and with MZI sensor the sensitivity is 160

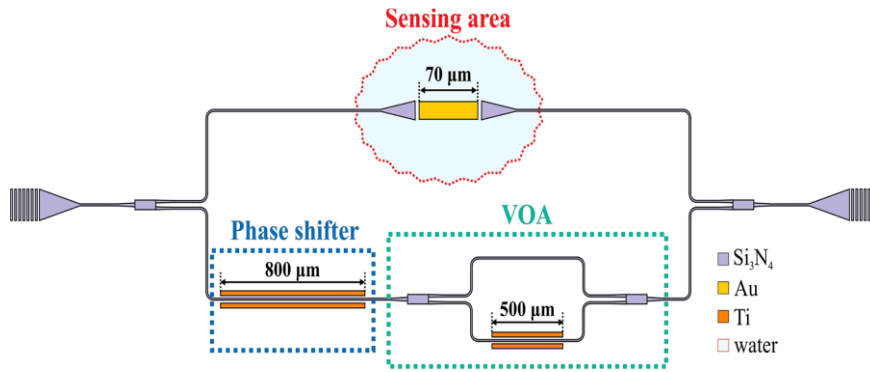


**Figure 2.14.** Schematic of the plasmo-photonic MZI sensor. An Au metal stripe serves as the sensing element. Thermo-optic phase shifter and a variable optical attenuator are implemented in the reference arm for tuning at the desirable wavelength and power balancing, respectively [93].

nm/RIU, with an extinction ratio larger than 40 dB with a low detection limit of  $2.8 \times 10^{-6}$  RIU. Chatzianagnostou et.al [93] designed and experimentally evaluated a refractive index sensor based on an integrated plasmo-photonic silicon nitride ( $\text{Si}_3\text{N}_4$ ) MZI structure exhibiting high sensitivity based on planar surface plasmon polariton (SPP) waveguide shown in Fig.2.14. A 70  $\mu\text{m}$  long Au-based plasmonic stripe, cointegrated on a low-loss  $\text{Si}_3\text{N}_4$  photonic platform incorporated in the sensing arm serving as the transducer element. In the reference arm, a variable optical attenuator stage in combination with a thermo-optic phase shifter are deployed for performance optimization. The bulk sensitivity observed up to 1930 nm/RIU and a resonance extinction ratio of 37 dB.

## 2.4 Fano Resonance in Periodic Structures

In the last few years an enormous amount of research done to demonstrate Fano line shapes in periodic plasmonic nanostructures and metamaterials. The resonant scattering properties of subwavelength periodic structures and interference can be modified to their asymmetric Fano line shapes [94]. Fano resonance asymmetry originates from the interaction of the broad resonance or continuum state with a narrow resonance or discrete state, were first discovered in quantum interference to describe asymmetric autoionization spectra of He atoms[95]. Biosensors based on asymmetric Fano like resonances

are based on various wavelength ranges like visible or infrared[94], [96], [97]. Fano resonance can be created by bringing proper symmetry breaking in symmetric nanorods structures, by arranging periodically the nanorods to reduce radiative losses[98], [99] The result of constructive and destructive interferences of broadband continuum states with discrete resonance states emerges as Fano resonance. The directly excited broadband continuum states are known as bright modes and mode which cannot be addressed is known as dark mode of discrete resonances[100]. Structural asymmetry can achieve Fano resonance in nanophotonic structures. Fano in 1961 introduced the asymmetry parameter  $q$  as a ratio of the mixed state and continuum transition probabilities.

Fano formula for scattering cross-section for  $l$ th partial wave defined as[101]:

$$\sigma_l = \frac{4\pi}{k^2} (2l + 1) \text{Sin}^2 \xi_l(k) \frac{(q + \varepsilon)^2}{1 + \varepsilon^2} \quad (2.5)$$

$\xi$  is the background phase shift.

$$\text{Where} \quad \varepsilon = -\cot \delta_l^r(k) \quad (2.6)$$

$$q = -\cot \xi_l(k) \quad (2.7)$$

When  $\xi_l$  is small  $\sigma_l$  becomes  $\sigma_l^r$  and when  $q = -\varepsilon$  ;  $\sigma_l$  becomes 0.

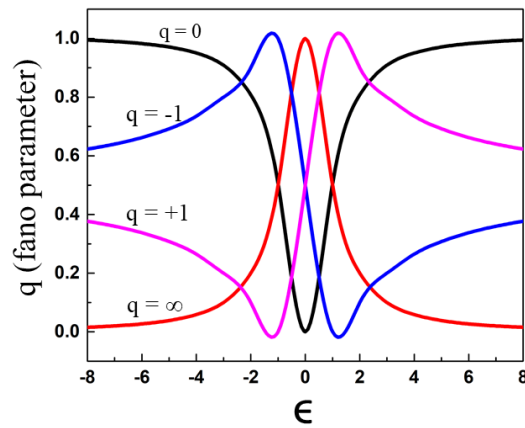


**Figure 2.15.** Normalized Fano profile for various values of the asymmetry parameter  $q$ .

It is not when you have resonance effects the scattering cross-section must only increase, it can be decreased or vanish or got to zero. To show the effect of background phase shift on Fano shape we calculate the spectra from the Fano formula shown in Fig.2.15. The asymmetric parameter  $q$  is to indicate the discrete state and continuum state strengths during coupling. If the phase shift equal to zero or integer multiple of  $2\pi$   $q$  tends to be infinity as shown in the graph. The line shape is determined by transition through discrete state only with Lorentzian profile of a Breit Wigner resonance or, if coupling of continuum states and external perturbation does not occur, means continuum modes and discrete modes do not couple strongly then we get  $q = \rightarrow \pm\infty$ , the Fano profile becomes symmetric Lorentzian function and asymmetry disappears. When  $n$  is an odd number because of destructive interference between discrete and continuum resonance modes, the Fano spectrum evolves into EIT like a peak or extremal perturbation coupled with a discrete state, not with continuum states, Fano shapes become antiresonance (suppression of resonance) symmetric quasi-Lorentzian and  $q = 0$ . For other values of phase shift like nonzero values of  $q$ , discrete and continuum resonance modes exist at the same time with destructive and constructive interferences to generate the asymmetric Fano line shapes[102], [103]. Asymmetrical Fano profile shape is seen at  $q = 1$  when both continuum and discrete transition are same with maximum value at  $E_{\max}=EF+q/2$  and minimum at  $E_{\min}=EF-q/2$ .

Fano resonances are generally related to coherent scattering in regular structures like sphere and cylinders, but many results show that it can also sustain in disordered or periodic photonic systems. A number of research articles has been reported with high Q-factor and sensitivity using Fano resonance in discrete structural geometry such as photonic crystals, plasmonic structures, ring disk nano-cavities and gratings [104]. Yang et al. [105] developed a Si-based meta-surfaces with EIT (Electromagnetic Induced Transparency) resonance refractive index sensor Fig .2.16, with a sensitivity of 300 nm/RIU and FOM of 100 in the near-infrared regime. They show that the dielectric metasurfaces

can be engineered to confine the optical field in either the silicon resonator or the environment, allowing one to tailor light-matter interaction at the nanoscale. The coupling to free space is provided by the bright-mode resonators, which are placed in close proximity to the symmetric dark-mode resonators. They observed the transmittance of 82% with Fano line shape at a wavelength of 1371 nm with a Q-factor of 483.

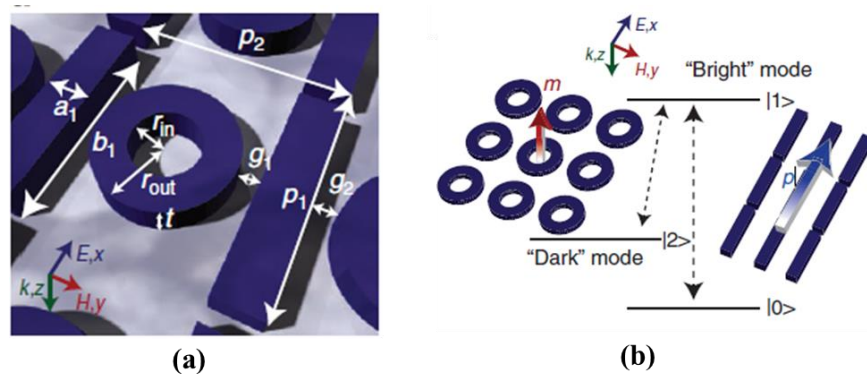


**Figure 2.16** (a) Schematic of the metasurface with one bus and one ring structure forming the one-unit cell. (b) Schematic of interference between the bright- and dark-mode resonators.[105]

To achieve the Fano resonance in the waveguide, the guided modes have to couple with local defects or cavities. Fano-resonant metasurfaces based on silicon and its oxides supporting optical resonances with high-quality factors  $Q > 100$  have been demonstrated experimentally. Each unit cell of the waveguide is composed of one straight and one bent silicon nanorod, where the bend is responsible for coupling between bright (electric dipole) and dark resonances. Higher FOM is one of the important factors to be used in Fano resonant refractive index sensing applications. A narrow photonic band interacts with the continuum spectrum through an interference effect constructively or destructively leading to Fano resonance. Zhang et. al [107] analyses the based on periodical asymmetric paired bars, Fig 2.17, in the near-infrared regime and observed multiple Fano resonance with a high Q factor of 105. the highest sensitivity achieved is 370 nm/RIU and a figure of merit of 2846. They deduce that multiple Fano resonances can be easily tailored by adjusting different

geometric parameters. The sharp peaks and intrinsic multimodal response make this waveguide structure suitable for refractive index sensing.

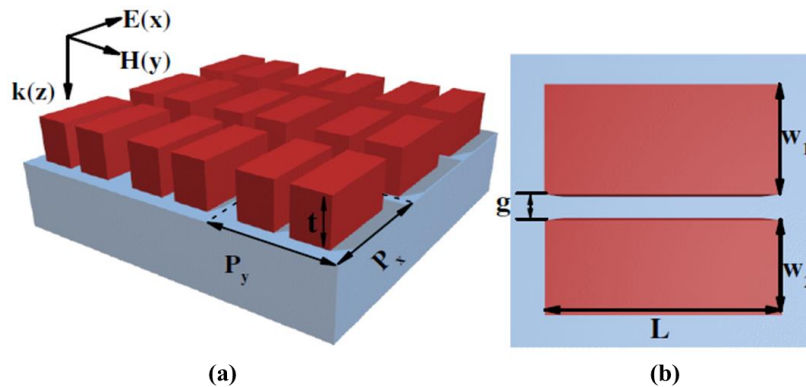


**Figure 2.17.** Schematic of the dielectric metasurface composed of periodical asymmetric Si nanobar pairs. (b) Top view and geometric parameters of a unit cell of the Si bar pairs [107].

Zhang et.al [108] proposed the surface plasmon polariton refractive index sensor based on Fano resonances in metal-insulator-metal waveguides coupled with rectangular and ring resonators. The device exhibits that when the refractive index of the fill dielectric material in the slot of the system is increasing, the Fano resonance peak exhibits a remarkable redshift, and the highest value of sensitivity ( $S$ ) is 1125 nm/RIU. Wu et.al [109] investigates the design of silicon-based Fano-resonant unit cells with the bright and dark mode resonators shown in Fig 2.18. The bright mode resonance created by collective oscillations of the bar resonators while the ring resonators interact through near-field coupling forming the dark mode. Nanostructures have been designed to generate Fano resonances, such as disk and ring cavities,

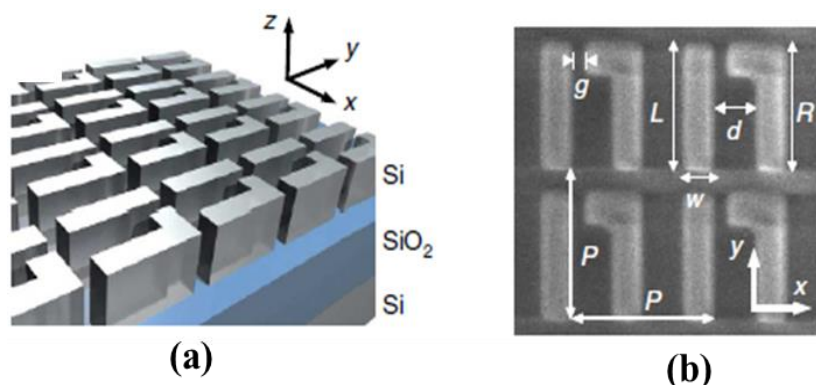


**Figure 2.18.** (a) A schematic of the silicon-based chiral metasurface supporting high- $Q$  Fano resonances. (b) The SEM image of the fabricated sample and geometry definitions [109]

nanoshells, and mismatched nanoparticle dimers. With cautious engineering of nanostructures, more than one dark mode may be excited, thereby forming multiple Fano resonances, and radiative damping can be simultaneously suppressed at different spectral positions.

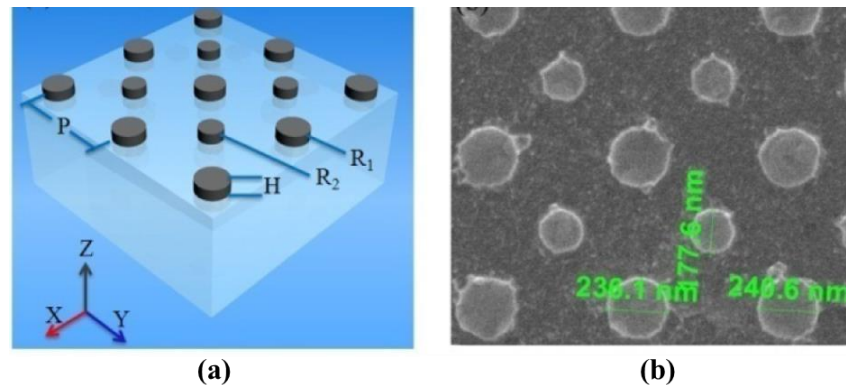


**Figure 2.19.** 3-D scheme of binary silicon nanodisk array with particle radii of  $1 R$  and  $2 R$  (b) top view of corresponding SEM image [110].

Zhao et.al [110] presented in Fig 2.19, the study of Fano resonance originating from the interaction of in-phased lattice collective resonance and antiphased lattice collective resonance supported by a silicon nanodisk array. They demonstrate that binary silicon nanodisk array can act as an optical filter and offers an efficient way to tune the linewidth by changing the radius of the particles. When the radius  $2 R$  increasing from 60 nm to 115 nm the linewidth varies 12 nm to 0.7 nm and  $Q$  factor varies from 72 to 1290. The theta-shaped dielectric arrays based is designed and numerically analyzed generated Fano resonance with an enhanced  $Q$ -factor.  $Q$ -factor in theta-shaped Si arrays is one order larger than that of the perfect disk arrays due to breaking the symmetry [103]. The high  $Q$ -factor and strong magnetic near-field enhancements can be easily tailored by adjusting different geometric parameters and this provides a useful insight into their tuning behaviour. Single silicon disk is investigated for polarization-independent Fano resonances with strong modulation depths. The subradiant mode is form by interaction of strong electromagnetic fields of the dielectric nanodisk, and magnetic field with the electric dipole [100].

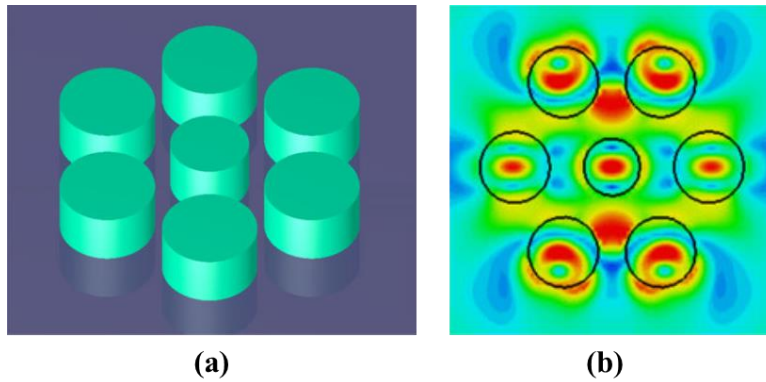


**Figure 2.20** (a) Schematic of a silicon oligomer with six nanodisk of larger radius surrounding the central smaller radius nanodisk (b) Electric field profiles at the positions of the main resonances[111]

Chong et.al [111], in Fig 2.20, demonstrate refractive index sensing with localized Fano resonances in silicon oligomers. The structure consists of six disks with a large diameter surrounding a central one of slightly small diameter. The refractive index sensitivities are up to  $150 \text{ nmRIU}^{-1}$  and  $428 \text{ nmRIU}^{-1}$  have been observed experimentally. Due to their sharp resonances profile and strong near-field enhancements, Fano resonances are promising to improve the performance of optical biosensing.

## 2.5 Food Pathogen Detection with Nanocomposites

Many bacterial pathogens and toxins in food are responsible for foodborne illness that is hazardous to human health. The bacteria, viruses and parasites present in the foods are the main reason for foodborne diseases [112]. Because of its toxin generating capability, *E. coli* has drawn considerable attention, which can damage the intestinal lining, anaemia and stomach cramps with infective dose [56]. Food safety is an important aspect of public safety. Many technological advancements have been made by new developments in nanotechnology to build smart biosensors for the detection of adulteration and contamination of foodborne pathogens [5], [113]. Label-free methods of electro-optical detection for pathogens leads to monitor interactions between chemical and biological analytes, provide results in real-time and detect analytes without using labels.

Nanomaterials are used in different types of biosensors which can detect toxic contamination. Various advancements in nanotechnology have enabled new technologies for rapid pathogen detection. Nanomaterials such as nanoparticles, nanorods, nanosheets and 3D-nanostructures have demonstrated remarkable advantages in sensing applications [114]. Different types of techniques are used to prepare a sensing layer with desired and controlled characteristics. The sensitivities reported for the detection of a wide range of pathogens using a variety of surface modifications methods and assays. Several techniques are available for the detection of food pathogen based on conventional methods summarizes in Fig. 2.21.

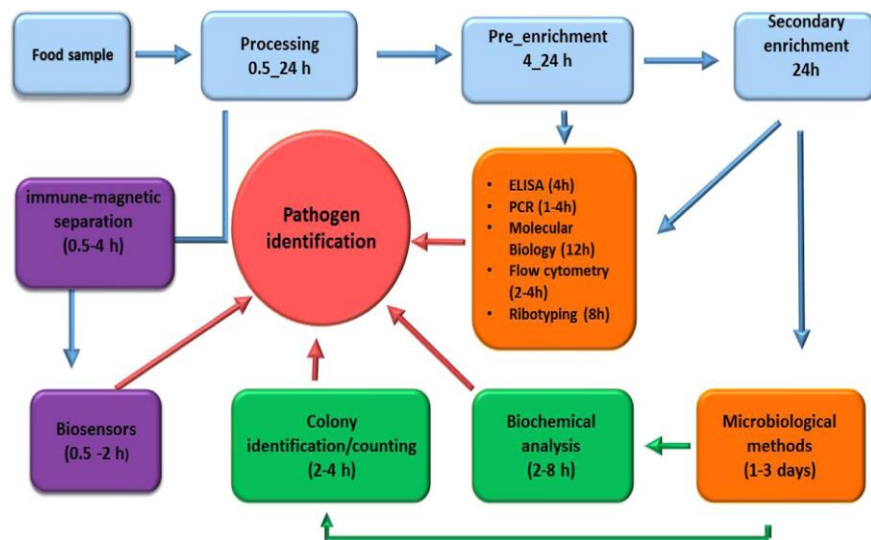


**Figure 2.21** Methods available for pathogen identification[113]

Detection of Escherichia coli [115] O157:H7 at  $10^2$  to  $10^3$  CFU/ml has been achieved by coating the gold surface with streptavidin and biotin-labelled antibodies on the assembly of streptavidin. Among different proteins for immobilization, Protein G and protein A have been successfully applied in immobilizing antibodies to sensor surfaces for the detection of bacteria. Using mixed SAM, Jyoung et al. developed an immunosensor based on surface plasmon resonance (SPR) for Vibrio cholerae O1 with a detection limit of  $10^5$  CFU/ml. A monoclonal antibody, which was confirmed to be specific to V. cholera O1 was immobilized on the protein G layer. Jain et al. [116]

developed a biosensor by using carbon nanotubes (CNTs) for the detection of Salmonella. Salmonella monoclonal antibodies were covalently attached to the high surface area of CNTs by using diimide activated imitiation coupling then immobilized onto a glassy carbon electrode. Joo et.al [117] detected Salmonella bacteria in milk by using antibody-conjugated magnetic nanoparticles (MNPs) and separated them from the samples by applying an external magnetic field. Chen et.al [118] employed a single-walled carbon nanotube field-effect transistor biosensor and incorporated it with the *E. coli* DH5R aptamer. The sensor was able to detect *E. coli*, at concentrations two orders of magnitude higher than that of the standard MPN protocol, and there was no change in sensor response when *S. typhimurium* was applied to the sensor. A carbon nanotube (CNT) chemi-resistive biosensor coated with antibodies was presented which detects the variations in cell numbers of *E. coli* O157:H7, with a limit of detection of 100000 CFU/mL [119]. Teng and co-workers [120] used ferrocene-functionalized ZnO nanorods to detect *E. coli* and changes in current corresponded to changes in *E. coli* cell numbers and as few as 50 CFU/mL could be detected. A highly sensitive impedance-based biosensor device was reported [121] where an alumina nanoporous membrane with a PDMS microfluidic flow cell was immobilized by an antibody specific to *E. coli* O157: H7 via self-assembled GPMS silane. Other *E. coli* sensors report the limit of detection up to  $10^4$  CFU/ml using porous SiO<sub>2</sub> via direct cell capture [122]; limit of detection  $10^3$  CFU/ml using over oxidized polypyrrole film with dielectrophoresis [123] and limit of detection  $7.4 \times 10^4$  CFU/ml using magnetic nanoparticle–antibody conjugates with microelectrode-based impedance biosensor. Rakesh Narang et.al [124] presented a microfluidic-integrated microwave biosensor for detecting the concentration and proliferation of *E. Coli* in real-time. The microwave microstrip ring resonator sensor was designed for the detection of the concentration and growth of bacteria, incorporated with a microfluidic channel, operates on frequency of 2.5 GHz with the quality factor of 83. The changes in resonant amplitude and frequency responses of the

microwave system were observed to detect the different concentrations in different pH solutions.

## **2.6 Thesis Objective and Contribution**

The objective of this thesis is to create new, SOI compatible silicon nanophotonic sensors, to develop novel waveguides structures with performance better than available silicon photonic biosensors. The aim is to demonstrate the full design, fabrication and characterization of label-free slot waveguide optical biosensors utilizing an on-chip integrated platform. The objective is accomplished by improving the bulk and surface sensitivity, detection limit and figure of merit of transverse electric (TE) and transverse magnetic mode resonators in slot waveguide topologies.

Following are the objectives of research work carried out for this thesis:

- To design engineered slot waveguide devices for the detection of viral infections.
- To design and analyze engineered nanophotonic structures for biochemical sensing
- To process and analyze nanocomposites for biosensing applications
- To fabricate an electrically controlled nanophotonic structure based on nanocomposites for the optical detection of food pathogens

## Chapter 3

### Optical Slot Waveguide for Detection of Hepatitis B

The nanophotonic sensing platforms based on slot waveguide for the detection of viral infections are designed. The introduction of silicon grating in the slot-based waveguide enhances the sensitivity of the label-free biosensors. By optimizing the pitch, width and duty cycle of the grating, the effective index of the medium can be engineered. The slot is created between the cladding made up of silicon and TiO<sub>2</sub> grating. The presence of TiO<sub>2</sub> overlay provides the twofold benefit of bio-compatibility with higher sensitivity. A gold layer under top SiO<sub>2</sub> is used to enhance optical confinement in the slot region. The device is numerically shown to detect surface antigen HBsAg, a principal marker of hepatitis-B viral infection, with a high sensitivity of 1200 nm/RIU with a figure of merit of 300. To further improve the sensing performance the combination of nano-disk with a grating in optical slot waveguide is designed. The device based on Fano resonance, can detect very small refractive index change of 0.0008 with high sensitivity of 1463 nm/RIU. The device is numerically shown to detect surface antigen HBsAg, a principal marker of hepatitis-B viral infection.

#### 3.1 Slot Waveguide Based on Grating-Loaded Cladding of Silicon and TiO<sub>2</sub>

Detection of viral diseases at an early stage is crucial for timely treatment and health recovery. On-chip detection of viral infections on silicon platform is advantageous to realize CMOS driven sensing systems which require silicon based sensor design which is compatible with existing CMOS fabrication technology with minimal change [76], [125]–[127]. The real time measurements with optical biosensors are possible and they are intrinsically label free and does not require modification of primary or secondary target with a probe [128]. This

makes the operation and the readout more effortless and less prone to possible artifacts arising from labeling [129]. Integrated photonic devices enable label-free and cost-effective approach for biosensing applications [74], [130]–[132]. On-chip nanophotonic devices for the detection of viral infections is being possible due to the confinement of light in sub-micron dimensions. The advancement in integrated photonic devices led to the detection of viral infections and other bio-analytes with enhanced sensitivity [75], [133].

In integrated photonic sensing platforms tight optical confinement with tailorable characteristics is a primary requirement for the detection of bio samples. Plasmonic waveguide is one of the best suited platforms for biosensing [134]–[136]. Light can be confined in a high refractive index or low refractive index waveguide or by creating deformity states in a periodic structure. The analytes with bio-molecules are usually water-based solutions with refractive indices near to 1.33, hence for better sensing the optical confinement in low indices are desirable. Usually the light is guided in a higher refractive index, therefore, the interaction of light with the sensing material in the cladding or at the surface of the waveguide is limited, leading to the low sensitivity of the device. One of the finest examples of guiding light in low refractive index media is the slot waveguide [57] which has been utilized to realize number of photonic functionalities for variety of applications [46], [58], [137]. The slot waveguide structure has two higher refractive index rails of silicon waveguide close to each other. The principle of the slot is based on the discontinuity of the electric (E) field at a normal boundary between two materials. For an electromagnetic wave propagating in the x-direction, the major E-field component of the quasi-TE eigenmode (which is aligned in the y-axis) undergoes a discontinuity at the perpendicular rails/slot interfaces. In slot waveguide, a large amount of optical energy can be confined in the slot region and this optical energy can be influenced by the presence of the sensing medium to yield a highly sensitive sensor [41]. The gold layer below the slot waveguide is helpful for suppressing the optical

leakage in substrate making strong light confinement in the slot region [69].

The introduction of the grating in the slot-based waveguide can enhance the sensitivity of the sensors. The waveguide grating usually composed of silicon pillars in a periodic manner in the direction of propagation having period smaller than the operating wavelength. By optimizing the pitch, width and duty cycle of the grating, the effective index of the medium can be engineered. The proposed nanophotonic sensing device has a larger fraction of the optical mode propagates in 100 nm wide low-index region where the bio-molecules are located. The bio-sample can be flexibly placed in the central slot region, on the grating or around both the gratings. The inclusion of gold and grating has increased the optical confinement in slot region which in turn increase the interaction of light with bio-sample. Hepatitis B surface antigen (HBsAg) is the principal marker for the diagnosis. The HBsAg is the first protein that appears in the serum after the incubation period, which confirms acute HBV infection [138]. The size of HBsAg is 22 nm and in 1  $\mu\text{g/ml}$  it forms the thickness of 4 nm. The device shows high sensitivity of 1200 nm/RIU for the detection of surface antigen HBsAg, with a very small FWHM of 4 nm. In all computations we use APTMS as a bio-receptor for HBsAg. The proposed sensor device can detect even a small change of 0.005 in analyte indices. We numerically investigate the effect of the structural parameters on the optical properties the sensor. The bio-sample can be flexibly placed in the central slot region, on the grating or around both the gratings.

The proposed nanophotonic biosensor based on optical slot waveguide is designed on silicon on insulator platform as shown in Fig. 3.1. The slot is created by placing two one dimensional silicon-air grating over the silicon rib separated by a low-index region (air-slot) of 100 nm. These two silicon ribs of slot-waveguide strongly confine light in a nanoscale low refractive- index material (analyte) shown in inset Fig.1. For providing strong confinement a gold layer of 200 nm thickness is sandwiched between buried oxide and top silicon oxide cladding [28]. The reflecting property of gold layer helps in stronger

optical confinement in the slot region by prohibiting the light to propagate in the lower SiO<sub>2</sub> cladding.

### 3.2 Proposed Device Design

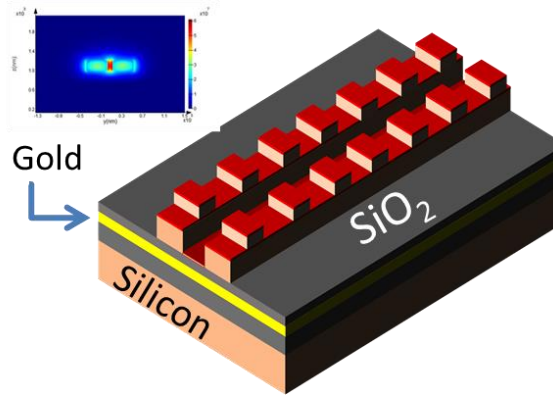


**Figure 3.1.** Schematic of Grating loaded slot waveguide with overlay layer of TiO<sub>2</sub>. Inset optical mode confinement in slot region.

In simulation the top surface is assumed to be filled with the target bioanalyte, HBsAg, a principal marker of hepatitis-B viral infection, which acts as a cladding for the optical confinement. The one-dimensional grating over slot induces the resonance in the device and increase the light-matter interaction. The thickness of silicon/air grating structure with silicon rib is 200 nm, grating period of 300 nm, and duty cycle of 33%. To increase the sensitivity of the device a 20 nm thick of TiO<sub>2</sub> is placed over the top surface of the device including the ridge formation in slot region, which in turn makes the total thickness of device 220 nm. Rib width, Slot width, grating thickness and overlay thickness are optimized to achieve large optical field overlap with sensing medium. The maximum part of optical field confinement is delocalized from high index silicon region into the slot region which is filled with the analyte. Fig. 3.2 shows a side view of the proposed device with an overlay of TiO<sub>2</sub>. For 200nm thick top silicon, grating period ( $\Delta$ ) and grating thickness (d) are optimized to 300nm and 100nm respectively. The inset of Fig. 2 shows the mode-field propagation in the device. The major part of optical mode travels in the slot region partially overlaps with the grating over the rib of the

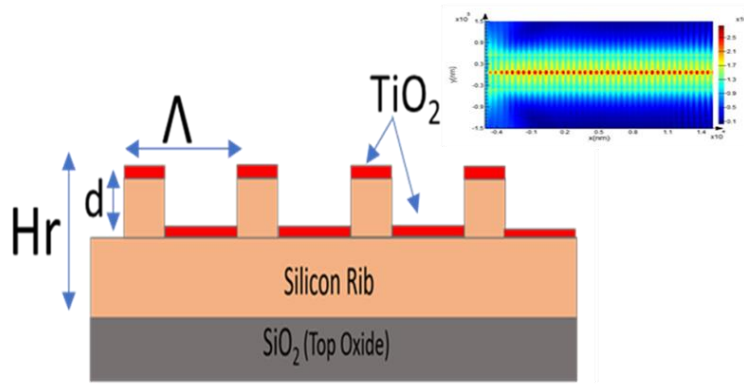


**Figure 3.2** Side view of the proposed design with an overlay of 20-nm thick  $\text{TiO}_2$  layer.  $\Lambda$ ,  $H_r$  and  $d$  represents the period, total height and grating depth of the device respectively. Inset shows top view showing optical mode propagation in 100 nm wide slot region.

slot (top view). Simulations of the proposed device are performed using the Lumerical simulation software. The FDTD simulations are suitable since the grating devices and slot devices are invariant in one dimension (i.e., along with the x-axis). 3D FDTD gives exact quantitative results as compare to 2.5D FDTD simulations. They are less computationally intensive and can be used to understand the device characteristics and properties of the proposed device [30]. The mesh resolution is set at auto non uniform with a mesh accuracy index of 3 as defined in Lumerical. The source wavelength used for simulation is 1300 nm to 1600 nm. PML is designed to absorb the outgoing waves from the active computation domain without reflecting them back to the active region of the device. The perfectly matched layer boundaries and metal boundaries are located at more than 3 times the dimension of the device being simulated along the y-axis and z-axis.

### 3.3 Analysis of Deposited Layers

A partial experimental study of thin films of Gold,  $\text{SiO}_2$ , APTMS and  $\text{TiO}_2$  which are required in final device fabrication is presented. The computation of device design and characteristics used in simulation include measured dimensions and refractive indices of  $\text{TiO}_2$ , Gold and  $\text{SiO}_2$ . The silane chemistry for covalent attachment of capture agent

(APTMS) over the silicon and TiO<sub>2</sub> is used to increase the stability and robustness.

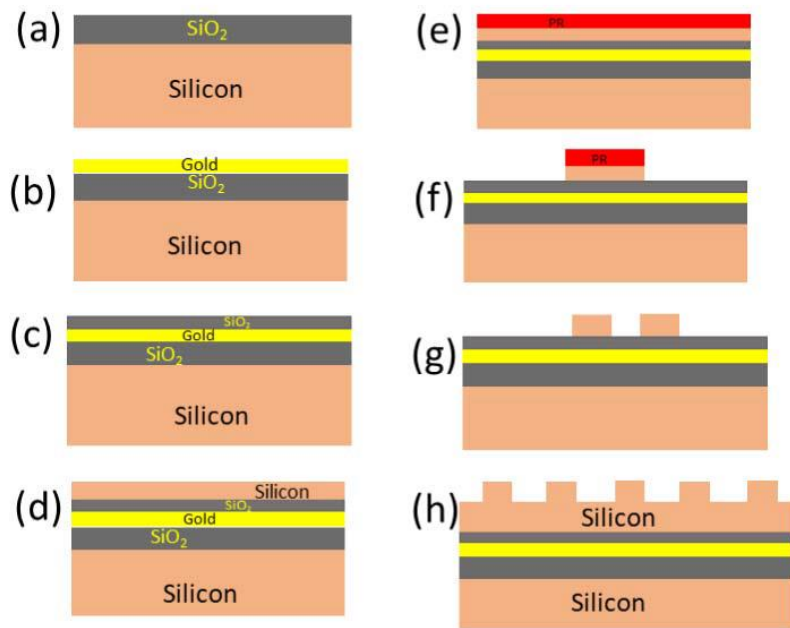
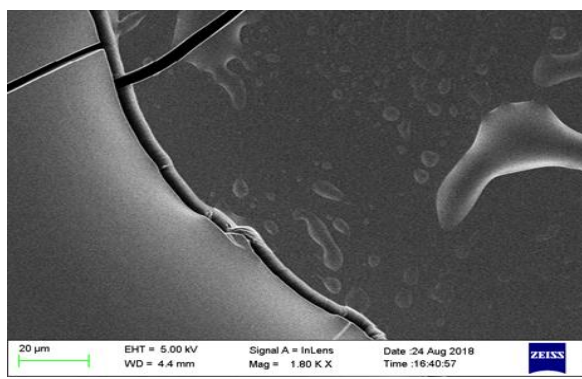


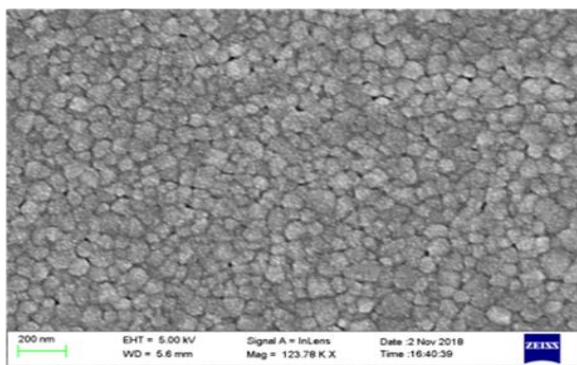
**Figure 3.3.** Process flow for bottom cladding and silicon (a-d). from Fig. 3(e-h) are the process steps to be adopted in near future for the fabrication of final device.

At first, the silicon wafer is cleaned by piranha cleaning process with 1:3 ratio of H<sub>2</sub>O<sub>2</sub> and H<sub>2</sub>SO<sub>4</sub>, continued by HF dip to remove all oxides and contaminants from the top surface of silicon wafer. The 2 μm thick SiO<sub>2</sub> is grown over the silicon surface by PECVD process at a pressure of 313 m Torr at 300°C shown in Fig. 3.3 (a). The rate of deposition is 400 Å/min. The sample is then annealed at 800°C for 2hr. The 100 nm thick layer of gold is deposited by electron beam evaporation method in Fig. 3.3 (b). The top SiO<sub>2</sub> layer is deposited by PECVD at 300°C and 315 m torrs Fig. 3.3 (c). The top silicon of 220nm is deposited using PLD at 200°C over the SiO<sub>2</sub> Fig. 3.3 (d). To create the slot and grating we deposit photoresist by spin coating and pattern is transfer by Electron Beam Lithography. After RIE etch we obtain the slot and grating structure Fig. 3.3 (e-h). TiO<sub>2</sub> is deposited over the top of entire slot and grating structure. APTMS as bioreceptor is deposited by silanization process

The SEM image of interface of SiO<sub>2</sub> and gold shown in Fig. 3.4 (a). An adhesion layer of chromium is used in the ratio of 20 nm:100 nm (chrome: gold). The scanning electron microscopy has been used to analyze the surface morphology of sol-gel deposited TiO<sub>2</sub> thin film on p-Si substrates as shown in Fig. 3.4 (b). The SEM image clearly shows that the deposited sol-gel based TiO<sub>2</sub> thin film is homogeneous and uniform with a grain size of 60 nm. For the sol-gel synthesis of TiO<sub>2</sub>: Titanium butoxide, butanol, acetylacetonate and acetic acid are mixed and stirred at 500 rpm for 8 hrs. at room temperature until the clear



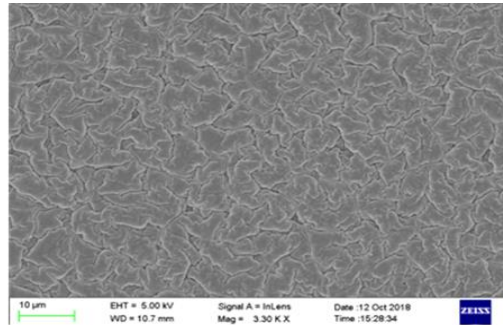
(a)



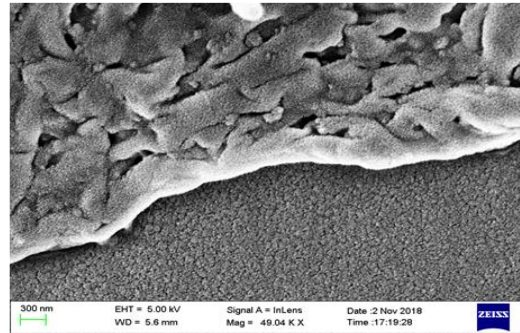
(b)

**Figure 3.4.** (a) SEM image showing the interface surface Gold (100 nm thick) deposited by electron beam evaporation over SiO<sub>2</sub>. (b) SEM image of sol-gel derived TiO<sub>2</sub> thin film grown on intrinsic Si <100> substrate

yellow color liquid is formed. Thin films by precursor sols are deposited using spin coater at 2000 rpm for 30 seconds. The spin coated film is heated at 50°C followed by annealing at 800°C for 1 hr. Sol-gel deposition of TiO<sub>2</sub> is cost effective and easy to process.



(a)



(b)

**Figure 3.5.** (a) SEM image of APTMS over intrinsic Si  $\langle 100 \rangle$  substrate. (b) SEM image of APTMS over TiO<sub>2</sub> after 3 hours of immersion in solution.

The functionalization of the freshly cleaned wafers is carried out in a 3-mM solution of 3-aminopropyltrimethoxysilane (APTMS) in Ethanol as a solvent over a silicon surface. Silane deposition can be carried out in solvents like ethanol, acetone and isopropanol. By adding amine functionality variety of bioconjugation techniques to capture agent is possible. The reaction takes place in a petri dish for 3 hr at 25°C. After completion of the reaction step, the wafers were rinsed for two times with ethanol and methanol and dried at 80°C for 15 min in oven, to remove the physisorbed APTMS molecules and any residue of solvent from the surface. The SEM image of developed APTMS over the silicon surface is shown in Fig. 3.5 (a), it confirms the crack free and uniformity of the deposited layer. At this initial stage we only consider the partial fabrication process of the proposed design wherein the aim is to investigate the morphology of TiO<sub>2</sub> and APTMS (as bio receptor) over silicon at the initial stage. That is the reason we adopted sol-gel processed TiO<sub>2</sub>. The APTMS is functionalized as a bio receptor element over TiO<sub>2</sub> as shown in Fig. 3.5

(b). Amines on the device surface are coupled with the amines on the capture agent. As silanization is a disordered process, multiple layers of silanes are deposited on the surface of the sensor by immersion of TiO<sub>2</sub> coated sample for 3 hours at room temperature in APTMS and ethanol solution. Silanization provides a base for bio-conjugation reactivity to modify the surface with capture agents. The observed experimental characteristics of these layers will be utilized in the fabrication of final device which will be the subject of near future research and will be published elsewhere.

### 3.4 Transmission and Sensing Characteristics

For the better performance of the device the optical field should be confined tightly in the slot region. To avoid the leakage of the optical field in the lower SiO<sub>2</sub> layer, a gold layer is inserted in the buried oxide layer which reflects the optical field and hence increases the optical field intensity in the slot region [139]. For creating the resonance in the slot waveguide, the gratings over the silicon rib in slot waveguide is introduced. The resonance increases the interaction time of light-matter to increase the sensitivity of the biosensing device. The slot and cladding (shown in Fig. 1 and Fig. 2) are filled with the analyte. The confinement factor in the slot region and the cladding medium (including the slot region) is defined as follows in Eq. (2.2)

The optical field confinement factor is 77%. The integrals are calculated inside the slot region and the entire clad region. The optical confinement factor considering the electric field of the y component because high-contrast waveguides such as silicon slot waveguides have a large y component of the E-field. The mode properties of propagation are controlled by the geometry of waveguide, the period  $\Lambda$  of silicon blocks, and the duty cycle. In periodic grating waveguides the field distribution of the mode changes periodically while propagating.

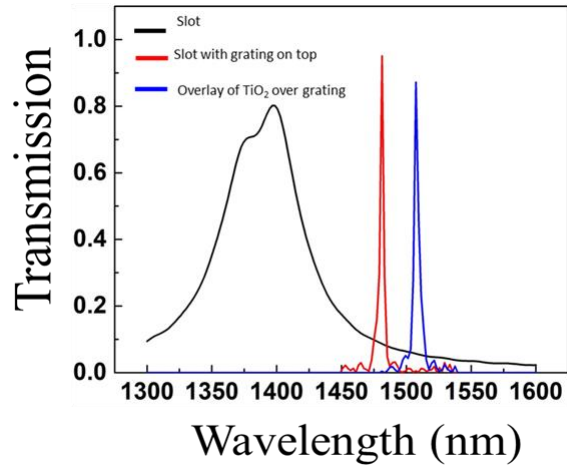


**Figure 3.6.** Simulated transmission spectra of the device with a 100 nm wide: black curve shows only slot waveguide with rib width of 400 nm and rib thickness of 220 nm; red curve shows grating on top of ribs beside slot region with a grating period of 300 nm and thickness of 100 nm; blue curve shows grating with 20 nm thick TiO<sub>2</sub> overlay.

In Fig. 3.6, the transmission spectra of the proposed device is shown which include (i) only slot region without grating, (ii) grating without TiO<sub>2</sub> overlay and (iii) grating with TiO<sub>2</sub> overlay. It is observed that on creating grating over silicon rib of slot waveguide the resonant wavelength peak (red color) becomes narrow as compared to the broad spectrum of slot waveguide (black color). After introducing TiO<sub>2</sub> over silicon grating the transmission peak (blue color) becomes sharp with FWHM of 4 nm.

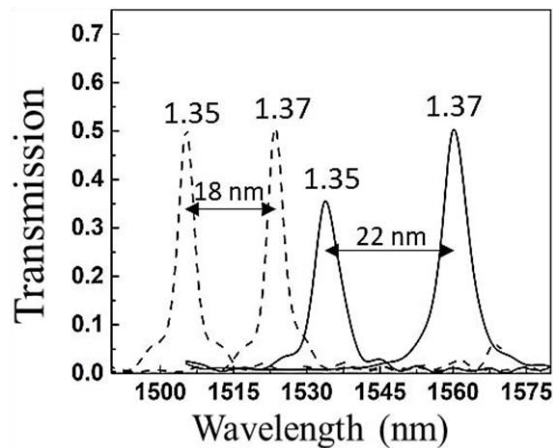


**Figure 3.7.** Shift in resonant peak when refractive index of analyte changes by 0.02. The dotted line shows shift in the peak without TiO<sub>2</sub> overlay and solid line shows shift with TiO<sub>2</sub> overlay on the grating.

The highest intensity of optical field confinement is observed in the slot region as compare in the grating region. The S parameter calculated is  $S_{21} = S_{12} = 0.81$ . We have observed that the transmission

spectra changes when the overlay of TiO<sub>2</sub> is applied over the silicon grating. As shown in Fig. 3.7, a larger peak shift is observed due to the presence of overlay material. TiO<sub>2</sub> is low absorptive material with high biocompatibility. The device shows large red shift in transmission on introducing TiO<sub>2</sub> over silicon grating. The interaction of resonating optical field with analyte takes place in the slot and a top grating layer of the device.

As shown in Fig. 3.7 with the change in the analyte, the effective refractive index of device changes and hence a shift of resonant wavelength is observed from  $\lambda$  to  $\lambda + \Delta\lambda$ . The change of analyte can be noted by measuring the variation in optical output power at a fixed resonating wavelength. The shift of 22 nm and 18 nm in resonant wavelength are respectively observed with and without TiO<sub>2</sub> overlay when the refractive index of the analyte is varied from 1.35 to 1.37. For resonance-based biosensors a narrower FWHM is desirable for a notable change in the resonance shift. In sensing applications, bulk sensitivity ( $S$ ) and figure of merit (FOM) are used to evaluate the sensing performance.  $S$  and FOM are respectively defined as  $S = \Delta\lambda_r/\Delta n_c$ ,  $FOM = S/FWHM$ , where  $\Delta n_c$  is the refractive index change,  $\lambda_r$  is the resonance wavelength change corresponding to the refractive index change. Fig. 3.8 shows transmission spectra of the device with the bio-samples of various refractive indices ranging from 1.37 to 1.39. A significant shift in the transmission spectra of resonant wavelength is

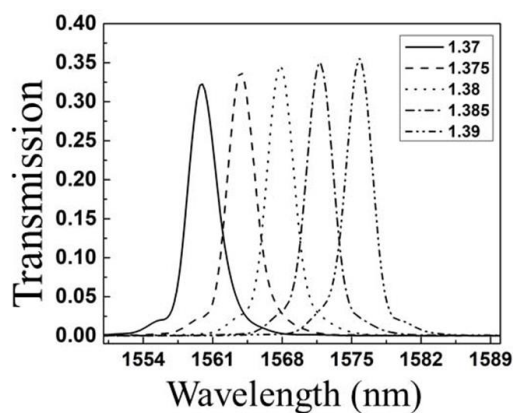


**Figure 3.8.** Simulated transmission spectra of the proposed device with TiO<sub>2</sub> overlay in which refractive index of analyte changes from 1.37 to 1.39. The grating period is kept 300 nm with slot width of 100 nm and with the thickness of 220 nm.

observed when the analyte index over the TiO<sub>2</sub> overlay is varied by 0.005 i.e., from 1.37 to 1.375. The observed spectra of resonant wavelength have a small FWHM of 4 nm leading to high FOM of 300, with sensitivity of 1200 nm/RIU for 20 nm TiO<sub>2</sub> overlay thickness. The change in resonant wavelength with change in the refractive index of the analyte with and without TiO<sub>2</sub> overlay is shown in Fig. 3.9.

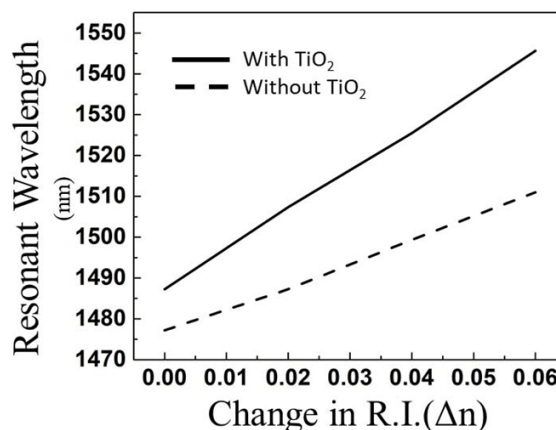


**Figure 3.9.** Variation in resonant wavelength with change in refractive index of the analyte. The refractive index is changed from 1.35 to 1.41 with an overall change of 0.06 which is common for bio-samples with various infections. The variation is observed with and without TiO<sub>2</sub> overlay with grating period of 300 nm and slot width of 100 nm.

The reference refractive index of analyte is kept at 1.35 and varied till 1.41 with an overall change of 0.06 which is common for bio-samples with various infections. The slope of resonant wavelength with TiO<sub>2</sub> overlay is larger as compared to the slope without TiO<sub>2</sub> overlay, indicating an increase in the resonance shift and hence a higher sensitivity of the device. From the above discussion it is clear that the high sensitivity is important parameter to achieve efficient sensing characteristics.

Table 3.1 illustrates the comparison of proposed work with previous reported work in terms of sensitivity, sensing area and fabrication process. In an MZI biosensor, the guided light is split by a Y-junction into two waveguides, one containing the sample, which is sensing arm, and the other is reference arm. MZI is easy to fabricate and have large sensing area [89].

**Table 3.1:** Comparison of sensitivity (s) reported in various sensors

| Sensor type                                | Sensitivity (nm/RIU) | Remarks  |
|--|----------------------|--|
| <b>Mach Zander Interferometer</b> [89]     | 1061                 | Large sensing area, Easy fabrication process     |
| <b>Photonic Crystal based</b> [140], [141] | 1000                 | Large sensing area, Complex fabrication process  |
| <b>Grating based</b> [142]                 | 580                  | Large sensing area, Complex fabrication process  |
| <b>Ring Resonator based</b> [143]          | 1060                 | Large sensing area, Moderate fabrication process |
| <b>Proposed work</b>                       | 1200                 | Small sensing area, Moderate fabrication process |

On the other hand, the sensors based on surface plasmonic resonance show moderately high sensitivity with complex optical coupling schemes which hinder their commercial applications [144]. Photonic crystal cavity built in one- or two-dimensional structures has high Q-factor, strong light-matter interaction, high sensitivity and large surface area. Grating based structure with a periodic modulation in the propagation direction of the optical mode similar to 1D photonic crystals provide high Q factor but with low sensitivity [142].

### 3.5 Fabrication Tolerance

Analysis of the fabrication tolerance of the proposed device is also performed numerically to include the errors during fabrication of the device. The effect of a change in grating depth, grating period, overlay thickness and rib width is observed numerically on the device performance. The effect of the overlay thickness on the sensitivity of the device is shown in Fig. 3.10, in which refractive index of the analyte (bio-samples) is varied from 1.35 to 1.37.

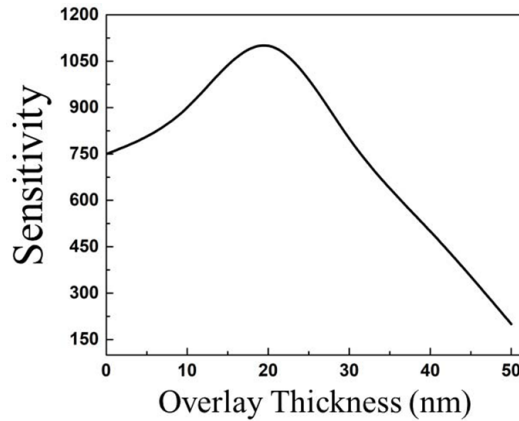


**Figure 3.10.** Effect of variation of TiO<sub>2</sub> overlay thickness on the sensitivity of device. The grating period is kept at 300 nm with a slot width of 100 nm

Grating period, duty cycle and slot width are optimized at 300 nm, 33 % and 100 nm. The highest sensitivity of 1107 nm/RIU is obtained at 20 nm thick TiO<sub>2</sub> overlay. The overlay thickness is varied from zero nanometre (no overlay) to 50 nm. Beyond 50 nm resonance appears to diminish resulting in greater FWHM. The sensitivity is 750 nm/RIU without overlay, when overlay thickness increases beyond 20 nm, the device sensing performance starts degrading and sensitivity falls to 200 nm/RIU for 50 nm thick overlay. The calculated group index is 4.13 with a Q factor of 1154 without TiO<sub>2</sub> overlay, as the thickness of the TiO<sub>2</sub> overlay increases the Q factor reduces to 594.

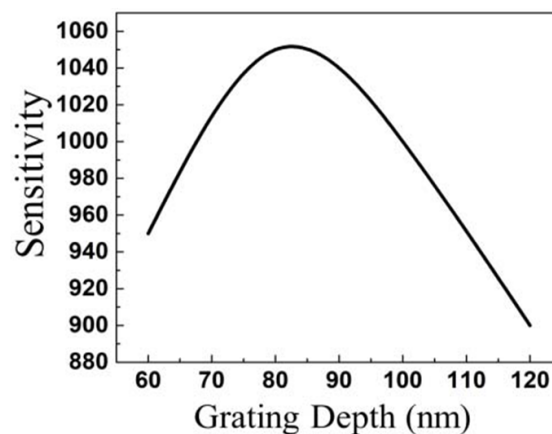


**Figure 3.11.** Effect of grating depth on the sensitivity with no TiO<sub>2</sub> overlay. The grating period and silicon rib width are 300 nm and 400 nm, respectively.

Fig. 3.11 shows the effect of grating depth ‘d’ on the sensitivity of the proposed device without TiO<sub>2</sub> overlay.

With the variations in ‘ $d$ ’ the device shows an acceptable change in the sensitivity. The highest sensitivity of 1040 nm/RIU achieved at  $d = 90$  nm. The sensitivity increases from 950 to 1040 nm/RIU on increasing the grating depth from 60 nm to 90 nm. These variations or errors in the grating depth are common for grating fabrication. As the thickness further increases from 90 nm to 120 nm, we observe a fall in the sensitivity which still remain at an acceptable level without degrading the device performance.

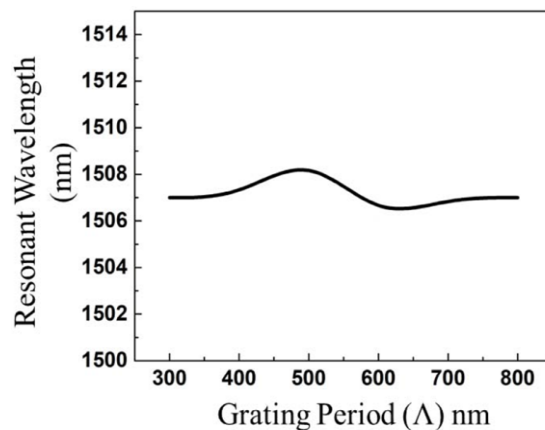


**Figure 3.12.** Effect on resonant wavelength shift on variation of grating period with grating thickness of 100 nm, rib width of 400 nm and slot width of 100 nm.

In Fig. 3.12, even a large change in the grating period shows a very small change in sensitivity of the device. Usually, the change in the grating period significantly affects for the resonance condition. The negligible variations are observed when the grating period is varied from 300 nm to 800 nm with a grating height of 100 nm and a grating width of 400 nm. The variation in resonant wavelength is found to be within acceptable range on the variation of the grating period. Hence the proposed device can easily accommodate common errors, in terms of variations in grating depth and period, occurred during device fabrication. To further analyze the fabrication tolerance of the device, effect of variations in each silicon rib width is studied on the sensitivity as shown in Fig. 3.13. The widths of each rib are varied from 300 nm to 500 nm with and without TiO<sub>2</sub> overlay. The sensitivity without TiO<sub>2</sub> overlay varies from 900 roughly to 1000 nm/RIU while it varies from 1000 to 1200 nm/RIU.

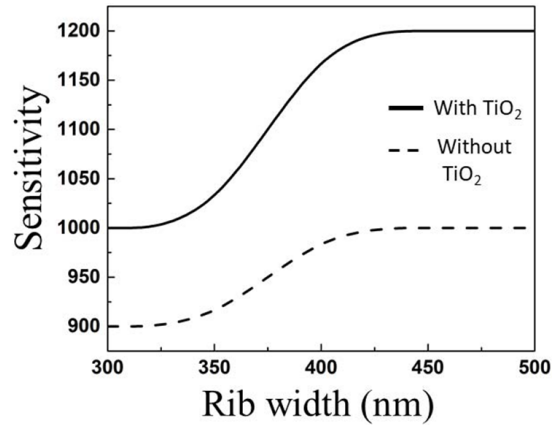


**Figure 3.13.** Effect of variation in silicon rib width on the sensitivity with (solid line) and without TiO<sub>2</sub> (dotted). The grating period is kept at 300 nm with a slot width of 100 nm.

It is observed that wider silicon ribs result in the improved sensitivity. This is because wider rib increases the optical mode area and thus improves the interaction of light with analyte present in the slot and grating region. Below 300 nm and beyond 500 nm, the optical confinement becomes weak. The range of variation of rib width from 400 nm to 500 nm is more favourable where sensitivity remains high. Below 400 nm of the rib width sensitivity drops down to 1000 nm/RIU with overlay which is still at an acceptably high level.

### 3.6 Summary

A nanophotonic biosensing device with a high sensitivity of 1200 nm/RIU is proposed. For effective selectivity and sensitivity of the analyte a small FWHM is desirable which is observed to be 4 nm in the proposed device. To increase the biocompatibility and sensitivity of the proposed device an overlay of TiO<sub>2</sub> on silicon/air grating is adopted. The gold layer under top TiO<sub>2</sub> is used to suppress the leaky mode in bottom cladding region. The introduction of the grating with TiO<sub>2</sub> overlay in the slot region provides a quasi-resonance in the low index region where the analyte resides which leads to strong light-analyte interaction. The surface functionalization of bio-receptors on silicon is studied and the measured characteristics are incorporated into the simulation for near-to practical results. We experimentally analyse the morphology of thin films of, underlying layer of gold in SiO<sub>2</sub>

cladding, TiO<sub>2</sub> as an overlay material and APTMS as bio-receptors. The device design provides a flexibility to accommodate bio samples of various size in a desired width ranging from few hundred nanometres to few micrometres. The proposed device can detect very low change in refractive index of analyte with a moderately less complex process flow.

## Chapter 4

### Engineered Slot Waveguide for Optical Detection of Viral Infections

A nanophotonic biosensing platform based on an engineered slot waveguide is proposed. The proposed device based on Fano resonance which consists of a periodic arrangement of two rows of nano-disks and rectangular grating. The periodically arranged nano-disk structure in the form of engineered slot waveguide provides enhanced light-matter interaction and easy accommodation of bio-samples. The surface morphology of (3-Aminopropyl) trimethoxysilane (APTMS) as a functionalized layer on the silicon surface is experimentally analysed. The proposed sensor device can detect very small refractive index change of 0.0008. Based on refractive index sensing, the device numerically exhibits a high sensitivity of 1463 nm/RIU for some viral infections including hepatitis B the with a Figure of Merit (FOM) of 471 for refractive index change of 0.02. The limit of detection for the proposed device is  $1.02 \times 10^{-3}$  RIU (Refractive Index Unit). The proposed scheme with Fano like resonance spectrum carries a great potential for on-chip and off-chip nanoscale optical devices and sensors.

#### 4.1 Generation of Fano Resonance

In 1961, asymmetric autoionization spectra of He atoms was discovered which further known as Fano resonance [145]. Fano resonance is a special type of asymmetrical resonance in the integrated photonic devices which can be used for the detection of bio-samples. This Fano resonance originates from the interaction of the broad resonance (or continuum state) with a narrow resonance (or discrete state). The directly excited broadband continuum states are known as bright modes and the modes which cannot be addressed are known as dark mode of discrete resonances [146]. Asymmetric resonances like

Fano resonance can be achieved by modification in the periodic structure to make it operate at various wavelength ranges in-between visible to infrared. The Fano resonance can be created by bringing the proper symmetry in breaking the nano-rod structures. Moreover, the periodic arrangement of the nanorods reduces the radiative losses of the guided optical mode [94], [96]. In the past few years, an enormous amount of research has been done to demonstrate the Fano resonance in periodic plasmonic nanostructures and metamaterials [103], [147]. To achieve strong interaction of analyte and optical field, the combination of grating and slot waveguide is favourable, where a large amount of quasi (Transverse Electric) TE mode will be concentrated in the low index region [57], [148]. The requirement of strong optical confinement in subwavelength devices is fulfilled by the slot waveguide structure. The grating waveguide support low-loss optical modes that propagates in the wave-guiding region and enhances the field overlaps with analytes and suppresses reflection [149], [150]. After optimizing the device parameters, the combination of nanophotonic grating structure (nano-disk embedded with rectangular grating) with slot waveguide gives an advantage to better control the tightly confined guided mode in slot region.

Here, we propose a nanophotonic device for the label-free detection of viral infection utilizing Fano resonance in an engineered slot based optical waveguide. The proposed device is composed of periodically arranged nano-disk with rectangular grating connected between a pair of nano-disk which is separated into two parts to form a slot region. The confined optical mode propagates in a 75 nm wide low-index slot-region where biomolecules of the target analyte are present. Here APTMS is used as a functionalized layer to support immobilization of antibodies to bind antigens. HBsAg is a small DNA virus and it belongs to the Hepadnaviridae family [151]. The HBsAg obtained after purification from human hepatoma cell lines and human primary hepatocytes [138], [152]. The size of HBsAg is 22 nm and in 1  $\mu\text{g/ml}$  and it forms the thickness of 4 nm over the functionalized surface [153]. Due to the intense electric field distribution and strong light-

matter interaction, the proposed sensor device manifests bulk sensitivity of 1463 nm/RIU for 0.02 refractive index change of analyte with FOM of 471 and limit of detection of  $1.02 \times 10^{-3}$  RIU<sup>-1</sup>. The proposed device exhibits promising results to detect the virus analytes with the smallest refractive index change of 0.0008 in serum medium with the sensitivity of 937 nm/RIU.

#### 4.2 Nanophotonic Engineered Slot Waveguide

The proposed nanophotonic biosensor based on engineered slot waveguide device on a silicon-on-insulator (SOI) substrate is shown in Fig. 4.1. In the proposed design, two rows of silicon nano-disks are arranged periodically in the direction of propagation. The radius, period and thickness of nano-disk are kept at 175 nm 500 nm and 220 nm respectively. A rectangular grating which connects each pair of nano-disks is broken from the centre to form the slot region. The width and thickness of rectangular grating are 150 nm and 220 nm, respectively.

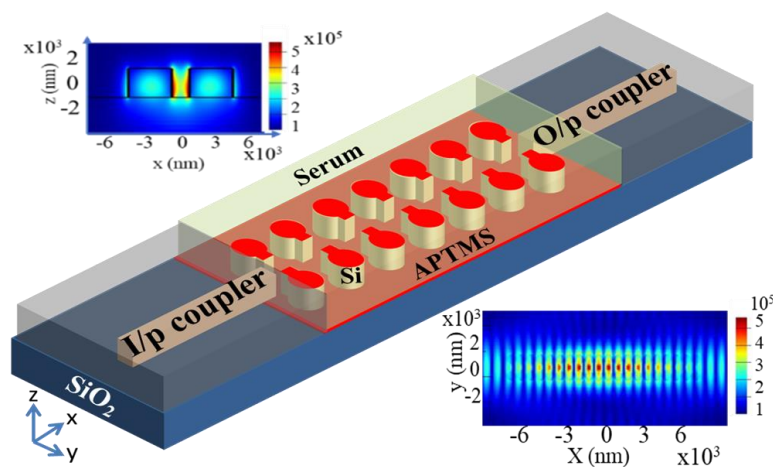


**Figure 4.1.** Schematic of the proposed bio-sensor based on engineered slot waveguide device on SOI substrate. The silicon nano-disk radius, thickness and period are 175-nm, 220-nm and 500 nm respectively. Inset shows optical confinement in slot region

Nano-disk radius and grating width are kept at subwavelength dimensions to ensure mode confinement and to suppress diffraction effects. The propagation of the optical field is shown in inset of Fig. 4.1. The periodicity of nano-disk and the rectangular grating is smaller than the wavelength of the incident light which satisfies the condition

$\Lambda < \lambda/2 \cdot n_{\text{eff}}$  to operate in the subwavelength regime where  $\Lambda$  is period,  $\lambda$  is the operating wavelength and  $n_{\text{eff}}$  is the effective refractive index [45].

The duty cycle defined by  $DC = L_{\text{Si}} / \Lambda$ , where  $L_{\text{Si}}$  is the diameter of nano-disk. The dimension for the silicon box is taken the same as the standard silicon substrate for photonics applications, the 3  $\mu\text{m}$  oxide thickness over the silicon substrate to prevent leakage of optical modes. The working top silicon thickness in all cases is 220 nm as per foundry standard. This nano-disk array with rectangular grating is separated by a low index region of width 75 nm. The period of the rectangular grating is kept same as nano-disk. High electric field intensity concentrated between the nano-disk array and rectangular grating can be observed in the inset of Fig. 4.1. Electric field intensity in the slot region with viral infection like HBsAg and without any sample (air) is shown in Fig. 4.2.

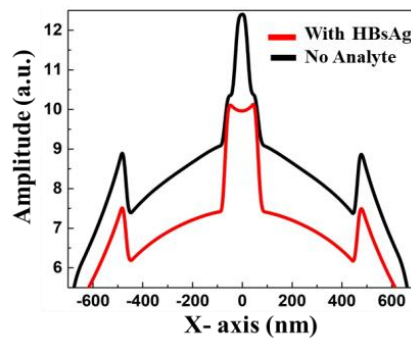


**Figure 4.2.** Electric field intensity of device with viral infection like HBsAg and without any sample. (c) Fano resonant mode propagation in 75 nm slot region

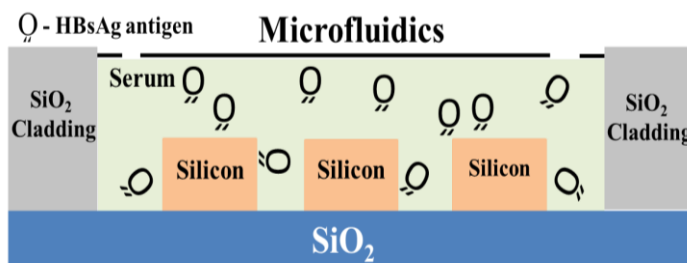


**Figure 4.3.** Side View of proposed device with a simple microfluidic channel

A maximum part of optical mode propagates in the slot region and overlap with grating structure. The electric field intensity is higher for

air cladding and it decreases when cladding changes to viral infection biomarker. The resonant optical mode is created in slot region is due to the periodic arrangement of nano-disks with the embedded grating structure. The active sites for the analyte increase due to the periodic nature of waveguide which results in improvement of refractive index sensitivity. The top view of one pair of nano-disk with rectangular grating broken at the centre to form the slot region.  $S_g$ ,  $r$  and  $w$  are the slot gap, radius of nano-disk, and grating width respectively. Polydimethylsiloxane (PDMS) microfluidic channel will be formed to flow the serum and virus antigen in a controlled way over the device. Fig.4.3 shows the side view of the proposed device with  $\text{SiO}_2$  cladding at both the sides of the structure and incorporated PDMS microfluidic channel. The sensing area is covered with serum and target bio-analyte.

To optimize the maximum optical field confinement in the slot region and to enhance modal overlap, nano-disk radius, grating width, slot width and period are optimised. The grating structure induces the resonance in the device and increases the light-matter interaction. The optical mode formed in the proposed device is the combination of slot mode and Bloch mode. The discontinuity of electric field at normal boundary between silicon and air (high refractive index contrast) with narrow slot region generates slot mode. The Bloch mode obtained by a periodic arrangement of silicon-air blocks in direction of propagation having a period in the subwavelength range [149]. Simulation of the device is performed on Lumerical software. The mesh type is taken auto-non uniform, the resolution is set to 10 nm with an accuracy of 5 and mesh refinement is set to conformal variant 0, to mimic the practical device behaviour. The time step taken is 0.04 femtosecond. The broadband wavelength source is used from 1500 nm to 1700 nm. The perfectly matched layer (PML), metal and periodic boundary conditions are applied in y-axis, z-axis and x-axis respectively. The window size of y, z and x-axis is 7000 nm, 5000 nm and 300 nm for a single cell

### 4.3 APTMS Functionalization and Susceptibility

Self-assembling layers of silane have high physical and chemical stability for covalent immobilization. Following this approach, bioactive layers (or linkers) are formed uniformly with little effect of denaturation of proteins. Bioactive layers interact with the functional group of silane with one of their ends and attaching protein molecules to the surface at another end. The proteins can be antigen, antibodies, DNA or cell binding proteins [154]. We characterize the APTMS silane layer numerically and experimentally as functionalization surface for binding of virus antibodies like anti-HBV for detection of HBsAg surface antigen. The partial experimental study of APTMS which is required in the fabrication process of the final device is presented. APTMS is prepared, deposited and analyzed experimentally on silicon. For numerical calculation, the refractive index of APTMS is taken as 1.433 and serum is taken as analyte medium. APTMS layer deposited over the proposed device as the functionalized surface for attachment of virus antibody. The susceptibility  $\left\{ \frac{\partial n_{\text{eff}}}{\partial t} \right\}$  for surface sensing applications is calculated [155] for proposed device and compared with conventional slot waveguide using Lumerical Mode Solutions simulator.

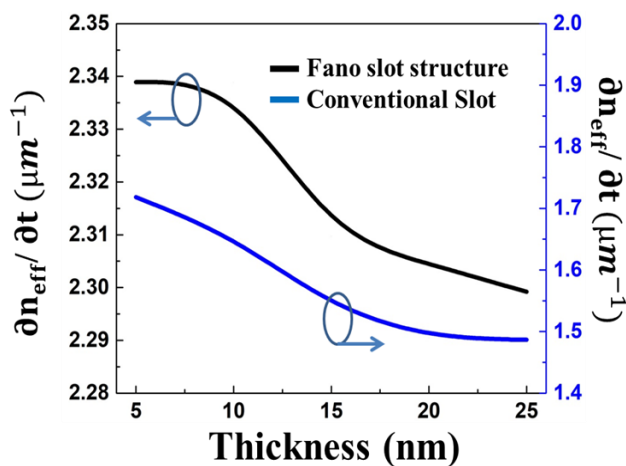


**Figure 4.4.** Comparing  $\partial n_{\text{eff}} / \partial t$  as the thickness of APTMS surface layer on proposed device with conventional slot waveguide.

The device parameters nano-disk radius, grating width and slot width selected for simulation of the proposed device are taken as 175 nm,

150 nm and 75 nm respectively. The  $\partial n_{\text{eff}} / \partial t$  of the conventional slot waveguide is calculated with rib width of 350 nm and a slot width of 75 nm. Fig. 4.4 shows the simulated results of the susceptibility of the proposed device and slot waveguide. The  $\partial n_{\text{eff}} / \partial t$  is larger in proposed Fano structure slot waveguide than in conventional slot waveguide due to high mode overlapping factor of 0.3. For APTMS as a functionalized surface layer, the susceptibility is highest at a thickness of 5 nm and starts decreasing as the thickness of the surface layer increases. Susceptibility is also known as mode sensitivity, where a portion of optical mode intensity interacting with the sample. On increasing, surface layer thickness interaction with optical mode exists between nano-disk and rectangular grating decreases, which results in degradation of surface sensitivity. The APTMS as the functionalized surface layer is deposited on the silicon surface by silanization. Silanization is done by the absorption of tri-ethoxy molecules and condensation of hydroxyl groups on the silicon surface. APTMS silane is best for bio-functionalization of sensor surface due to high reactivity with aldehyde and epoxy.

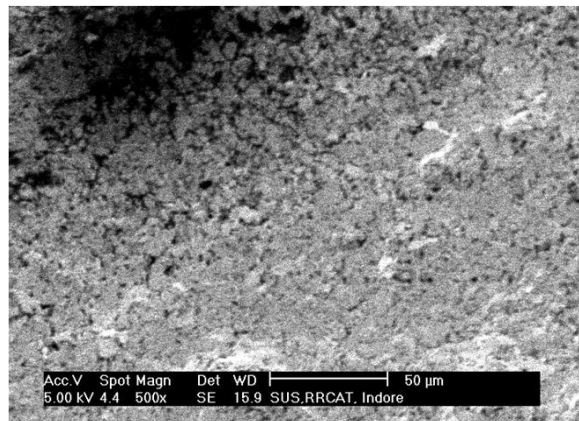


**Figure 4.5.** SEM image of APTMS over intrinsic Si <100> substrate deposited after 3 hours of immersion in solution.

The silanization of nanocomposite material is carried out by mixing a 3-mM solution of 3-aminopropyltrimethoxysilane (APTMS) in ethanol as a solvent. For silanization reaction, the silicon wafer placed in the petri dish for 3hrs at room temperature. After silanization, the silicon wafer is washed for two times by methanol and dried up in hot air oven for 15 min at 80°C. The SEM image of developed APTMS over the

silicon surface is shown in Fig. 4.5. The SEM confirms that APTMS layer binds to silicon surface is crack-free, smooth and uniform. The APTMS as surface functionalization layer can deposit up to few nanometres under controllable environment. Longer reaction time causes APTMS to polymerize to form multiple layers of non-uniform morphology. This experimental characteristics of functionalized layer APTMS can be utilized to bind the protein and antibodies for sensing characteristics of the final device which will be the subject of the near future and will be published elsewhere.

#### 4.4 Propagation Characteristics

For better performance of the proposed device optical field must be confined in slot region and in between the gratings. Nano-disks embedded with rectangular grating helps to create resonance in the device. When optical modes of nano-disk and rectangular grating are coupled, a dip and peak (Fano profile) occur in the transmission spectra. High optical resonance in the slot region increases the light-matter interaction which improves the performance of the device. The confinement factor in the slot and cladding region is calculated by Eq. (2.2). The calculated confinement factor is 82%.

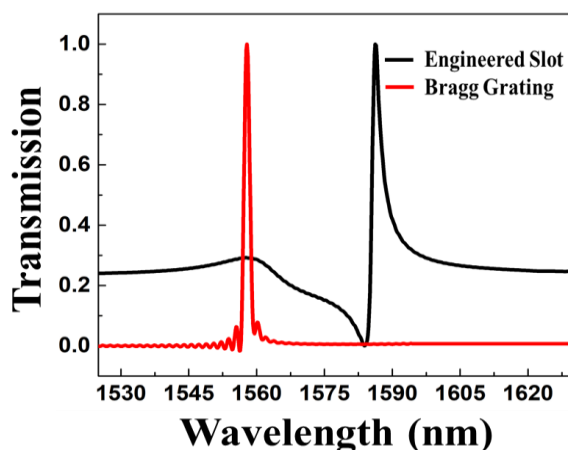


**Figure 4.6.** Simulated transmission spectra of Bragg grating (red) and Fano structure (black). For Bragg gratings waveguide the width and thickness is 350 nm and 220 nm with period of 500 nm and duty cycle is 60%. For Fano structure Nano-disk radius is 175 nm, grating width is 150 nm, slot width kept at 75 nm and period is 500 nm.

The transmission spectra is shown in Fig. 4.6 includes (i) Bragg grating structure (ii) proposed Fano waveguide structure. It is observed that Bragg grating structure generates a narrow resonant peak (red colour) of 0.9 nm linewidth while engineered slot with nano-disk combined with rectangular grating generates Fano profile (black colour) with a linewidth of 1.6 nm. The transmission spectra of the proposed design are simulated by varying the design parameters. The coupling between different resonant modes forms the Fano resonance modes.

Metal nanostructures undergo large ohmic losses intrinsically, which results in the limitation of Q factor and spectral variation and prohibits improvement in performance [101]. Resonance tailoring in Fano profile is correlated to the radius of nano-disks. Silicon nano-disk 1-D array supports cumulative resonance by considering collective excitation of the single nano-disk and attached grating in slot waveguide. Period, shape and background index determines the resonant frequency in the waveguide. The peak wavelength of Fano resonance is mainly affected by the change in nano-disk radius (duty cycle) and not affected by the variation in periodicity of nano-disk or embedded grating width. The intensity and direction of the electric and magnetic field depend on the dimensions of cylinder type geometry i.e. nano-disks [110], [111].

The mode position in nano-disk is estimated by magnetic wall boundary conditions, this exhibits a stronger wavelength shift of electric resonance with respect to nano-disk diameter. Fig. 4.7 shows the transmission spectra of the proposed structure for variation in radius of silicon nano-disk from 150 nm to 200 nm with grating width fixed at 150 nm and slot width kept at 75 nm. As the radius of nano-disk increases, the resonant wavelength shift becomes large and the Fano profile become broad with the high value of FWHM. We observe from Fig. 3.20 that Fano profile generated by the nano-disk radius of 150 nm have low FWHM value compared to 175 nm and 200 nm radius. With the increase in the nano-disk radius the duty cycle

increases which results in a reduction in low index region and increment in high index material dimensions. This change in duty cycle diffracts energy of resonant mode out of the structure instead of resonating in the gap which leads to larger FWHM. When we keep the duty cycle (>60%) the evanescent field penetrated deeper into the cladding and optical mode confinement in the core region (between the silicon blocks) is reduced. Weaker confinement in device enhances modal overlap with an analyte. This results in enhancing the light-matter interaction by keeping enough energy to guide in the device. To maintain the Fano profile spectrum intact, the value of the duty cycle kept between 60% to 80% for a period of 500 nm. Therefore, by selecting a 60% duty cycle (radius 150 nm), a proper balance is formed between photon analyte interaction and losses for detection of virus. The devices with a 60% duty cycle are easier to fabricate and enhance the sensitivity with a thickness of 220 nm.

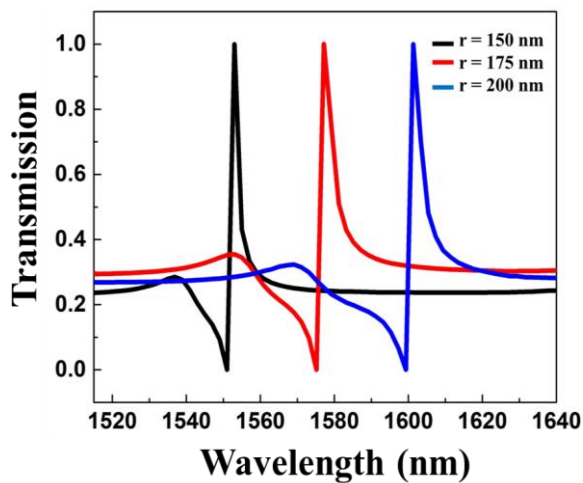


**Figure 4.7.** Simulated transmission spectra of proposed device with variation in nano-disk radius from 150 nm to 200 nm. The grating width is kept constant at 150 nm with period of 500nm.

When nano-disk radius increases beyond 200 nm the Fano profile deteriorates and spectrum gets broaden, which results in high FWHM. The wavelength shift introduced by variation in the embedded grating is insignificant with respect to nano-disk diameter variation. The Fano spectrum of the proposed device is a collective resonance determined by asymmetrical shape, period and refractive index of the analyte, which is a serum in this case. The calculated group index [156] of the

proposed device is 6.34 at 1550 nm for nano-disk radius and grating width at 150 nm. The slow down factor (SF) is 18, calculated by  $SF = c\tau/2\Lambda N$ , where  $\tau$  is the group delay,  $\Lambda$  period of proposed device and  $N$  is the total number of the grating in the proposed design. The use of susceptibility and group index with a slowdown factor are parameters which can be used for surface sensing application.

#### 4.5 Bulk and Surface Sensing Characteristics

The reradiated fields of oscillations of particles which are in-phase and anti-phase with incident light interfere constructively and destructively lead to the formation of bright modes and dark modes. Dark mode exhibits properties like the elimination of scattering loss, narrow resonance linewidth and high sensitivity due to weak coupling to free-space radiation. Bright mode couples light effectively which enhances the transmission. In sensing applications, bulk sensitivity and figure of merit (FOM) are important sensing parameters to evaluate the sensor performance. The sensitivity (S) of the refractive index sensor is defined by  $\delta\lambda / \delta n$ , FOM is defined by  $FOM = S/FWHM$  and Q factor calculated by  $Q = \lambda/FWHM$  where  $\delta n$  is the refractive index change,  $\delta\lambda$  is the resonance wavelength change corresponding to the refractive index change and FWHM is full width half maximum. Asymmetric line shape and narrow linewidth of Fano resonance exhibit high-quality factors. For high Q factor in nanostructures, radiative losses induced by bright mode should be minimized and it must efficiently excite the dark resonance by surpassing the material losses.

The nano-disk with embedded grating creates the Fano resonance and exhibits strong optical confinement in the slot region. The top cladding of the device assumes to be filled with serum. The serum obtained after centrifuging of whole blood. The refractive index of the whole blood is calculated by selleimier equation 4.1 [157].

$$n^2(\lambda) = 1 + \frac{A_1\lambda^2}{\lambda^2 - B_1} + \frac{A_2\lambda^2}{\lambda^2 - B_2} \quad (4.1)$$

where  $A_1 = 0.7960$ ,  $A_2 = 5.1819$ ,  $B_1 = 1.0772 \times 10^4$ ,  $B_2 = -7.8301 \times 10^5$

$$n_s = A + \frac{B}{\lambda^2} + \frac{C}{\lambda^4} \quad (4.2)$$

where  $A = 1.3350$ ,  $B = 4.6513 \times 10^3$ ,  $C = -1.3069 \times 10^8$

After centrifugation of whole blood at 3000 rpm for 10 min serum is obtained. The refractive index of serum can be calculated by the Cauchy equation [157]. The refractive index of the virus biomarker is calculated by the [158]

$$n = n_s + \frac{dn}{dc} c \quad (4.3)$$

where  $n_s$  is the refractive index of solvent (serum) which is calculated by Eq. (4.3),  $dn/dc$  is the refractive index increment and  $c$  is the concentration. The proposed biosensor with serum as cladding medium is able to detect viral infections with  $dn/dc = 0.165$  ml/gm which includes Hepatitis B surface antigen HBsAg [138]. Fig. 4.8 depicts the shift in Fano resonance peak with the variation of the analyte refractive index. The refractive index 'n' (using eq. 2.9) increases from 1.3377 to 1.3425 with a step of 0.0008 RIU for different concentrations of analytes.

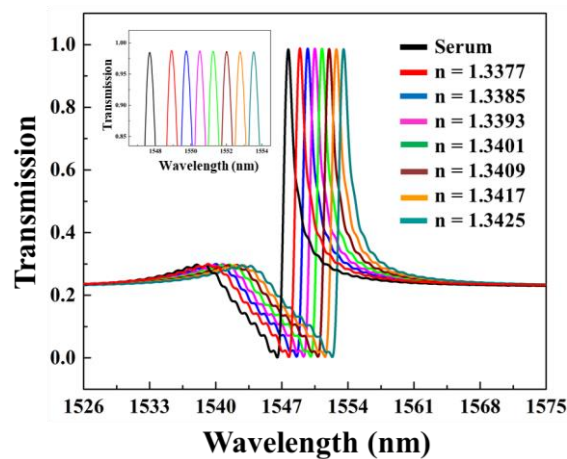


**Figure 4.8.** Simulated transmission spectra of the proposed device with refractive index of analyte changes from 1.3377 to 1.3425. The grating period is kept 500 nm and with the thickness of 220 nm. Inset shows zoom in of resonance peaks.

Structural parameters like nano-disk radius, grating width, slot width and period are fixed at 150 nm, 150 nm, 75 nm and 500 nm respectively. The observed spectra of resonant wavelength have a small FWHM of 1.2 nm leading to a sensitivity of 937 nm/RIU. The highest Q factor of 1291 is obtained when nano-disk radius to height ratio is kept at 0.68. In the inset of Fig. 3.21 resonant peaks are shown and we observe that peaks are distinguished and shifted by 75 pm with a change in refractive index. Fig.4.9 shows the transmission spectra of the proposed device with bio analytes of different refractive indices ranging from 1.38 to 1.44. By varying the refractive index of analyte, a larger wavelength shift to new Fano resonance peak is observed. The reference refractive index of the top cladding is kept at 1.38 and varied till 1.44 with a change of 0.02 which is near to the practical value of proteins, bio-samples and biomarkers. The largest resonant peak shift observed is 29.26 nm with the nano-disk radius of 200 nm, when the refractive index of analyte varied from 1.40 to 1.42 RIU.

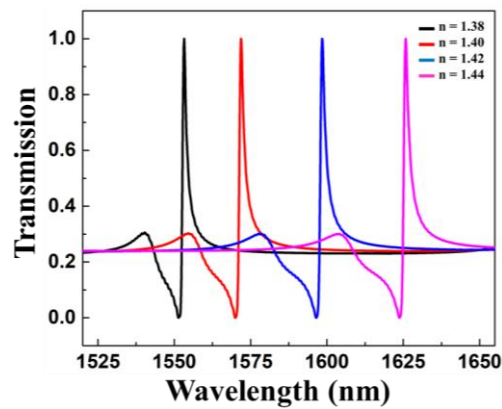


**Figure 4.9** Simulated transmission spectra of the proposed device with nano-disk radius, grating width and slot width at 175 nm, 150 nm and 75 nm, in which refractive index of analyte changes from 1.38 to 1.44. The grating period is kept 600 nm and with the thickness.

The sensitivity observed with 0.02 RIU change in analyte refractive index is, 1219 nm/RIU, 1306 nm/RIU and 1463 nm/RIU for the nano-disk radius of 150 nm, 175 nm and 200 nm respectively. The radius of the silicon nano-disk influences the bulk sensitivity of the device. The figure of merit of the sensor is 471. The relationship between Fano resonances peak shifts and different refractive index of analytes are

analysed for the variation in nano-disk radius shown in Fig. 4.10. Inset shows the shift in resonance peak for change in refractive index by 0.0008 RIU.

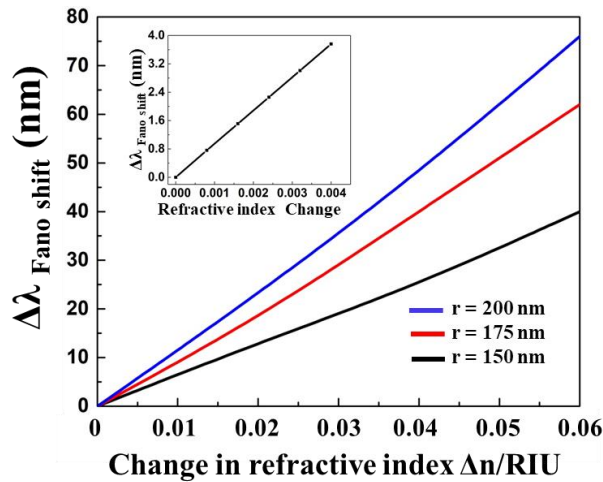


**Figure 4.10.** Variation in Fano resonant wavelength with the change in the analyte with different refractive index. The refractive index is changed from 1.38 to 1.44 with overall change of 0.02. The variation is observed with different nano-disk radius. Grating period and slot width kept at 150 nm and 75 nm. Inset shows the Fano peak shift with change in refractive index of 0.0008 for HBsAg sensing.

The sensitivity observed for 0.0008 RIU change in refractive index is 937 nm/RIU. The slope of the shift in resonant wavelength for nano-disk of radius 200 nm is larger compared to nano-disk of radius 175 nm and 150 nm, which indicated higher sensitivity of device with broad FWHM. For virus biomarker detection, the nano-disk radius of 150 nm is preferred because of the low value of FWHM of 1.2 nm compared to 3.1 nm FWHM of 200 nm nano-disk radius. The low value of FWHM is preferred for better detection of very small change in the refractive index of the analyte. The limit of detection (LOD) is also a fundamental parameter to evaluate sensor performance. LOD is defined by  $DL = \lambda/Q \times S$ , where S is the bulk sensitivity, Q is a quality factor and  $\lambda$  is the resonant wavelength. The minimum value for we calculated value is  $1.02 \times 10^{-3} RIU^{-1}$ . In proposed device low DL can be realized with high bulk sensitivity and Q factor. High sensitivity and Q factors are important parameters to achieve high sensing characteristics.

Table 4.2 shows a comparison of the proposed work with other reported sensors in terms of sensitivity, Q factor and total sensing area.

**Table 4.2:** Comparison of various reported nanophotonic biosensors with the proposed device.

| <b>Sensors</b>                            | <b>Sensitivity<br/>nm/RIU</b> | <b>Quality<br/>Factor</b> | <b>Sensing<br/>Area</b> |
|---|-------------------------------|---------------------------|-------------------------|
| <b>Bragg<br/>Grating</b><br>[159]         | 579                           | 8000                      | $\sim 28 \mu\text{m}^2$ |
| <b>MIM<br/>Resonator</b><br>[108]         | 1160                          | 73                        | $\sim 18 \mu\text{m}^2$ |
| <b>SWG<br/>resonator</b><br>[160]         | 366                           | 12900                     | $\sim 80 \mu\text{m}^2$ |
| <b>Nanoslits</b> [6]                      | 926                           | 224                       | $\sim 25 \mu\text{m}^2$ |
| <b>This work<br/>(0.02) RI<br/>change</b> | <b>1463</b>                   | <b>516</b>                | $\sim 10 \mu\text{m}^2$ |

In Multi-box Bragg grating structure [159] where the periodicity is present in the propagation direction and also in the transverse direction, provide high Q factor with more fabrication errors. MIM double-ring resonator [108] shows high sensitivity, strong light-matter interaction and small sensing area and generate a considerable evanescent field for the interaction of light and matter. SWG Ring resonator [160] designed with the periodicity in direction of propagation with features of high Q factor, sensitivity and large sensing area. Nano slit arrays [6] in the form of grating exhibits high sensitivity and advantage of multiplexed detection with the moderate fabrication process and small sensing area. The proposed device attributed to Fano resonance characteristics is numerically shown to

achieve efficient optical detection with high sensitivity and small footprint.

In another application of biosensing Fano resonance-based slot waveguide can be used for the detection of proteins and polysaccharides present in human blood. Human blood plasma consists 90% of water and 10% with albumin[161]. Albumin is natural protein used to coagulate human blood during surgery. Mainly the colloidal osmotic pressure of blood is regulated by albumin. Albumin is fatty acid free used to dissolve lipids. When albumin infused in blood it starts increasing the colloid osmotic pressure. The interstitial fluid forced into intravascular compartment and overall volume of circulatory system increases[162]. Dextran function is to improve the microcirculatory flow in surgical implantations. These polysaccharides, replace volumes of blood as they are able to multiply the plasma volume, also known as plasma expanders. Dextran oncotic pressure is higher than plasma and fluid starting flow from tissues to bloodstream. In another application infusion of dextran in blood cause increase the refractive index of plasma so that light can penetrate in blood stream for optical coherence tomography[163], [164]. The intravascular volume of tissue edema restores by use of colloids. Type of colloid and volume status determines the clinical responses of ill people at initial stage of administration. Albumin is the natural colloid and dextran is the non-protein colloids [163]. Albumin is the natural protein found in abundantly in blood and accounts for 50% of blood plasma. It is natural colloid solution with single polypeptide chain of 585 amino acids and molecular weight of 69kDa. Albumin is synthesized by liver and contribution of albumin for normal oncotic pressure is 80%. Human albumin does not have any carbohydrate [162]. Dextran are highly branched polysaccharide molecules which use as artificial colloid [164]. It is polymer of 70kDa molecular weight with 6% of oncotic solution. Bacterial enzyme dextran sucrose is used to synthesized Dextran, by growing bacterium (B512 strain) in sucrose medium. Dextran are used for plasma expansion. This engineered

nanophotonic slot waveguide structure is also used for the detection of polysaccharide dextran in natural protein albumin.

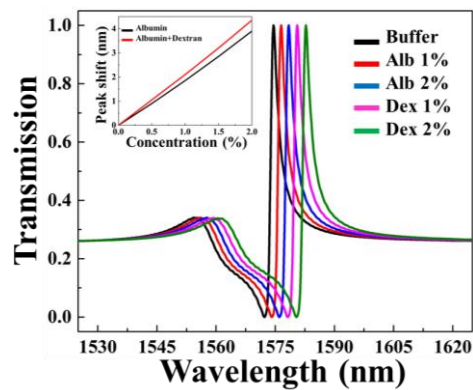


**Figure 4.11.** Transmission spectra of proposed device with buffer, albumin and dextran added in albumin with 1% - 2% concentration.

For detection of albumin and dextran in PBS buffer solution, the top surface of device assumes to be filled with PBS buffer which act as cladding for optical confinement. The refractive index of PBS can be calculated by Sellmeier equation Eq.2.8 The refractive index of albumin and dextran are calculated by Eq.2.9. The refractive index increment percentage of albumin and mixture of albumin and dextran is 0.0018 and 0.00205[165]. The Fano resonance transmission spectrum with albumin and when the dextran is added to the albumin with different concentration are shown in Fig.4.11 When the concentration of albumin is increases from 1 % to 2%, the refractive index changes by 0.00185 and spectrum shifts by 2.5 nm. The calculated bulk sensitivity,  $\Delta\lambda/\Delta n$  of albumin in buffer is 1351 nm/RIU. When dextran is added in albumin by 1 % and 2% the combined refractive index becomes 0.00205 and we obtain the resonant shift of 2.25 nm with sensitivity of 1097 nm/RIU. Inset of Fig 24 shows the change in Fano resonant peak with variation in A and A+D concentration with maximum shift of 3.3 nm for 2% concentration compare to 2.85 of albumin only. The slope of albumin dextran combination is higher than albumin in PBS. To detect biomolecules attached on the sensor surface, the layers of protein A (refractive index of 1.48) is uniformly functionalized on surface of device [74].

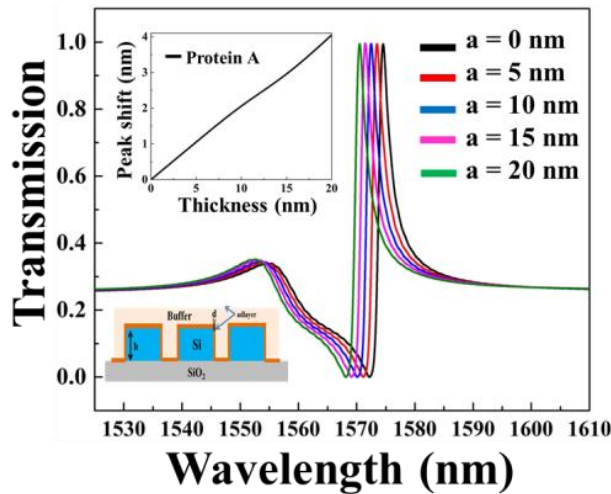


**Figure 4.12.** Transmission spectra with protein adlayer deposited on device and thickness is varied from 5 – 20 nm

Fig. 4.12 depicts the shift in Fano resonance peak with the variation in thickness of protein A layers. The thickness of Protein A layer increases in step of 5 nm upto 20 nm. In Fig. 3.25 resonant peaks are shown and we observe that peaks are distinguished and shifted by 1.05 nm with a change of 5 nm in protein A thickness which gives the surface sensitivity,  $\Delta\lambda/\Delta t$  of 0.21nm/nm. The radius of the silicon nano-disk influences the surface sensitivity of the device.

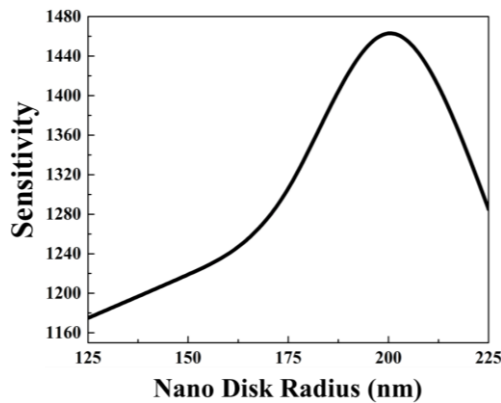


**Figure 4.13.** Effect of variation in nano-disk radius on the sensitivity. The grating period and grating width is kept at 500 nm and 150 nm.

The effect of variation of the nano-disk radius on sensitivity is shown in Fig.4.13. The grating width, slot width and period are kept at 150 nm, 75 nm and 500 nm respectively. The highest sensitivity of 1463

nm/RIU achieved at the nano-disk radius of 200 nm. It is observed that the wider nano-disk radius improves sensitivity. This is because large nano-disk radius increases the light-matter interaction in the slot and grating region by increasing the optical mode area. When nano-disk radius taken less than 150 nm and increases beyond 200 nm the Fano profile deteriorates and optical confinement becomes weak. The highest quality factor obtained is 516. High-quality factor prolongs the light-matter interaction and improves detection of limit. The potential of a biosensor can be illustrated by optical device sensitivity for change in cladding or environment.

#### **4.6 Summary**

A nanophotonic bio-sensor based on Fano resonance using the engineered structure of a slot waveguide is proposed. Label-free optical detection of biomarkers for some viral infections is reported numerically. Some experimental study on APTMS is performed and used for the simulation of device characteristics. The proposed device has a sensitivity of 1463 nm/RIU for refractive index change of 0.02. The surface morphology of APTMS as functionalized surface analyzed experimentally. The proposed device can detect the refractive index change of 0.0008 in serum which is small enough to detect viral infections e.g. Hepatitis B biomarkers with high sensitivity. The smaller footprint of Fano resonant nanostructures results in the reduction of fabrication cost. The calculated FOM is 471 with detection of limit is  $1.02 \times 10^{-3}$  RIU<sup>-1</sup> is achieved. Laser ablation focused ion-beam milling; electron-beam lithography is possible techniques to fabricate these high-aspect-ratio structures. Group index of 6.34 induce by proposed structure efficiently slows the light propagation and increases the light-matter interaction for surface sensing applications. The proposed design has high fabrication tolerance for the variations in grating width and nano-disk radius. The strong optical confinement in the low index region enhances the light-analyte interaction for efficient detection of virus biomarkers in serum.

Advancements in material preparation, synthesis and fabrication technologies have greatly facilitated the development of highly sensitive and efficient photonic biosensors with enhanced optical responses. The combination of nano-disk with a grating in engineered optical slot waveguide carries a great potential for biosensing applications especially in realizing efficient, smart and cost-effective detection of viral infections.

The Fano resonance-based slot waveguide structure gives better device performance compare to TiO<sub>2</sub> loaded grating structure slot waveguide. The sensitivity of former device is 1463 nm/RIU while later device has sensitivity of 1200 nm/RIU. The minimum change in refractive index is lower i.e 0.0008 in Fano based compare to 0.005 in grating loaded. The FWHM in Fano resonance is 1.6 nm which is also smaller than grating loaded design of 4 nm.

## **Chapter 5**

### **Double Slot Hybrid Plasmonic Waveguide for Biosensing**

To confine optical mode in horizontal as well as vertical slot regions, a double slot waveguide with a cover of gold is designed for polarization-independent biochemical sensing to achieve high bulk and surface sensitivity. The engineered structure is composed of the three silicon ribs forming two vertical slots optical confinement of TE mode and a top gold cover in the shape of microchannel forms horizontal slot region for confining TM plasmonic mode. The gold-clad prevents leakage of transverse magnetic mode in cladding and confines it near to silicon ribs which results in an increment of light-matter interaction. The bulk sensitivity in TM mode is increases by 1.5 times with gold cover. The proposed device exhibits better response with the higher change in effective refractive index for surface sensing to detect DNA hybridization, thickness variation of protein A and HBsAg antigen detection.

#### **5.1 Plasmonic - Photonic Slot Waveguide**

Slot optical waveguide has shown great potential which can confine the light in subwavelength dimensions in a low refractive index region [148]. The SPR based sensors used surface polarized polaritons (SPP) on metals to yield high sensitivity. Plasmonic waveguide sensors suffered from high propagation losses which limit the performance of the device that could be improved by integration of low loss photonic waveguides [38], [166]. This integration of plasmonic and photonic waveguides to enhance the sensing characteristics also known as hybrid plasmonic waveguides[84], [87]. Hybrid plasmonic devices support the combination of photonic and plasmonic modes with confinement in the subwavelength region and relatively low losses [86], [88]. The waveguide structure achieved polarization independence by supporting quasi-TE and quasi-TM mode which is confined in slot regions. High optical confinement in low index region

due to plasmonic enhancement and photonic high index contrast is a promising field to provide better performances for optical sensors. Altogether the hybrid waveguide so formed provides an effective way towards polarization independent bio-chemical sensing. The microchannel under the gold cover in the proposed photonic-plasmonic waveguide can flexibly accommodate a bio-sample providing an efficient way for polarization independent detection of bio-chemical samples. The potential of double slot gold-clad cover waveguide for bulk and surface sensing was analysed numerically to foresee the use of the proposed design in an integrated nanophotonic sensor such as a Mach-Zander interferometer (MZI). The proposed structure exhibits high bulk sensitivity, subwavelength confinement and low propagation loss compared to plasmonic waveguides.

Here, we propose a photonic-plasmonic waveguide based on double slot and gold cover structure for the polarization independent label-free bulk and surface sensing. The proposed device is composed of three silicon ribs forming the two vertical slot regions. The silicon slot structure covered with a gold layer creating a horizontal slot region between top of silicon ribs and a gold layer which enable confinement of surface plasmonic polariton (SPP) mode. The double slot region supports the guidance of quasi TE mode while the quasi-TM mode is guided under the top gold layer in form of SPP mode. Altogether the hybrid waveguide so formed provides an effective way forward towards polarization independent bio-chemical sensing. The microchannel under the gold cover in the proposed photonic-plasmonic waveguide can flexibly accommodate a bio-sample providing an efficient way for polarization independent detection of bio-chemical samples. These low index vertical and horizontal slot regions are filled with analyte solutions. The buffer and bio-molecules are usually water-based with refractive indices near to 1.33, hence for better sensing, the optical confinement in low indices are desirable. The TE and TM mode confined in vertical and horizontal low index slot regions. The potential of double slot gold-clad cover waveguide for bulk and surface sensing was analysed numerically to foresee the use of the proposed

design in an integrated nanophotonic sensor such as a Mach–Zander interferometer (MZI). For TE mode and TM mode bulk sensing, the area under the gold-clad is filled with PBS buffer as analyte. For surface sensing, the biomolecules of the target antigen attached to all the exposed area under the gold-clad region. Here to show surface sensing we simulate for DNA hybridization and HBsAg antigen detection. Protein A and ssDNA layers are used as bio receptor and antibody for Hepatitis B surface antigen (HBsAg) detection [28], [74]. HBsAg is the first serological marker that appears in serum during acute Hepatitis B infection [167]. The proposed structure exhibits high bulk sensitivity, subwavelength confinement and low propagation loss compared to plasmonic waveguides.

## 5.2 Engineered Horizontal and Vertical Slot Structure

The proposed biosensor is based on double slot optical waveguide structure on silicon on insulator substrate shown in Fig.1(a). The waveguide comprised of three parallel silicon ribs separated by low index region and gold-clad cover is created over double slot waveguide to form a microfluidic channel.

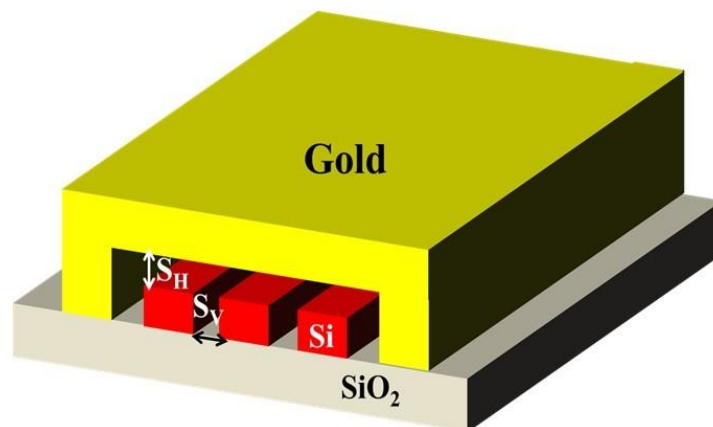


**Figure 5.1** Schematic of nanophotonic double slot waveguide structure with gold clad. The rib width, thickness and slot width of device is 300 nm, 220 nm and 100 nm. Thickness of gold clad is 200 nm.  $S_V$  and  $S_H$  are the vertical and horizontal slot widths.

The silicon ribs are 300 nm wide and placed at the gap of 100 nm low index region with the thickness equal to foundry standard of 220 nm.

The gold-clad width is optimized to 200 nm and the distance of gold-clad from silicon ribs is kept the same as the width of the slot between the silicon ribs. This gold cover acts as a microfluidic channel which holds the buffer solution over the device. The reflecting property of gold-clad cover helps in stronger optical mode confinement in the double slot region by prohibiting the light to leak in air. The optical mode confined in the device is the combination of photonic mode and plasmonic mode. In simulation area under the gold-clad filled with buffer or serum with target bioanalytes. The RI of silicon, SiO<sub>2</sub> and gold are taken as 3.47, 1.45 and 0.559 + j 9.81 for operation at a wavelength of 1550 nm.

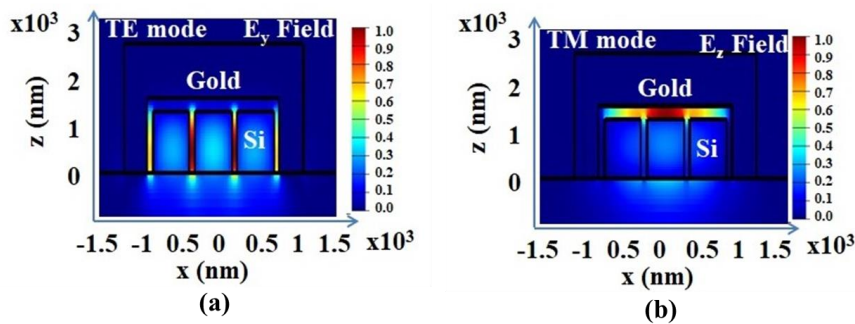


**Figure 5.2** (a) and (b) Optical confinement for  $E_y$  field of TE mode and  $E_z$  field of TM mode of proposed device.

We can observe the confinement of quasi-TE mode in vertical slot region formed between silicon ribs and quasi-TM mode in horizontal slot region formed between gold clad and the top of silicon ribs. Fig

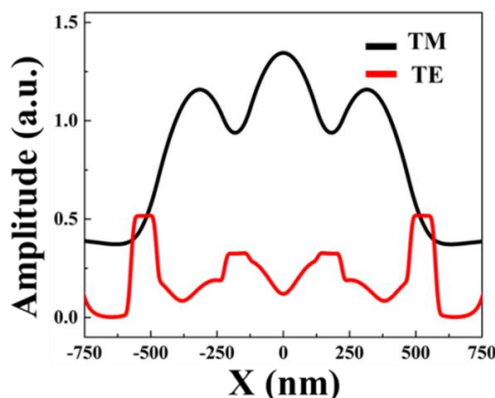


**Figure 5.3.** Electric field intensity in slot region for TE and TM mode.

5.2(a) and (b) shows the optical confinement of quasi-TE and quasi-TM mode in the vertical and horizontal slot regions of the proposed device. The dominant electric field component  $E_y$  get confines in vertical slot region for TE mode and electric field component  $E_z$  for TM mode gets confines in horizontal slot. The  $H_y$  field of TM mode has maximum intensity in dielectric but not in slot region so the  $E_z$  derived from  $H_y$  field shows discontinuity at the interface of silicon and gold providing maximum confinement intensity in horizontal slot region. The gold-clad cover prevents leakage of transverse magnetic mode in cladding and confines it near to silicon ribs which results in an increment of light-matter interaction in TM mode sensing. For the sufficient wider silicon ribs the mode confines in slot region and when the rib width decreases a portion of light also penetrate in dielectric thus reducing the interaction with cladding [66] . The electric field intensity for TE and TM mode are shown in Fig. 5.3. The TM mode shows higher intensity compare to TE mode because the gold-clad helps to confine more optical energy in the horizontal slot region. TE mode profile shows electric field intensity in vertical slot region between silicon ribs in between gold and silicon ribs. The photonic-plasmonic structure enhances the electric field intensity in the slot region compared to the photonic structure.

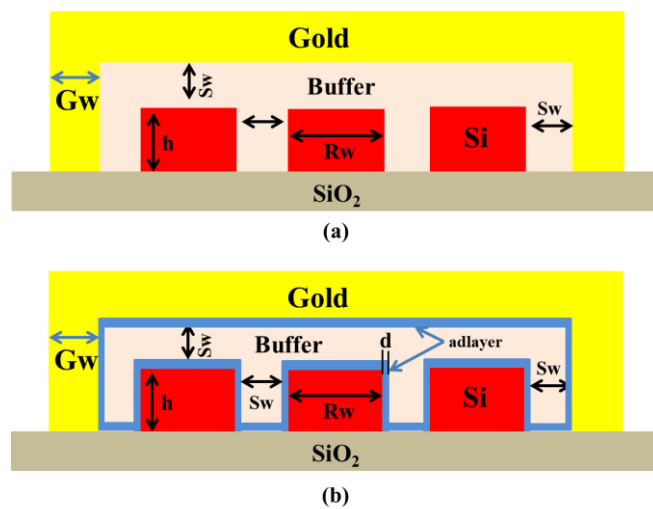
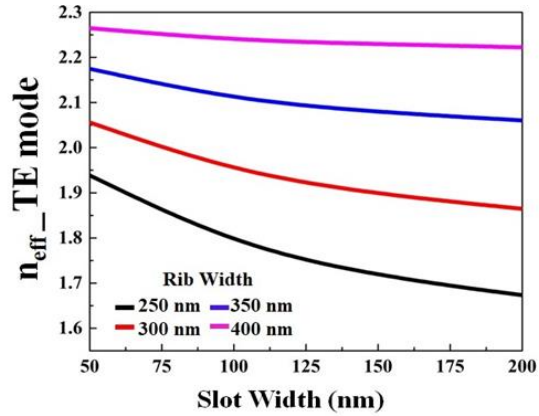


**Figure 5.4** (a) Cross-section of proposed device with gold clad and buffer solution.  $G_w$ ,  $R_w$  and  $S_w$  are the gold clad width, rib width and slot width (b) Cross-section of proposed device in buffer solution with adlayer integration

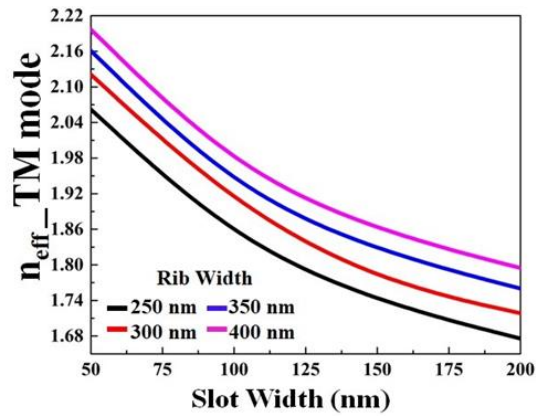
The proposed device is simulated for bulk sensing and surface sensing. For bulk sensing which involves the distribution of analyte over the top surface with maximum mode, confinement takes place in the cladding under the gold clad. In surface sensing, the optical waveguide modes interact with analytes which bound to the surface of sensor which cause a change in thickness. The thin adlayer is formed by absorption of molecules on all exposed area of the waveguide. The cross-section of the proposed device without adlayer and with adlayer on the silicon ribs and gold clad is shown in Fig. 5.4 (a) and (b). For 220 nm silicon thickness the slot width (Sw), rib width (Rw) and gold width (Gw) are optimized at 100 nm, 250 nm and 200 nm. The gap of gold-clad from silicon rib is equal to the width of slots created between the silicon ribs. We assume that adlayer is absorbed on all exposed area of double slot waveguide structure including inside part of the gold-clad region as shown in Fig 4(b). The thickness of adlayer varies from 1 nm to 10 nm with a refractive index of 1.48 which is same as protein A [74]. The area under the gold-clad is filled with buffer/analyte. Gold is used as metal cladding over double slot waveguide because it has good plasmonic property, less reactivity to organic matter and the gold surface is easily functionalize by thiol based compounds [168].

### **5.3 Modal Characteristics**

To obtain high sensitivity in the proposed device the optical field should be tightly confined in both vertical and horizontal slot regions. The photonic- plasmonic modes are investigated through the change in effective refractive index and propagation losses in the proposed device. The gold-clad over the double-slot silicon waveguide provides two-fold benefit, first to generate photonic plasmonic modes and second it prevents leaking of optical TM mode in cladding, thus increasing the optical field intensity in slot region. The effective refractive index of proposed device for TE and TM modes at different rib and slot width is shown in Fig.5.5. The rib width varies from 250 nm to 400 nm and the slot width varies from 50 nm to 200 nm. The thickness of the device is kept constant at 220 nm.



(a)



(b)

**Figure 5.5 (a) and (b)** Variation in effective refractive index with change in slot width for different rib width of double slot waveguide for TE and TM mode.

We can observe that as the rib width increases, the  $n_{\text{eff}}$  value grows for a fixed value of slot width. The larger  $n_{\text{eff}}$  with narrow slots shows that double slot waveguide with gold cladding provides higher optical confinement compared to conventional slot waveguide. As the slot width increases, the optical intensity of TE and TM mode reduces which results in a decrease in effective refractive index. The  $n_{\text{eff}}$  of the proposed device is higher for a wider rib because of the large refractive index of silicon and with smaller slots the mode confinement increases. The former effect due to the photonic modes and latter is due to plasmonic signal enhancement. Fig. 5.6 shows the propagation loss of the proposed device for TE and TM mode. The propagation loss is due to close vicinity of the metal layer hence, narrow the slot width more the propagation loss [86]. We observe at narrow slot width of 50 nm, the propagation loss is high due to high confinement of electric field

and it decreases with increase in slot width because the effective mode area in proposed device increases.

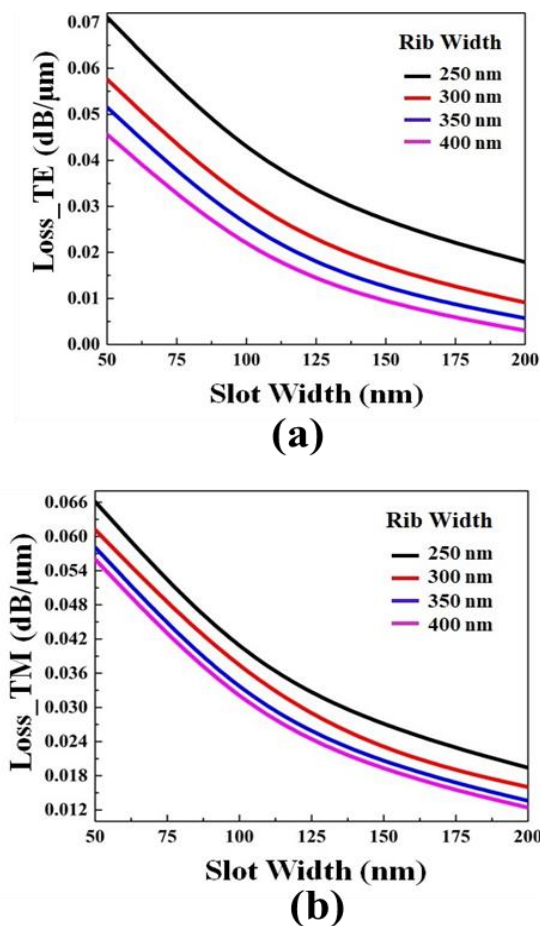


**Figure 5.6 (a) and (b)** Variation in propagation loss with change in slot width for different rib width for TE mode

From Fig. 5.6 we can conclude that propagation loss in the proposed device is more than convention slot waveguide but less than plasmonic waveguide. The propagation loss of the proposed device for 300 nm rib width and 100 nm slot width is 0.0292 dB/μm while for plasmonic waveguide the loss is 0.0495 dB/μm. It shows that loss in the proposed device is a combination of loss-less silicon photonics and lossy plasmonic modes. As the slot width increases the loss reduces due to low confinement. When the rib width increases the loss decreases it is because as the silicon area become larger the effective area of confined mode also become bigger and the effect of plasmonic mode reduces [84]. The highest loss of 0.082 dB/μm obtained for TE

mode at 50 nm slot width and 250 nm rib width. When the rib width is 400 nm the loss is 0.045 dB/ $\mu\text{m}$  for 50 nm slot width which decreases to 0.005 dB/ $\mu\text{m}$  for 200 nm slot width. The highest loss at TM mode for 250 nm rib at 50 nm slot is 0.077 dB/ $\mu\text{m}$  which reduces to 0.025 dB/ $\mu\text{m}$  for slot width of 200 nm. The device loss can be compensated by increasing the input power. The trade-off between loss and optical confinement of the proposed device can be depending on the type of applications.

#### 5.4 Bulk and Surface Sensing

The fundamental mode in silicon slot waveguide is quasi-TE where transverse electric field component is parallel to the substrate and quasi-TM mode where the transverse magnetic field component is parallel to the substrate [67]. In bulk or homogenous sensing, the refractive index of cladding varies which leads to change in the effective refractive index of guided modes. This change in the effective refractive index depends on optical confinement in slot waveguide, higher confinement means high bulk (homogenous) sensitivity [70]. The confinement factor in the slot region and the cladding medium (including the slot region) is defined as follows in Eq. (2.2)

The bulk (homogenous) sensitivity of silicon waveguide is calculated numerically by  $S_h = \partial n_{eff} / \partial n_m$ , where  $\partial n_{eff}$  is the change in effective refractive index and  $\partial n_m$  is the change in the refractive index of the medium (cladding) [169]. For surface sensing, it is assumed that all exposed areas of silicon waveguide under the gold-clad are covered with a thin layer of adsorbed molecules. The interaction between confined optical fields and varying thickness of the adsorbed layer changes the effective refractive index of the waveguide. Surface sensitivity of waveguide is calculated numerically by  $S_s = \partial n_{eff} / \partial t$ , where  $\partial n_{eff}$  is the change in effective refractive index and  $\partial t$  is the change in adlayer thickness [170]. Fig.5.7 shows the bulk sensitivity and surface sensitivity of silicon waveguide with an increasing number of slot regions. The single rib waveguide confines optical power inside waveguide whereas single and double slot waveguide concentrates

optical power in between ribs i.e slot region. In double slot waveguide, field confinement in the slot region is less than single slot waveguide, but the area of surface layer sensing is increases [171].

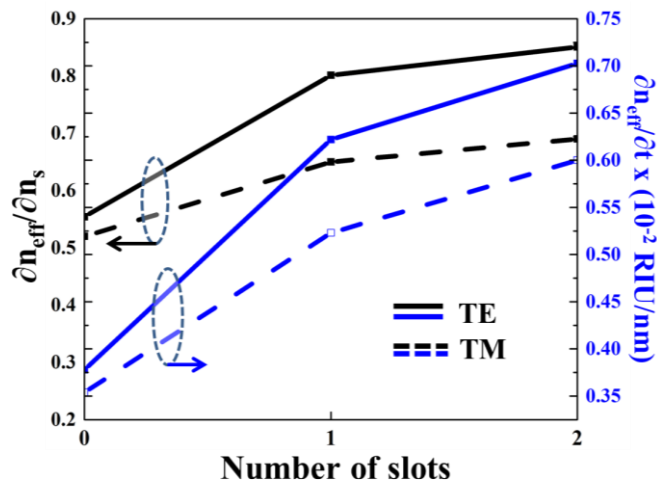
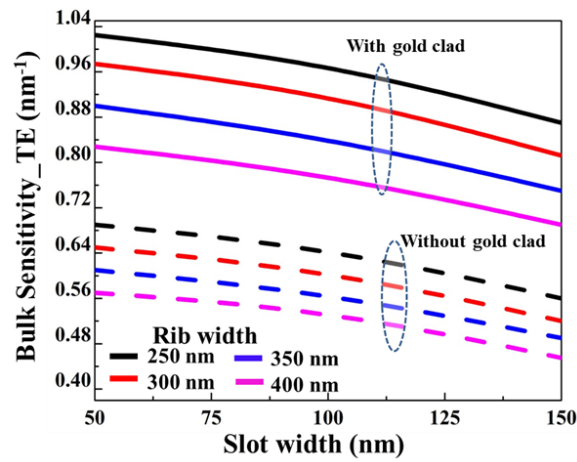
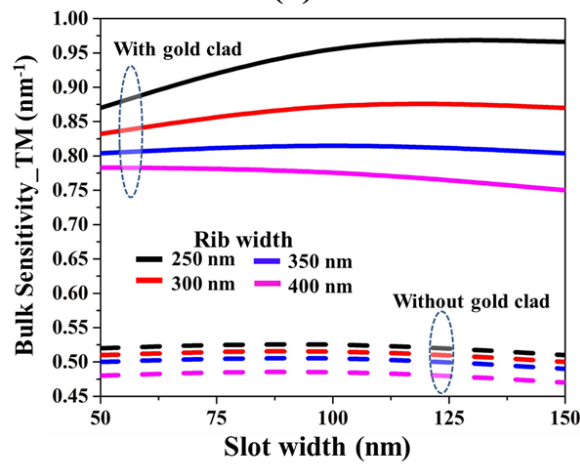


**Figure.5.7.** Bulk and Surface sensitivity for TE and TM modes as a function of number of slots.

As the slot regions in silicon waveguide are increases the bulk and surface sensitivity increase up to a point where mode start leaking from the waveguide. As shown in Fig. 5.8 (a) and (b) the bulk (homogenous) sensitivity of TE mode is higher than TM mode. The surface sensitivity is always low when compared to bulk sensitivity because when molecules bind to surface the optical property changes only in close proximity of the device surface [170]. To investigate the bulk sensitivity of double slot waveguide with gold and without gold clad, we set rib width of different values from 250 nm to 400 nm and increase the slot width from 50 nm to 150 nm by keeping thickness constant at 220 nm respectively. Fig. 4.8 shows bulk sensitivity of the proposed device for TE mode and TM mode with the change of 0.001 RIU in analyte refractive index. The solid lines in graph represent bulk sensitivity with gold-clad over double slot waveguide and dash lines shows sensitivity for without gold- clad. The bulk sensitivity of TE mode in the proposed device with gold-clad is higher when compared to without gold-clad device as shown in Fig.4.8. The increase in bulk sensitivity of TE mode with gold-clad is due to formation of photonic-plasmonic mode in vertical slot regions.



(a)



(b)

**Figure.5.8.** Bulk sensitivity for (a) TE mode and (b) TM mode with variation in rib width and for different slot widths.

The highest bulk sensitivity achieved in TE mode is  $1.034\text{nm}^{-1}$  for rib width of 250 nm which decreases to  $0.81\text{nm}^{-1}$  when rib width increases to 400 nm rib width for fixed slot width of 50 nm. The highest bulk sensitivity achieved without gold clad is  $0.68\text{nm}^{-1}$  for 250 nm rib width and 50 nm slot width. It is clear that hybrid plasmonic-photonic modes increase the light-matter interaction compare to only photonics or plasmonics modes. In Fig. 11 the bulk sensitivity in TM mode is higher due to the presence of gold-clad, which covered the device forming a horizontal slot on top of three silicon ribs. The bulk sensitivity in TM mode increases from  $0.54\text{ nm/nm}$  of without gold-clad to  $0.87\text{ nm/nm}$  with gold-clad for 50 nm slot width and 250 nm rib width. At 100 nm slot width, with gold clad, the highest bulk

sensitivity of TE mode is 0.97 nm/nm and for TM mode it is 0.95 nm/nm for the rib width of 250 nm. As the slot width increases the intensity of confined optical power reduces and bulk sensitivity decreases. Bulk sensitivity is higher for 250 nm rib width and decreases as rib width increases to 400 nm. This is because as the rib width increases most of the optical mode starts confining in high index silicon core region instead of low index slot regions. The limit of detection [82] in bulk sensitivity is  $1.98 \times 10^{-4}$  RIU. It is clear that gold clad on double slot waveguide increases the bulk sensitivity for TE and TM mode. A smaller slot width exhibits high sensitive performance with large change in effective index. Due to the limitation in fabrication process of creating 50 nm slot, a slot region of 100 nm width is the minimum value we can select for biosensing applications to accommodate bio-analytes.

For surface sensing PBS buffer is used as the medium, the top surface of the device under gold-clad assumes to be filled with PBS buffer which acts as cladding for optical confinement. The refractive index of PBS can be calculated by Sellmeier equation 4.1 [172]. The presence of adlayer on the silicon and gold affects the guided modes and waveguide can be used for surface sensing. To investigate the surface sensitivity of double slot waveguide, we set slot width of different values from 50 nm to 200 nm with a step size of 50 nm and check for rib width of 250 nm by keeping thickness constant at 220 nm respectively. In the simulation, the adlayer assumes to be homogenous, isotropic and uniformly deposited on all exposed regions of double slot waveguide [173].

The thickness of adlayer varies from 2 nm to 4 nm with a refractive index of 1.48 and medium is taken as PBS buffer solution with the refractive index of 1.336. Fig. 5.9 shows the effective refractive index difference ( $\Delta n_{\text{eff}}$ ) of TE and TM mode when the adlayer thickness varies from 2 nm to 4 nm for 250 nm rib width. We can observe that effective refractive index difference largely affected for TM mode due to the presence of gold-clad covering the double slot waveguide.

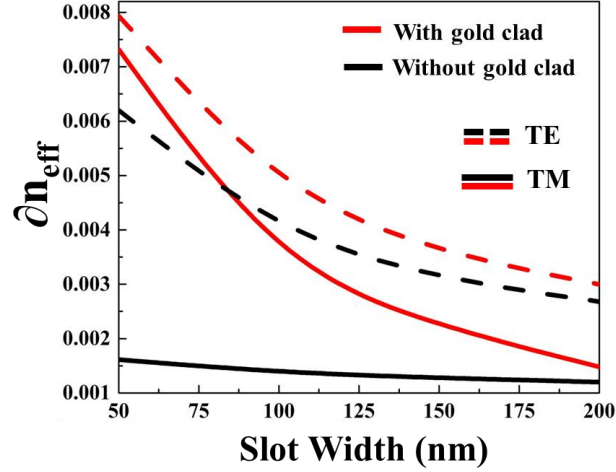


**Figure 5.9.** Variation of the effective refractive index difference when adlayer thickness changes from 2 nm to 4 nm for TE and TM mode. The rib width is kept at 250 nm and slot width varies from 50 nm to 200 nm.

The  $\partial n_{\text{eff}}$  for surface sensing with adlayer is calculated by:

$$\partial n_{\text{eff}} = n_{\text{eff}} \text{ 4 nm adlayer} - n_{\text{eff}} \text{ 2 nm adlayer.}$$

The effective refractive index difference,  $\partial n_{\text{eff}}$  of TE mode with gold clad is 0.00793 while for without gold-clad is 0.0063. The  $\partial n_{\text{eff}}$  for TM mode is .00731 with gold clad and 0.00161 for without gold clad device. Gold-clad increases the  $\partial n_{\text{eff}}$  of TM mode by 7 times than without gold-clad device. As we know that higher the  $\partial n_{\text{eff}}$  is higher the surface sensitivity of the proposed device. When the slot width increases from 50 nm to 200 nm for rib width of 250 nm, the intensity of confined optical power in TE and TM mode reduces and  $\partial n_{\text{eff}}$  starts decreasing. Due to higher optical confinement the effect on  $\partial n_{\text{eff}}$ , with gold clad, for TM mode is higher when compares to without gold clad when slot width varies from 50 nm to 200 nm. Double slot waveguide exhibits higher  $\partial n_{\text{eff}}$  because of large surface area compared to single slot waveguide.

The figure of merit [82] of the proposed device for bulk and surface sensing for the wavelength range of 1500 nm to 1600 nm is shown in Fig.5.10. FOM for bulk sensing is calculated for rib width of 250 nm, slot width of 50 nm and 1.337 as cladding medium index. For FOM of surface sensing, the adlayer thickness is kept at 1 nm with refractive index of 1.42, the refractive index of the medium is kept at 1.337. The highest FOM (surface) is 0.137/nm and for FOM (bulk) is 335/RIU.

FOM (surface) increases with wavelength up to 1550 nm and falls for further increase in wavelength while FOM (bulk) become near to constant after 1550 nm.

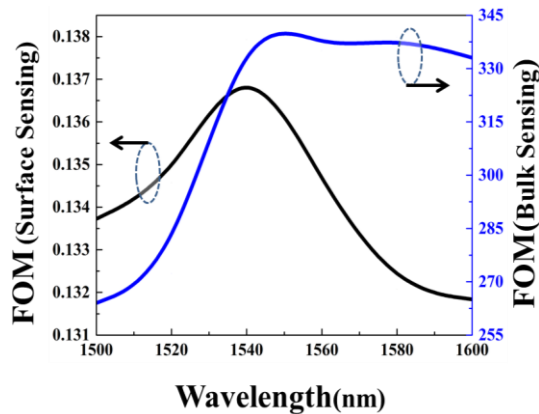


**Figure 5.10.** Figure of merit for bulk and surface sensing of proposed device for a wavelength range of 1500 nm to 1600 nm.

The performance of the proposed sensor can be improved by introducing the nano grating inside microchannel on the top of silicon ribs.

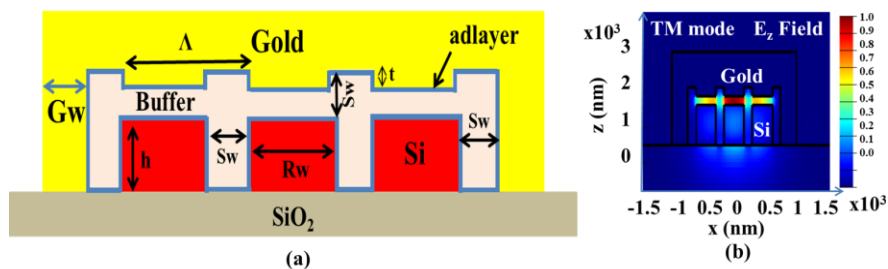


**Figure 5.11.** (a) Schematic of nanophotonic double slot waveguide structure with grating in gold clad. (b) Optical confinement of TM mode for  $E_z$  field.

The cross-section of the proposed device with adlayer on the silicon ribs and grated gold clad is shown in Fig. 5.11 (a). For 220 nm silicon thickness the slot width ( $S_w$  and  $S_H$ ), rib width ( $R_w$ ), grating thickness ( $t$ ) and gold width ( $G_w$ ) are optimized at 100 nm, 250 nm, 70 nm and 200 nm. The gold-clad spacing from silicon rib is equal to the width of the slots created between the silicon ribs i.e. the width of horizontal and vertical slots are same. The grating is formed in gold in the horizontal slot region with a period of 350 nm (duty cycle = 71%) and thickness of 60 nm. The horizontal slot width changes with the

variation in the gold grating thickness in the slot region. Fig.5.11(b) shows the optical confinement of TM mode in the proposed device. The optical mode confined in the device is the combination of photonic mode and plasmonic mode.

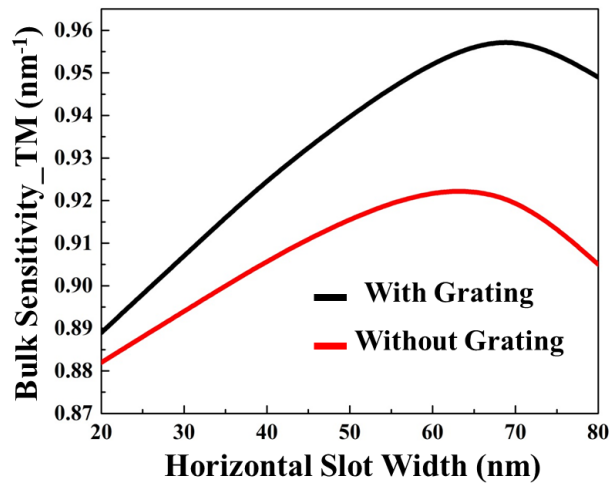


**Figure 5.12.** Bulk sensitivity in TM mode with grating and without grating for the variation of horizontal slot width.

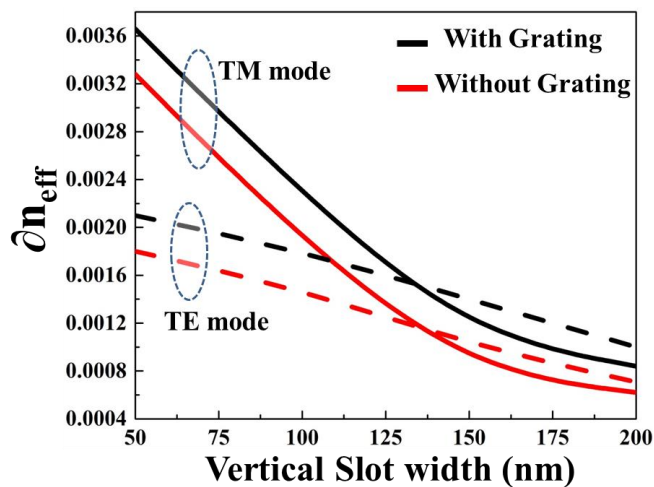


**Figure 5.13.** Variation in difference in  $n_{eff}$  of device with grating and without grating for change in vertical slot width.

The bulk sensitivity in TM mode is observed for grating and for without grating is shown in Fig. 5.12, where horizontal slot width varies from 20 nm to 80 nm with change in gold grating thickness. The highest sensitivity of 0.96 nm/nm is obtained for the grating thickness of 70 nm. The grated gold-clad over the double-slot silicon waveguide

provides two-fold benefit, first to generate photonic plasmonic modes and second it prevents leaking of optical TM mode in cladding, thus increasing the optical field intensity in slot region. The difference in effective refractive index of device with grating and without grating is shown in Fig.5.13. The  $\partial n_{\text{eff}}$  of TM mode is larger because at smaller slot width (gold is in proximity with silicon) the mode confinement is higher and the effective refractive index increases.

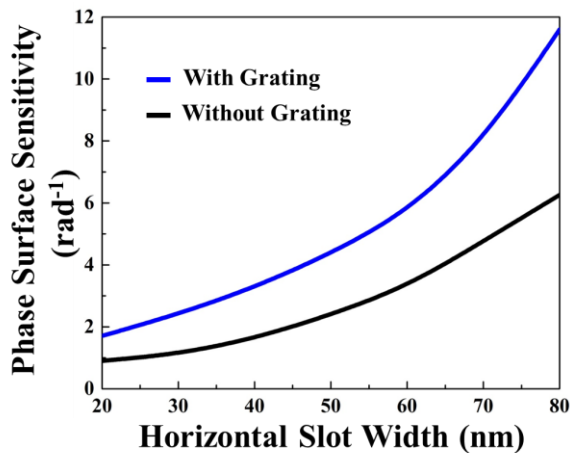


Figure 5.14. Variation in phase surface sensitivity of Protein A adlayer with change in horizontal slot width.

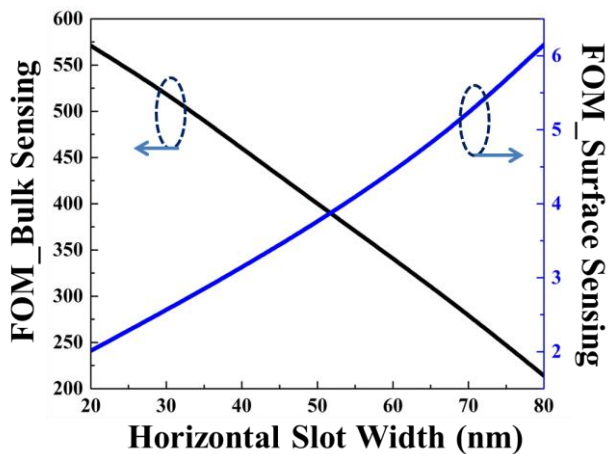


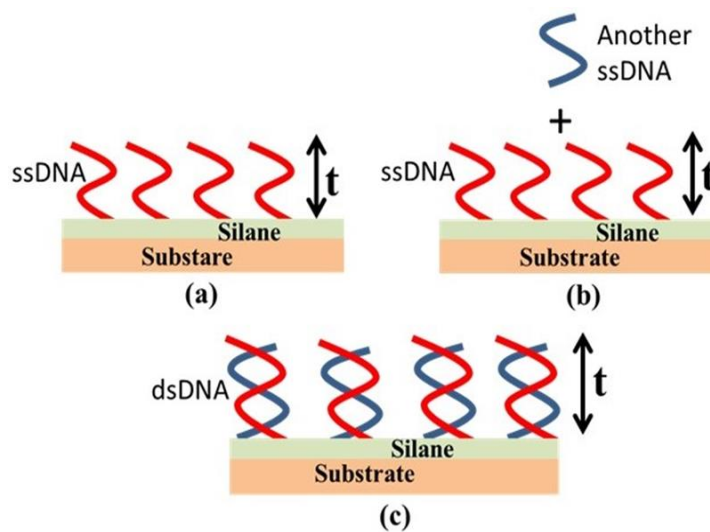
Figure 5.15. FOM for bulk sensing and surface sensing in TM mode.

Fig.5.14 shows the phase surface sensitivity of protein A (refractive index = 1.48) for variation in horizontal slot width. The phase surface sensitivity is calculated by MZI interferometer configuration. The

highest phase surface sensitivity with gold grating is 11.2/rad for 2 nm of adlayer compare to 6.3/rad without gold grating with respect to the buffer solution. When horizontal slot width decreases due to the increase in the thickness of gold grating ( $t$ ) the confinement in slot region also increases which in turn increases the phase surface sensitivity. The figure of merit (FOM) of the proposed device for bulk and surface sensing for TM mode with variation in horizontal slot width from 20 nm to 80 nm is shown in Fig.5.15. The FOM of surface and bulk sensing in TM mode is obtained with adlayer thickness difference of 2 nm and difference in bulk analyte index of 0.001. The highest FOM (surface) is 6.1/nm and for FOM (bulk) is 571/RIU. The proposed device exhibits better response with the higher change in effective refractive index for surface sensing applications.

### 5.5 DNA Hybridization and Detection of Viral Infection

We investigate the surface sensing application of the proposed double slot gold-clad device for detection of DNA hybridization [174]. The process of combining two single-strand DNA to form one double-strand DNA is called DNA hybridization. The proposed sensor is designed to detect the change in the effective refractive index of the surface layer when two DNA are combined [175].



**Figure 5.16.** (a-c) DNA hybridization processes. The film thickness ( $t$ ) is fixed.

The ssDNA attached to the silicon surface by the help of thin silane layer as shown in Fig. 5.16 (a). This silane acts as a functionalised layer for ssDNA. When the single-strand DNA layer, with the refractive index of 1.41 is attached to the 1 nm thick silane layer it acts as a receptor for another single-strand DNA layer as shown in Fig. 5.16 (b). When another ssDNA layer deposited it gets combined with first ssDNA layer to form a double-strand DNA layer as shown in Fig. 5.16 (c). In the DNA hybridization process, the thickness ( $t$ ) of ssDNA does not changes only the refractive index of film changes. The ssDNA refractive index is 1.456 and after hybridization, it changes to 1.53 while thickness of layer remains the same [176]. Fig.5.17 shows the effective refractive index difference between ssDNA and dsDNA for TE and TM mode. The slot width varies from 50 nm to 200 nm for rib width of 250nm and 300 nm. As the refractive index of dsDNA is higher than ssDNA the effective refractive index of the surface layer is also higher for dsDNA compare to ssDNA.

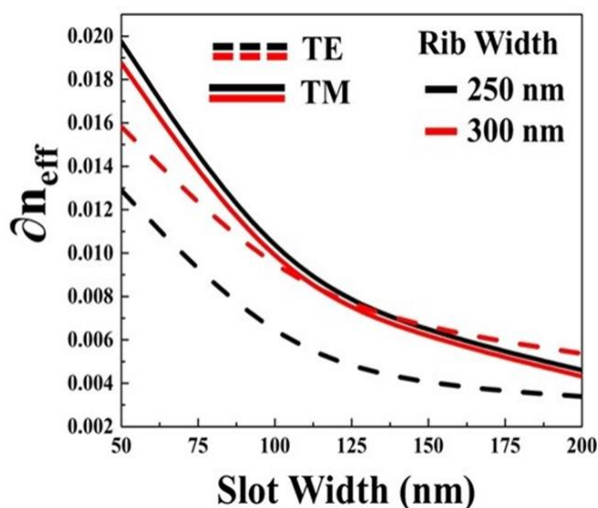


**Figure 5.17.** Variation in effective refractive index difference in DNA hybridization for rib width of 250 nm and 300 nm with change in slot width. The rib thickness is kept at 220 nm.

With increase in slot width the effective refractive index decreases because the confinement intensity of optical mode reduces in slot areas. For TM mode, the difference in  $n_{\text{eff}}$  for two different rib width is

very small as the change in surface area of top of silicon rib is very small for surface sensing application. The difference in  $n_{\text{eff}}$  for TE mode is higher because more surface area is available in the vertical slots which increases the surface sensitivity. As the width is optimized at 300 nm the TE mode efficiently confined in vertical slot region increases the  $n_{\text{eff}}$  difference between ssDNA and dsDNA.

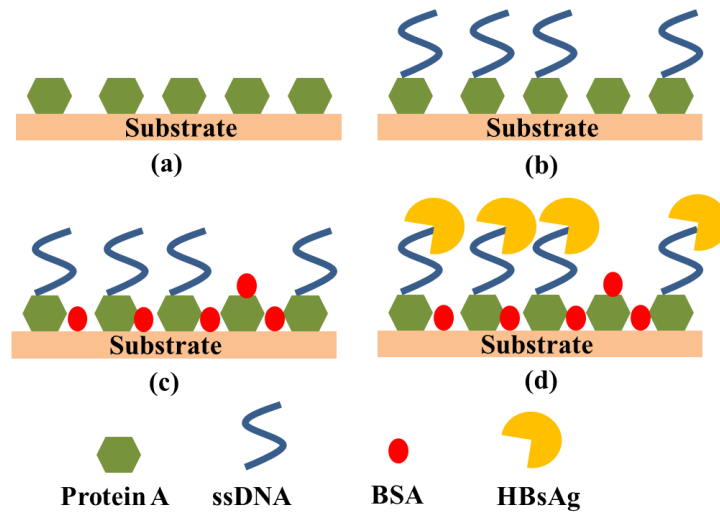


**Figure.5.18.** Functionalization of Protein A, ssDNA, BSA and HBsAg antigen on substrate

The surface sensing is performed numerically for the detection of HBsAg [158]. For surface sensing functionalization layer, antibody layer, blocking layer and targeted bio-analyte layer are formed over the proposed device with different thickness and different refractive indices as shown in Fig. 5.18. The first layer formed is Protein A, to functionalize the antibody, with a thickness of 2 nm and a refractive index of 1.48 in Fig. 5.18 (a). The second layer is formed of ssDNA as antibody to capture HBsAg antigen [177] with thickness and refractive index of 3 nm and 1.456 as in Fig. 5.18 (b). The third layer of BSA with a thickness of 1 nm and refractive index of 1.59 formed over Protein A as a blocking layer to stop unspecific binding over antibody as in Fig. 5.18 (c). The fourth and final layer of HBsAg antigen is formed, which binds to ssDNA, in Fig.5.18 (d), with a thickness of 4 nm and a refractive index of 1.5 [178]. PBS is taken as a buffer

solution for all layers with a refractive index of 1.335. The effective refractive index changes as the layers are formed over the device.

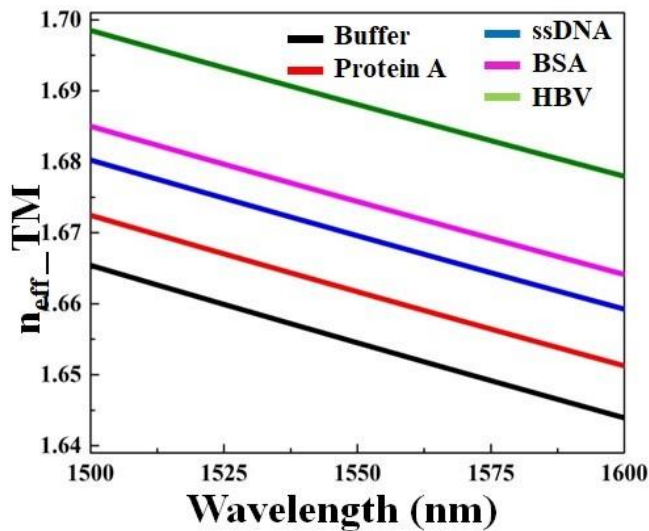


**Figure 5.19.** Variation in effective refractive index of proposed device for Protein A, ssDNA, BSA and HBsAg

The  $n_{\text{eff}}$  of each layer is calculated in TM mode for the wavelength range of 1500 nm to 1600 nm as shown in Fig. 5.19. The baseline of surface sensing is set by PBS buffer solution and effective refractive index of TM mode is calculated. We assume that functionalization layer of Protein A is deposited over the entire exposed surface of the device and the resultant  $n_{\text{eff}}$  varies by 0.00720 compared to PBS buffer solution. When ssDNA antibody deposited over protein A layer the  $n_{\text{eff}}$  varies by 0.00789. After deposition of BSA as a blocking layer, the  $n_{\text{eff}}$  of the device varies by 0.00482. We assume that after deposition of each layer the sample is washed by buffer solution to remove residue material and cladding is filled by PBS buffer solution. So every time the simulation is performed with buffer as the medium. The HBsAg antigen is attached to ssDNA antibody in the buffer solution and  $n_{\text{eff}}$  varies by 0.01368. The phase surface sensitivity is calculated by MZI interferometer. The phase surface sensitivity of the proposed device for HBsAg detection is calculated by [81] :

$$\frac{\partial \phi_D}{\partial a} = \frac{2\pi L}{\lambda} \frac{\partial n_{\text{eff},s}}{\partial a} \quad (5.1)$$

where  $L$  is the length of the device,  $\lambda$  is the operating wavelength and  $\partial n_{eff}$ ,  $s$  is the effective refractive index difference for surface layers.

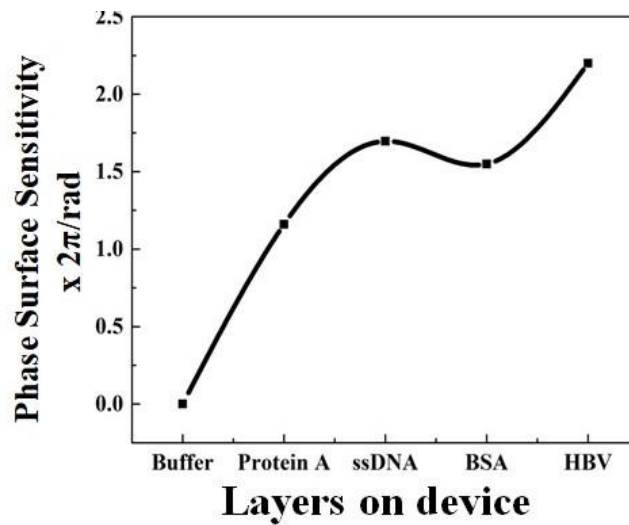


*Figure 5.20. Phase surface sensitivity with all layers for HBsAg detection.*

The length for MZI arm for phase surface sensing is taken at 1mm. The Fig. 5.20 shows the phase surface sensitivity for protein A, ssDNA, BSA and HBsAg antigen. The highest phase surface sensitivity of  $2.20 \times 2\pi/\text{rad}$  obtained for HBsAg (HBV) layer with respect to the buffer solution. When ssDNA deposited over protein A the surface phase sensitivity falls to  $1.696 \times 2\pi/\text{rad}$ . At BSA it increases to  $1.55 \times 2\pi/\text{rad}$  and when 4 nm of HBsAg is deposited the phase surface sensitivity changes to  $2.20 \times 2\pi/\text{rad}$ . The antibody-antigen combination of ssDNA and HBsAg gives the difference of  $1.98 \times 2\pi/\text{rad}$ . The surface mass density [82] of Protein A, ssDNA and HBsAg is calculated by  $m = a(n_a - n_m)/(dn/dc)$ , where  $dn/dc$  is the refractive index increment in  $\text{cm}^3/\text{g}$ . For protein A, ssDNA and HBsAg the  $dn/dc$  is  $0.186 \text{ cm}^3/\text{g}$ ,  $0.166 \text{ cm}^3/\text{g}$  and  $0.161 \text{ cm}^3/\text{g}$  respectively. The surface density of protein A, ssDNA and HBsAg adlayer are  $0.774 \text{ g}/\text{cm}^3$ ,  $2.168 \text{ g}/\text{cm}^3$  and  $0.103 \text{ g}/\text{cm}^3$  respectively. ssDNA formed thick layer to capture HBsAg antigen with low concentration.

## 5.6 Summary

We propose an engineered nanophotonic waveguide by combining a double vertical slot and a horizontal slot under a gold cover which

enable the guidance of photonic quasi-TE mode and plasmonic quasi-TM mode. The gold-clad cover increases the bulk sensitivity in TM mode by 1.5 times compared to only photonic device. The propagation loss observed is lower than plasmonic waveguide and higher than silicon photonics. Bulk sensitivity for TE and TM mode is  $1.024 \text{ nm}^{-1}$  and  $0.95 \text{ nm}^{-1}$  is better than silicon photonics devices. The device offers low loss of  $0.005 \text{ dB}/\mu\text{m}$  for TE mode and  $0.012 \text{ dB}/\mu\text{m}$  for TM mode at  $400 \text{ nm}$  rib width. The proposed device exhibits better response with the higher change in effective refractive index for surface sensing to detect DNA hybridization and thickness variation of protein A. The phase surface sensitivity of functionalization layer, antibody and HBsAg antigen is  $1.16 \times 2\pi/\text{rad}$ ,  $1.69 \times 2\pi/\text{rad}$  and  $2.20 \times 2\pi/\text{rad}$ . The bulk sensitivity with grating structure in TM is  $0.96 \text{ nm}/\text{nm}$  and phase surface sensitivity of Protein A functionalization layer is  $11.6 /\text{rad}$ . The strong optical confinement in subwavelength dimensions so obtained in the proposed waveguide can be utilized to make compact devices for polarization independent sensing of biochemical analytes.

## Chapter 6

### Label-Free Nanocomposite Film Biosensor for E. coli Detection

Food borne bacterial illnesses give rise to a threat to human health across the globe. Early detection of E. coli with high sensitivity is crucial to preventing the disease. We demonstrate a rapid and label-free detection mechanism of bacteria E. coli utilizing the photocurrent biosensing platform. The proposed biosensor is based on the interaction of E. coli with the functionalized surface of copper doped ZnO/TiO<sub>2</sub> (CZT), which is prepared by the sol-gel technique. CZT deposited by spin coating method on ITO coated glass. The photo-excited carriers which provide photocurrent on the application of a voltage on ITO/CZT nanocomposite thin films are utilized to detect E. coli in buffer solution. Proposed ITO/CZT thin film exhibits photocurrent for a linear range of 10<sup>3</sup> CFU/ml to 10<sup>5</sup> CFU/ml with a lower detection limit of 1000 CFU/ml. The highest photocurrent exhibit by ITO/CZT film is 239  $\mu$ A after functionalization reduces to 218  $\mu$ A and changes to 206  $\mu$ A in presence of drop cast E. coli in the buffer. A change of 20  $\mu$ A is detected with a change in concentration of E. coli on the application of 4volts. This method of detection provides flexibility with optical and electrochemical characteristics opening a whole new class of integrated photonic devices for multidisciplinary applications.

#### 6.1 Nanocomposite for Pathogen Detection

Detection of pathogenic strains is necessary for the food industry and water supplies because the microbial infection morality rate is very high. Many bacterial pathogens in food are responsible for foodborne diseases that are hazardous to human health [5], [179]. E. coli is one of the food bacteria transmitted in the human body through consumption of non-hygienic food, milk and water. Infection with E. coli bacteria produces a toxin that causes many diseases to humans like diarrhoea, nausea, vomiting and meningitis [180]. Conventional methods of detection of food borne bacteria are ELISA, culture-based, ATP

bioluminescence, flow cytometry and PCR [181], [182]. To perform detection from these methods, follow certain steps like enrichment, serological verification, plating, and biochemical screening [4], [183]. These methods suffer from complexity, time-consuming, required specific facilities, produce biological waste and are tedious [184], [185]. So early and rapid detection of bacterial pathogens are required with high sensitivity to identify disease in starting stage.

New advancements in biosensors carry the potential in early detection of food pathogenic bacteria with their fast and low-cost methods. Various techniques are developed for detection of bacterial pathogen by piezoelectric quartz crystal [15], electrochemical [186], [187] and optical methods [188], [189]. Label-free methods of electro-optical detection for pathogens and bio-chemicals leads to monitor interactions between chemical and biological analytes, provide results in real-time and detect analytes without using labels. New fabrication technologies in nanomaterials facilitate the growth of smaller, low cost, adaptable and fully integrated biosensors to determine bacterial pathogens [190], [191]. Biosensors based on nanomaterials demand binding of biomolecules with target analytes and generate a detectable response in terms of impedance or current [192]–[194]. This fast response enables rapid detection of bacterial pathogens and ensures the safety of public health. In pristine semiconductor oxides, the recombination rate of photo generated charge carriers is very high which restricts the flow of current. To improve photocurrent for a certain application, doping of metal and semiconductor oxides are done to vanquish the recombination of charge carriers [13], [195]. By controlling the morphology of the semiconductor surfaces the recombination of photo generated charge carriers can be reduced and the active area of reaction increases. Metal oxides are stable in nature when they are derived in presence of oxygen. These oxides show strong absorption in UV-Visible region and higher electron transfer rate, large surface areas and easy separation of charge carriers [54], [196]. It supports immobilization of biomolecules on the surface to

facilitate the transfer of charge resulting in enhancement of biosensing property.

Metal oxides of Zinc, titanium, tin and iron exhibits excellent properties of catalysis, morphological function and bio-compatibility [197].  $\text{TiO}_2$  and  $\text{ZnO}$  show efficient catalytic properties and high photochemical stability, with a bandgap of 3.3 eV and 3.2 eV, respectively[198]. Wide band gap, low response in the visible region and fast recombination of photo generated charge carriers are limitations of  $\text{TiO}_2$ , which results in the poor photocatalytic property. To overcome this constraint efforts are done to reduce the recombination of charge carriers by modifying  $\text{TiO}_2$  into hybrid material. Metal nanocomposites (cations or anions) and semiconductor oxides are incorporate with  $\text{TiO}_2$  to increase interfacial charge transfer [199]. Copper oxide[200] and Zinc oxide [36] are the effective materials that improve the photocatalytic property of  $\text{TiO}_2$ . Many efforts are done to combine semiconductor oxides with suitable material to enhance the photocatalytic property. In [201] they report  $\text{AuNR@TiO}_2$  core-shell structure enhances the electron transfer to  $\text{TiO}_2$  and shows good stability and biocompatibility. Fernando et.al [202]shows doping of Au particles in  $\text{ZnO}$  improves the photocathode response under visible light. Modification of  $\text{TiO}_2$  with  $\text{ZnO}$  and copper improves the properties of  $\text{TiO}_2$  and make an effective photo catalyst due to enhance electron mobility. Integration of Copper and  $\text{ZnO}$  with  $\text{TiO}_2$  leads to more sensitive biosensors where copper doped  $\text{ZnO/ TiO}_2$  offers rapid transfer of electrons across active sites of the functionalized surface.

In this work, we present a photocurrent bio-sensing mechanism for label-free detection of *E. coli* pathogen using copper doped  $\text{ZnO/TiO}_2$  (CZT) nanocomposite thin film over ITO coated glass substrate. Nanocomposite CZT deposited over ITO coated glass derived from the sol-gel process. Under the irradiation of light source nanocomposite, CZT which is deposited over ITO glass generates photocurrent with the application of voltage. The proposed biosensing mechanism is based on a change in photo-current to detect the presence of *E. coli* in

buffer solution. APTMS as bio receptor for E. coli bound covalently on the CZT surface. The interaction of the functionalized surface with E. coli was confirmed using the photoluminescence spectrum. Morphology of spin-coated CZT over ITO coated glass and functionalized CZT are observed by SEM. The proposed nanocomposite thin film shows variation in photocurrent for different E.coli concentrations varying from  $10^5$  CFU/ml to  $10^3$  CFU/ml with buffer as the surrounding medium. To verify the function of CZT/ITO thin film as a biosensor only E. coli is used. The results obtained for E. coli detection carry the potential for the proposed film sensor to be used as a label-free biosensing platform for other food pathogens.

## 6.2 Thin Film Preparation, Bacteria Culture and Functionalization

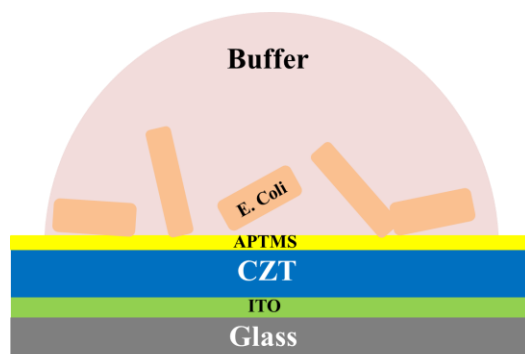


*Figure 6.1. Schematic of prepared ITO/CZT film biosensor with functionalization of APTMS*

The proposed biosensor shown in Fig.6.1 is based on the interaction of E. coli with the functionalized surface of copper doped ZnO/TiO<sub>2</sub> (CZT), which is prepared by the sol-gel technique. CZT deposited by spin coating method on ITO coated glass. The photo-excited carriers which provide photocurrent on the application of a voltage on ITO/CZT nanocomposite thin films is utilized to detect E. coli in buffer solution. Proposed ITO/CZT thin film exhibits photocurrent for a linear range of  $10^3$  CFU/ml to  $10^5$  CFU/ml with a lower detection limit of 1000 CFU/ml. The highest photocurrent exhibit by ITO/CZT

film is 239  $\mu\text{A}$  after functionalization reduces to 218  $\mu\text{A}$  and changes to 206  $\mu\text{A}$  in presence of drop cast E. coli in the buffer. A change of 20  $\mu\text{A}$  is detected with a change in concentration of E. coli on the application of 4volts. This method of detection provides flexibility with optical and electrochemical characteristics opening a whole new class of integrated photonic devices for multidisciplinary applications.

To prepare the copper doped ZnO/TiO<sub>2</sub> nanocomposite following materials used : Titanium(IV) n-butoxide (Ti(O-nBu)<sub>4</sub>, M.W.= 344.35 g/mol), Ethanol C<sub>2</sub>H<sub>5</sub>OH, M.W.= 46.07 g/mol), Acetylacetone (CH<sub>3</sub>COCH<sub>2</sub>COCH<sub>3</sub>, MW=100.13 g/mol), Zinc acetate dihydrate (Zn(CH<sub>3</sub>COO)<sub>2</sub>.2H<sub>2</sub>O, M.W. =183.48 g/mol), Diethanolamine (HN(CH<sub>2</sub>CH<sub>2</sub>OH)<sub>2</sub>, MW=105.14g/mol), Cupric chloride (CuCl<sub>2</sub>, MW 134.45 g/mol). All chemicals used were of analytical grade. All solutions were prepared with ultra-pure water (18.2M $\Omega$  cm<sup>-1</sup>).

CZT nanocomposite is prepared by the sol-gel process. The first solution is prepared by mixing 20 ml of 2-methoxyethanol in 3.5 ml of Titanium (IV) n-butoxide with 1.3 ml of acetylacetone. The mixture is stirred vigorously for 30 min at room temperature. Acetylacetone is added as a chelating agent to decrease the reactivity of Titanium (IV) n-butoxide. Acetic acid is added to the solution after 30 min. Glacial acid is used for hydrolysis via an esterification reaction. A molar ratio between acetic acid and Titanium (IV) n-butoxide of 0.2 was utilized. For the second solution zinc acetate dihydrate (2.2 gm), 2-methoxyethanol (20 ml) and 1.2 ml of diethanolamine (DEA) are mixed to form a second precursor solution. The mixture was stirred at 50°C for 90 minutes to produce a clear homogeneous solution. Copper doped ZnO/TiO<sub>2</sub> (CZT) sol was prepared by mixing TiO<sub>2</sub> sol and ZnO sol in a 1:1 molar ratio. The solution was stirred for 30 min at 500 rpm, afterwards, cupric chloride is added to the solution. The final solution was aged for 48 hours to obtain the gel solution. Two types of solutions are formed ZnO/TiO<sub>2</sub> and copper doped ZnO/TiO<sub>2</sub>.

Bacteria strain DH5 $\alpha$  is incubated in Luria Bertani Broth culture medium which is composed of Tryptone 10 g/L, yeast extract 5 g/L and NaCl 10 g/L. E. coli bacteria strain was cultured in LB nutrient

medium at 37 °C for 24 hrs. at the vibration of 125 rpm. The bacterial cells are separated by centrifugation after incubation and three times washed by phosphate buffer saline solution. Bacteria cell concentration suspension was stored at 4 °C. Functionalization of APTMS over ITO/CZT matrix surface provides amino groups. Surface functionalization was performed by putting ITO/CZT coated sample in (3-aminopropyl) triethoxysilane (APTMS): Ethanol (2:1000) solutions for 30 min. After the sample is washed three times by ethanol and methanol and dried in oven for 15 min at 80°C.

### **6.3 Film Morphological Characteristics**

The absorbance spectrum of nanocomposites Cu- ZnO/TiO<sub>2</sub> (CZT) and E. coli concentration were measured by a UV-visible spectrophotometer (Perkin Elmer UV 750). Photoluminescence (PL) spectra of ITO, ITO/CZT film and after functionalization were measured at room temperature using a photoluminescence analyzer (Dongwoo Optron DM 500i, pulsed Xe lamp) with an excitation wavelength of 325 nm. The morphology of the CZT film and functionalized samples were characterized using a SUPRA 55 field emission scanning electron microscope (SEM). Ellipsometry of thin films was performed on JA Woolam Ellipsometer for the wavelength range of 200 nm to 1000 nm. The current-voltage (I–V) curve was measured by using the Keithley Source meter. A 500W Xe lamp visible light source of wavelength 200 nm to 700nm was used as the irradiation source.

The UV spectroscopy was performed on the freshly cultured E. Coli bacteria in the buffer. The absorbance spectra of E. coli in the wavelength range of 200- 700 nm is shown in Fig.6.2. The optical density at 600 nm is 0.055 for the cell concentration to be 10<sup>5</sup> CFU/ml. The absorbance of sol-gel derived CZT thin film over glass substrate examined by UV-VIS spectrometer in the wavelength range of 200–600 nm at room temperature. The absorbance spectra of nanocomposites thin films TiO<sub>2</sub>/ZnO, and Cu-ZnO/TiO<sub>2</sub> for copper

doping of wt % = 0.01 and 0.02) were examined in the wavelength range of 250–700 nm in room temperature shown in Fig.6.3.

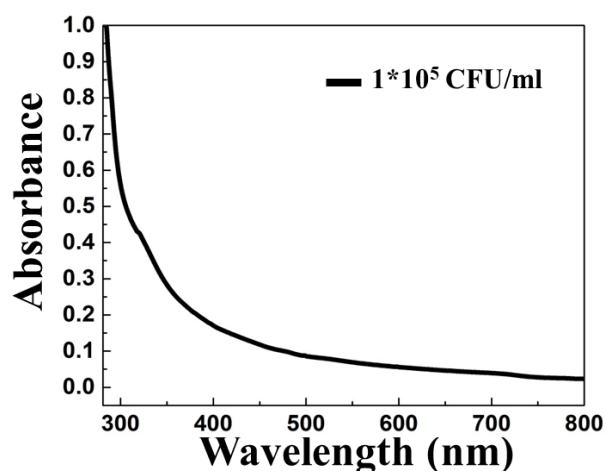


**Figure 6.2.** UV-Visible absorbance spectra of DHα *E. coli* bacterial cells for  $10^5$  CFU/ml concentrations.

It shows that absorption edges are formed at a wavelength near 350–550 nm for all samples. We can observe a shift in the absorption edge with doping of copper in ZnO/TiO<sub>2</sub> nanocomposite. The Fermi level of copper doped ZnO/TiO<sub>2</sub> nanocomposites vary due to the shift in absorption spectra, which leads to the reduction in the energy bandgap. CZT thin film exhibits high transmission of > 60% in UV to visible region shows the absorption edge around 300 nm.

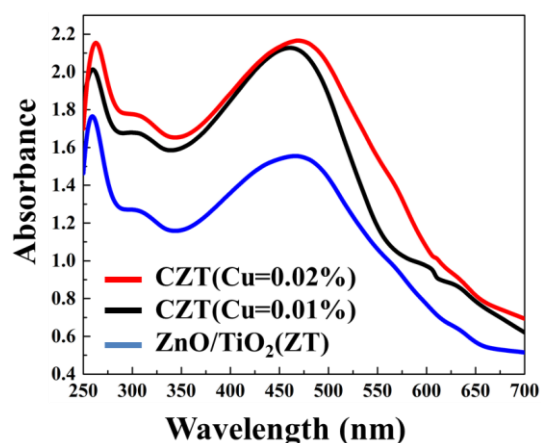


**Figure 6.3.** Absorbance spectra of sol gel derived nanocomposite CZT. Inset shows transmittance of spin coated Cu-ZnO/TiO<sub>2</sub> (CZT) film on quartz substrate annealed at 500°C

We can observe maximum absorbance in the UV region around 250 nm. The volume of *E. coli* concentration for a sample is kept at 50  $\mu$ l

in every measurement. Photoluminescence spectra of ITO, Cu-ZnO/TiO<sub>2</sub> and the functionalized surface of CZT/ITO on quartz substrate is shown in Fig. 6. 4.

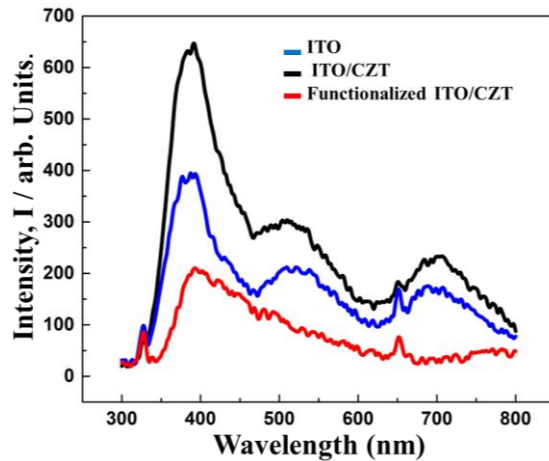


*Figure 6.4. Photoluminescence spectra of ITO, CZT/ITO and functionalized ITO/CZT films deposited over quartz substrate.*

The PL intensity signifies the recombination rate of photo generated electron holes. The intensity of the spectrum of CZT/ITO film is higher than ITO thin film, due to the increase in the transfer of photo generated electron and hole charge carriers across the surface. As prepared CZT/ITO film shows high emission at 400 nm and small emission at 325 nm. All the emission wavelengths places under the UV region, the excitation by the UV-VIS source is enough to generate photocurrent in the sample which leads to photocurrent sensing. After functionalization, the spectral intensity of the sample reduces because as the functionalized components (APTMS /antibody) are deposited on the CZT surface the generation of photo activated charge carriers responsible for luminescence intensity decreases. Fig. 6.5 shows the SEM as-fabricated CZT film over ITO coated glass annealed at 400°C and functionalized layer on the top of CZT.

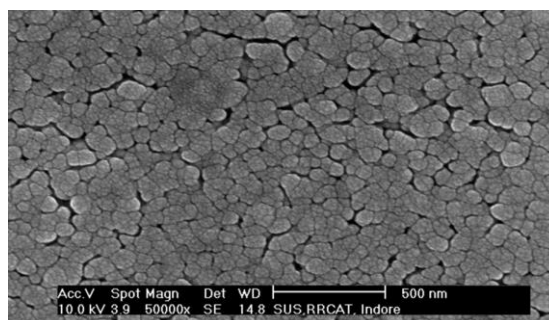


**Figure 6.5.** SEM of sol gel derived nanocomposite CZT thin film over ITO film

We observe that CZT layer formation by sol-gel method is uniform and crack-free. It can be observed that the CZT/ITO surface of the film exhibits compact regular morphology with a large surface area, which is favourable to the electron transfer and immobilization of biomolecules. Energy-dispersive X-ray spectroscopy (EDX) is an analytical tool used for the elemental analysis of thin films. Fig. 6.6 shows the EDX of the prepared thin film. The spectra reveal the presence of TiO<sub>2</sub>, ZnO and copper in the thin film. The atomic weight percentage of all elements in nanocomposite is shown in Table 6.1.

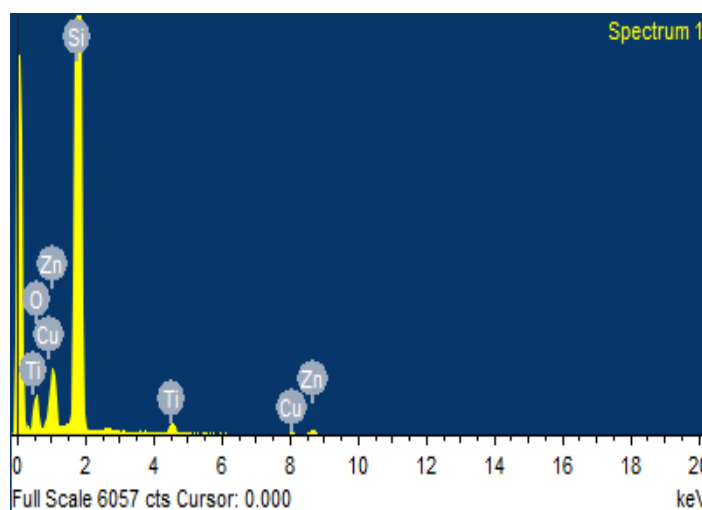


**Figure 6.6.** Energy dispersive analysis of X-ray (EDAX) spectra of CZT thin film deposited over glass substrate

**Table 6.1:** The weight% and atomic % of materials in CZT nanocomposite

| Elements | Weight% | Atomic% |
|----------|---------|---------|
| O K      | 16.16   | 27.28   |
| Si K     | 68.62   | 65.99   |
| Ti K     | 2.79    | 1.57    |
| Cu L     | 1.57    | 0.67    |
| Zn L     | 10.86   | 4.49    |
| Total    | 100.00  | 100.00  |

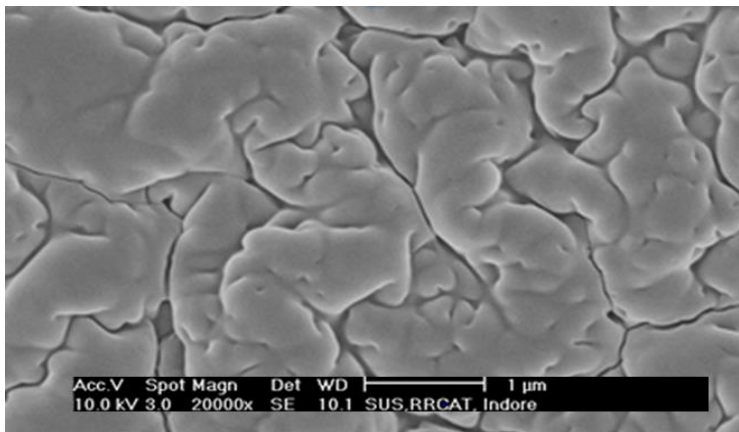


*Figure 6.7. SEM of APTMS functionalization over CZT/ITO thin film.*

Functionalization is a disordered process. Many thin layers are formed in silanization and antibody attachment. The deposition of APTMS makes the top surface non-uniform as shown in Fig. 6.7. APTMS silanization provides the base for bio conjugation reactivity to modify the surface to attach the antibody agents. The APTMS over CZT looks feasible, which provides good stability to the biosensor.

#### **6.4 Ellipsometry Characteristics**

Ellipsometry is a reflection-based technique to study the nanocomposite thin film surface and to determine the optical properties of thin films or bio layers [203]. The Ellipsometry measurement

depends on the change of polarization states. The polarization states depend on the after and before reflection from thin-film surface [204]. The simultaneous measurement of Ellipsometry parameters  $\Psi(\lambda)$  and  $\Delta(\lambda)$ , the magnitude and phase of the ratio of p and s polarized reflectivities provide rich information about nanocomposite thin films. Ellipsometry parameters in the reflection mode are  $\Psi$  and  $\Delta$ , given by [205]

$$\tan\Psi = R_p/R_s \quad (6.1)$$

$$\Delta = \delta_p - \delta_s \quad (6.2)$$

where  $R_p$  and  $R_s$  are the complex-valued reflection coefficients for the polarization parallel (p) and perpendicular (s) to the plane of incidence.  $\delta_p$  and  $\delta_s$  are the phases of  $R_p$  and  $R_s$ . As it is observed from perpendicular (s) to the plane of incidence.  $\delta_p$  and  $\delta_s$  are the phases of  $R_p$  and  $R_s$ .

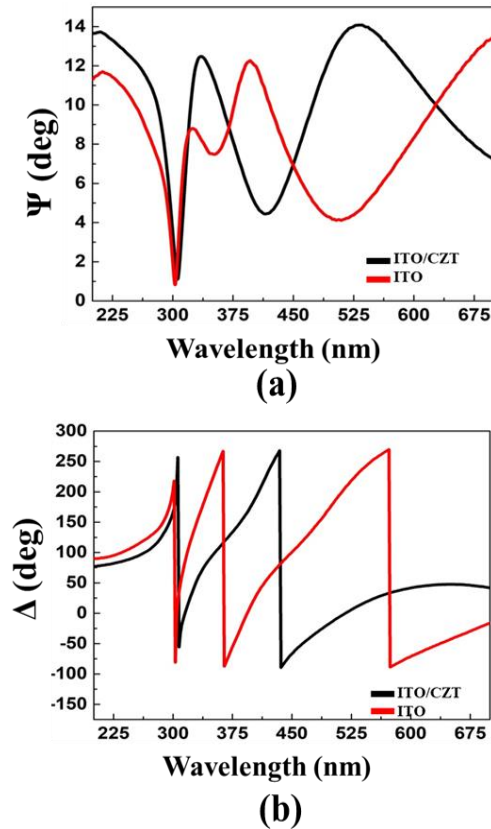


**Figure 6.8.** Spectral response of the Ellipsometry parameters  $\Delta$  for ITO thin film and CZT nanocomposite thin film over ITO film.

As it is observed from Fig. 6.8 the amplitude ( $\Psi$ ) spectrum shows a dip at reflected wavelength, while the phase ( $\Delta$ ) spectrum shows a steep change at the corresponding reflected wavelength. The dip shifts towards a longer wavelength as CZT nanocomposite is deposited on ITO. For ITO and CZT/ITO the corresponding wavelengths is 302.86 nm and 306.03 nm. There is a shift of 3.17 nm in wavelength when the sol-gel derived CZT is deposited over ITO thin film. The shift in wavelength is also observed in phase spectra where the steep change in slope is observed as the phase shifts towards a longer wavelength from 302.86 nm to 307.62 nm for ITO and CZT/ITO. This shift in amplitude and phase corresponds to the presence of CZT nanocomposite thin film over ITO film. The thickness of spin-coated CZT nanocomposite thin film observed by ellipsometer is 223 nm with n and k parameters of CZT/ITO are 2.221 and 0.205 at the wavelength of 630 nm.

## 6.5 Photocurrent Sensing Characteristics

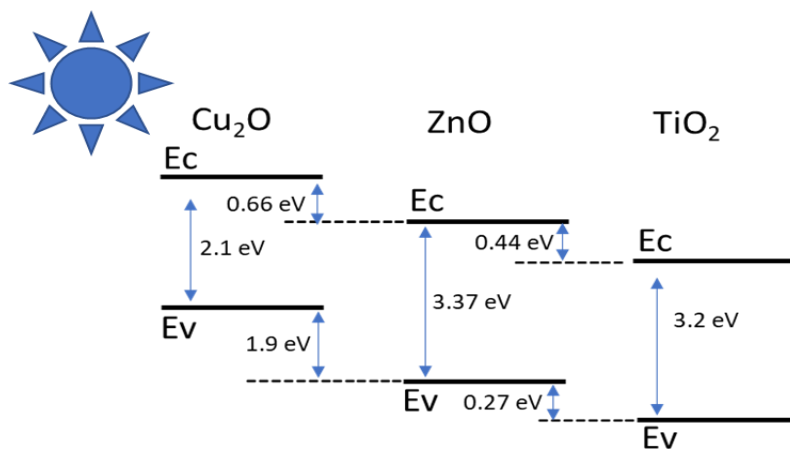


**Figure 6.9.** Schematic diagram of band gap, conduction band potential and valence band potential in Cu- ZnO/TiO<sub>2</sub> under UV-VIS radiation.

An excited electron, after irradiation of UV-Visible light on semiconductor, has greater energy than the bandgap of the semiconductor. The excited electron migrates from the fully occupied valence band (Ev) at the lower energy level of semiconductors to the empty conduction band (Ec) at the higher energy level. The photo-generated electrons and holes are trapped at surface sites or recombine to generate heat energy. For photocatalysis to occur trapped electrons

react with accepting or donating adsorbed species. The energy level at the top of the valence band determines the oxidizing ability of photo-generated holes while the energy level at the bottom of the conduction band of photo-generated electrons is reduction potential which determines the ability of the semiconductors to undergo oxidations and reductions. The charge transfer rate of electrons and holes can be determined by redox potential levels of adsorbate species and band gap energy. The band diagram of the CZT nanocomposite is shown in Fig. 6.9.

The property of ZnO and TiO<sub>2</sub> semiconductors is that their energy valence band and conduction band are more cationic and anodic compared to Cu<sub>2</sub>O which hinders the partial recombination of electrons and holes and favours the flow of electrons and holes from ZnO and TiO<sub>2</sub> to Cu<sub>2</sub>O. After irradiation from the light source, the photo generated electrons move from conduction bands of Cu<sub>2</sub>O to ZnO and then TiO<sub>2</sub> and holes traverse from TiO<sub>2</sub> to ZnO towards Cu<sub>2</sub>O. In this condition the ZnO act as the intermediate stage which favours the electron and hole transfer between conduction and valence bands of Cu<sub>2</sub>O, ZnO and TiO<sub>2</sub>. This process reduces the recombination rate of electrons and holes increasing the photocatalytic process of Cu–TiO<sub>2</sub>/ZnO. TiO<sub>2</sub> conduction band is less cathodic than the conduction band of ZnO and Cu<sub>2</sub>O. These charge carriers interact with the functionalized surfaces and E. coli and response is detected by source meter in terms of photocurrent. Thus under irradiation, this generation of photocurrent leads to biosensing. The broadband light source used for photocurrent measurement is 20 μW power with the wavelength of 200 nm to 800 nm and photocurrent measured at Keithley source meter under voltage range of 0 to 4 V in the step of 5 mV. The functionalized samples are incubated for 30 min in buffer solution. The photocurrent of prepared nanocomposite film with applied voltage varying from 0V to 4V is observed in Fig. 6.10. The photocurrent generated by ITO is small compared to CZT/ITO is deposited by spin coating process on ITO coated glass. The photocurrent observed for ITO thin film over glass is 120 μA and for CZT/ITO is 239 μA. The high photocurrent of

ITO/CZT indicates a large number of photo generated charge conduction of CZT film with ITO. The photocurrent reduces from 239  $\mu\text{A}$  at an applied voltage of 4V to 218  $\mu\text{A}$  on covalent immobilization of APTMS/antibody over the ITO/CZT film.

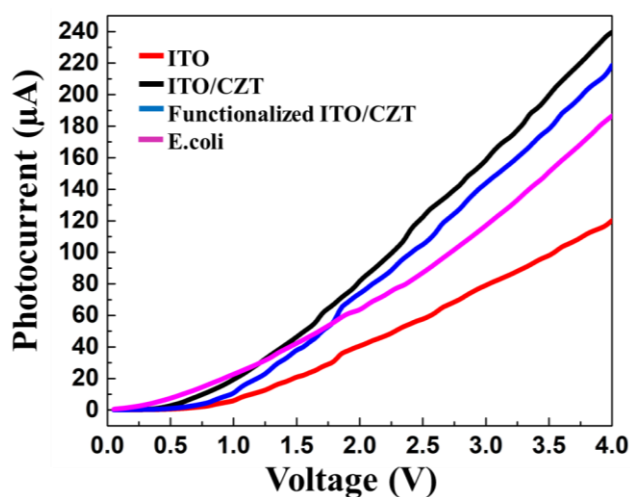


**Figure 6.10.** Photocurrent study of ITO, as prepared CZT/ITO thin film, functionalized top surface and after E. Coli concentration of  $10^3$  CFU/ml.

After silanization, the amine group creates a barrier to the conduction of ITO/CZT film by obstructing the transfer of charge carriers. After the addition of E. coli photocurrent exhibited a decrease of 14  $\mu\text{A}$ . This phenomenon is attributed to the hindrance effect caused by the interaction of APTMS and E. coli where electrons are blocked to reach the CZT/ITO surface and interfacial transfer of electrons stops. For photocurrent response of thin-film, E. coli cells are incubated for 30 minutes on the prepared film surface in varying concentrations from  $10^3$  CFU/ml to  $10^5$  CFU/ml. The maximum time for incubation is limited to 30 min because after 30 min the population of cells become so much that it is difficult to interact with single cells and affect the photocurrent response of the prepared film. Fig. 6.11 shows the photocurrent response of prepared biosensor ITO/CZT for E. Coli concentration varying from  $10^3$  CFU/ml to  $10^5$  CFU/ml. E. coli drop cast on the sensor film for detection. The volume of E. coli concentration for a sample is kept at 50  $\mu\text{l}$  in every measurement.

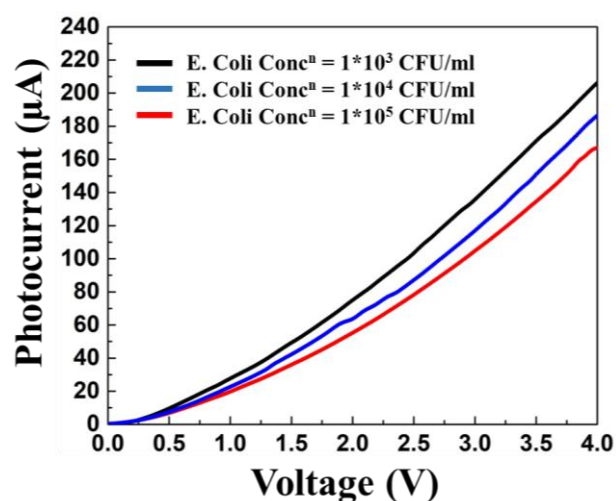


**Figure 6.11.** Photocurrent response of CZT/ITO film biosensor for varying concentration of *E. Coli*.

The highest photocurrent of 206  $\mu\text{A}$  was obtained at a cell concentration of  $10^3$  CFU/ml, 186  $\mu\text{A}$  for  $10^4$  CFU/ml and 167  $\mu\text{A}$  for  $10^5$  CFU/ml. The limit of detection of the proposed ITO/CZT sensing mechanism is limited to 1000 CFU/ml. The response time for ITO/CZT after the silanization process with bacterial cells is 20 seconds. It can be observed that photocurrent decreases gradually with the increased concentration of *E. coli*. This is due to the immuno-complex formed after interaction between *E. coli* and functionalization layer APTMS on the ITO/CZT surface. This immune complex of *E. Coli*, LB media, buffer and functionalization layer is act as insulation and obstructs the photo generated charge carriers transfer from top surface of ITO/CZT thin film.

The study of reproducibility of CZT/ITO bio sensor, two sets of samples are prepared and photocurrent response is measured against *E. coli* concentration. The value of photocurrent obtained after measurement for different concentration of *E. coli* is shown in Fig. 6.12. It is clear that response of any *E. coli* concentration is within the 3% range. The photocurrent sensing response of proposed CZT/ITO thin film sensor is reproducible. Selectivity of the photocurrent biosensor for the detection of *E. coli* is shown in Fig. 6.13 with *E. coli* and mixed culture pathogens.

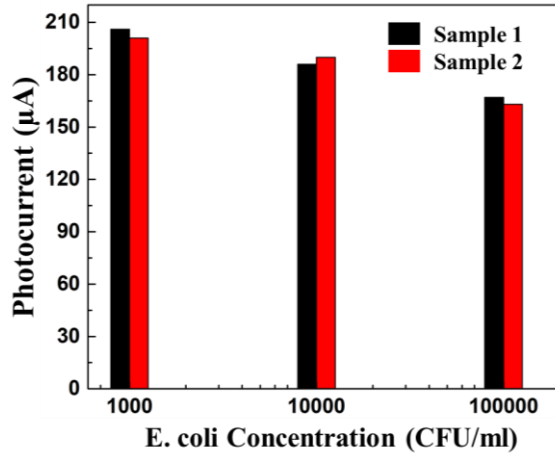


**Figure 6.12.** Reproducibility study of CZT/ITO thin film sensor towards *E. coli* concentration variation

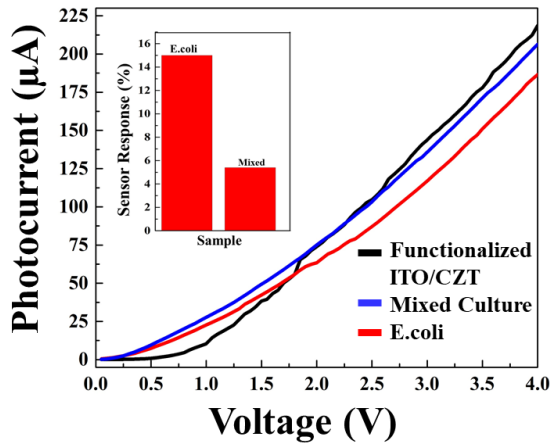


**Figure 6.13.** Photocurrent response of CZT/ITO film biosensor

Mixed culture includes *E. coli* and non-pathogenic bacterial solutions. The graph shows photocurrent for cell concentrations of  $10^4$  cells/ml. The inset shows a higher response for *E. coli* and a low response for mixed culture solution. The mixed culture response is lower as it consists of a smaller number of *E. coli* cells. Thus, the biosensor shows selective nature towards pathogenic *E. coli*. Other *E. coli* sensors report the limit of detection up to  $10^4$  CFU/ml using porous  $\text{SiO}_2$  via direct cell capture [122]; limit of detection  $10^3$  CFU/ml using over oxidized polypyrrole film with dielectrophoresis [123] and limit of detection  $7.4 \times 10^4$  CFU/ml using magnetic nanoparticle–antibody conjugates with microelectrode based impedance biosensor [206]. The nanocomposite CZT thin film over ITO coated glass increases the rate

of generation of photo-generated charge carriers and provides support to the APTMS layer to capture the E. coli. Thus, label-free and efficient biosensing has been demonstrated. The thin-film biosensor is highly efficient in the detection of food pathogens.

## 6.6 Summary

Label-free photocurrent biosensing platform based on ITO/CZT nanocomposite thin film has been demonstrated for the detection of E. coli in the buffer. The linear range of detection is  $10^3$  cells/ml to  $10^5$  cells/ml. To achieve a better photocurrent response, doping of copper in ZnO/TiO<sub>2</sub> nanocomposite is considered. SEM analyses confirm the uniform film morphology of CZT and functionalized CZT surface. At UV light irradiation, the photocurrent measurements of CZT revealed the favourable properties. The highest photocurrent of 206  $\mu$ A was obtained at a cell concentration of  $10^3$  CFU/ml. A change of 20  $\mu$ A is detected with a change in concentration of E. coli on the application of 4volts. The photocatalytic nanocomposite CZT is prepared and processed by a cost-effective sol-gel method. To verify the function of CZT/ITO thin film as a biosensor only E. coli is available to us. The results obtained for E. coli detection carry the potential for the proposed film sensor to be used as a label-free biosensing platform for other food pathogens. This method of detection provides flexibility with the electric control over optical characteristics opening a whole new class of integrated photonic devices for multidisciplinary applications. The film-based nanocomposite sensors have the disadvantage that the current density is low and the surface area for interaction with the analyte is small. The current density can increase by using the waveguide structure to achieve more absorption and confinement of light to enhance light-matter interaction. A combination of slot waveguide and photocatalytic materials can prove to be an effective optoelectronic platform to enhance the absorption and current density for biosensing applications.

## Chapter 7

### Electrically Controlled Nanocomposite Slot Structure for Optical Detection of Food-Borne Pathogen

The light absorption can be enhanced by confining modes in the waveguide which in turn maximizes the optical path length. The reduction in reflection and significant enhancement in optical path length can be achieved by proper engineering of structure geometry. An engineered nanophotonic optical slot structure is presented to provide enhanced light-matter interaction and flexibility to accommodate bio-sample. The advantage of using a nanocomposite slot waveguide structure is that it provides a higher current density than thin film. Photocurrent response of Cu-ZnO/TiO<sub>2</sub> (CZT) nanocomposite, is utilized to detect E. coli in the surrounding media of Luria Bertani broth (LB) solution. CZT nanocomposite is synthesised and prepared by a cost-effective sol-gel process, acting as an active layer in the structure, is responsible for the generation of photo-excited carriers which provide photocurrent on the application of a voltage. The fabricated structure with a synthesised nanocomposite slot waveguide exhibits a measured photocurrent of 22  $\mu$ A with LB media which increases to a value of 31  $\mu$ A in presence of E. coli. The limit of detection of fabricated biosensor for E. coli bacteria concentrations is 5000 CFU/ml from 10<sup>6</sup> CFU/ml saturated solution in liquid volume. A change in photocurrent of 9  $\mu$ A is obtained with E. coli on applying a low voltage of 3.5 volts. The combination of photocatalytic nanocomposite with engineered optical waveguide carries great potential for applications in bio-chemical detection and in realizing other integrated photonic devices with slotted nanocomposites.

#### 7.1 Detection of Food-Borne Pathogen

Many bacterial pathogens and toxins in food are responsible for the foodborne illness that is hazardous to human health. The detection methods to identify the existence of bacterial pathogens are very time

consuming and it requires essential instruments and trained manpower [180], [207]. The bacteria, viruses and parasites present in the foods are the main reason for foodborne diseases. Salmonella, Listeria, Campylobacter, and Escherichia coli are a few of the different bacterial pathogens that are responsible for foodborne diseases [112]. Because of its toxin generating capability, E. coli has drawn considerable attention, which can damage the intestinal lining, anaemia and stomach cramps with infective dose [56]. Raw uncooked food is the main reason for the transmission of E. coli to the human body. Many technological advancements have been made by new developments in nanotechnology to build smart biosensors for the detection of adulteration and contamination of foodborne pathogens [5], [113].

Passive optical methods for sensing, like the shift in resonance, have been studied widely but they have their own limitations where high losses can be a hindrance in sensing. An optical active method for sensing, which is referred to as an optoelectronic method, can efficiently detect an analyte even with low concentration. A combination of slot waveguide and photocatalytic materials can prove to be an effective optoelectronic platform for biosensing applications. Metal doped TiO<sub>2</sub> can affect the native attributes of the semiconductor catalyst and expand its photo response into the visible. The physiochemical properties like nontoxicity, biocompatibility, chemical stability water insolubility, chemical breakdown resistance is similar in TiO<sub>2</sub> and ZnO. Different methods and precursors of titanium and zinc oxide are proposed for the preparation of TiO<sub>2</sub>/ZnO nanocomposites [208], [209].

In this work, we present a bacteria-specific optical slot waveguide made up of nanocomposite Cu-ZnO/TiO<sub>2</sub> (CZT) as a label-free biosensor. The proposed sensing mechanism is based on a change in photo-current originated from the photo-excited carriers, on applying a voltage, in photocatalytic nanocomposite CZT to detect the presence of E. coli in Luria Bertani broth (LB) solution. A sol-gel derived photocatalytic nanocomposite CZT is used to create a slot waveguide structure for enhanced light-analyte interaction. The proposed

fabricated nanocomposite slot waveguide shows a photocurrent of 22  $\mu\text{A}$  with LB media as the surrounding medium and 31  $\mu\text{A}$  in presence of *E. coli*. The lower detection limit of the proposed device is reported to be 5000 CFU/ml, *E. coli* concentration from a saturated solution. The LB media and *E. coli* can be flexibly accommodated on the slot cladding regions. The combination of optical slot structure and photocatalytic nanocomposite can not only be used as a label-free sensing platform, but it can also offer other electro-optic functions for integrated photonic devices.

## 7.2 Slot Waveguide Design

The proposed electrically controlled nanophotonic slot structure based on a photocatalytic nanocomposite biosensor, shown in Fig. 7.1, is designed and fabricated on a silicon substrate.

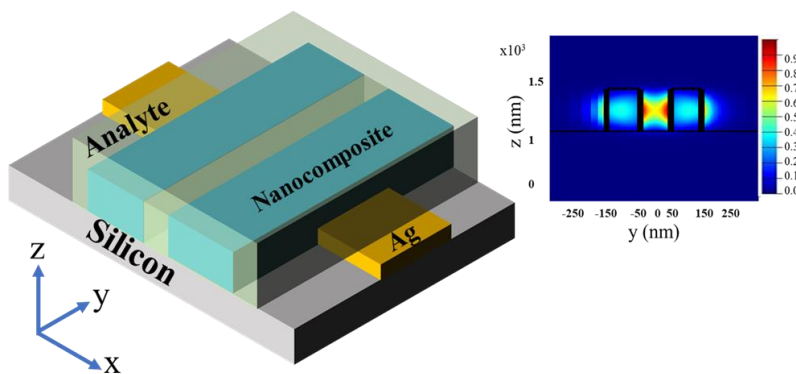


**Figure 7.1.** The schematic of the nanocomposite slot waveguide pathogen biosensor. Inset shows the electric field confinement in slot waveguide.

The slot region of 100 nm is created in 0.35  $\mu\text{m}$  wide rib of CZT photocatalytic nanocomposite created by using electron-beam lithography followed by lift-off with the thickness of 300 nm. The real value of the refractive index of nanocomposite material is taken 2.21 which was measured and confirmed by the Ellipsometry of thin films of nanocomposite material. These low index nanocomposite ribs confine the optical mode into the slot region (filled with analyte) and some part in nanocomposite rib also as shown in the inset. The amplitude distributions (of mode field) in slot waveguide filled with

LB media (Refractive index = 1.338) is shown in Fig. 6.2. The mode distribution is most convincing with X cut of slot waveguide which supports propagation of quasi-TE mode inside slot waveguide. As

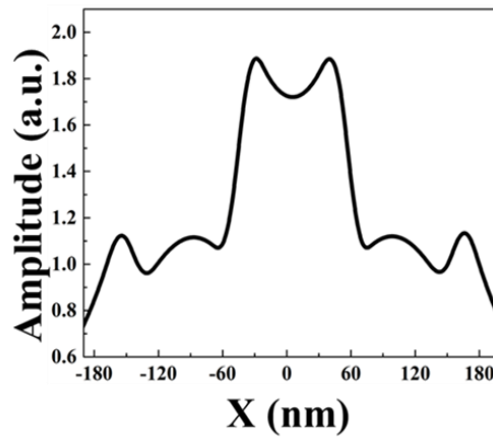


**Figure 7.2.** Mode field distribution profile of photocatalytic nanocomposite slot waveguide.

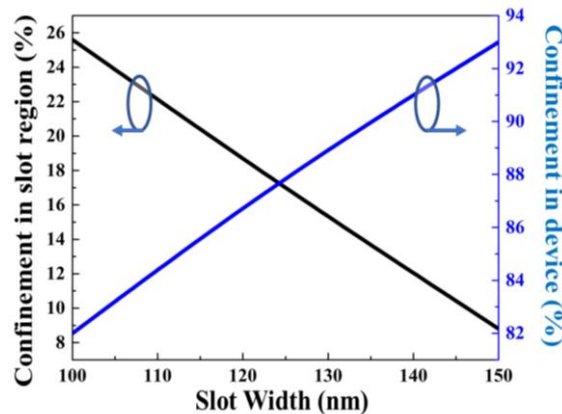


**Figure 7.3.** The effect of variation in slot width on the confinement of optical mode in slot region and whole device

shown in Fig.7.2 high electric field confinement in the slot region enables better interaction of optical mode with sensing material. When LB media is used as medium, the mode field distribution is substantially lying in the slot region and also on outside the waveguide region due to low contrast of refractive index with nanocomposite.

The simulation of the proposed slot waveguide is performed using FDTD simulation software. The calculated optical confinement of slot waveguide is 71%. We experimentally investigate the effect of nanocomposite material slot waveguide on the sensing of E. coli in LB

media. The effect of variation in slot width on the confinement of optical mode is slot region and the whole device is shown in Fig.7.3 The optical confinement in slot region decreases with increasing the slot width and optical confinement in whole device increases because as the slot width increases the optical mode tends to propagate in high refractive index region which increases confinement in the whole device. The rib width if kept at 100 nm and the thickness of the slot waveguide is 300 nm.

### **7.3 Fabrication of Slot Waveguide**

CZT nanocomposite is prepared by the sol-gel process. The first solution is prepared by mixing 20 ml of 2-methoxyethanol in 3.5 ml of Titanium (IV) n-butoxide with 1.3 ml of acetylacetone. The mixture is stirred vigorously for 30 min at room temperature. Acetylacetone is added as a chelating agent to decrease the reactivity of Titanium (IV) n-butoxide. Acetic acid is added to the solution after 30 min. Glacial acid is used for hydrolysis via an esterification reaction. A molar ratio between acetic acid and Titanium (IV) n-butoxide of 0.2 was utilized. For the second solution zinc acetate dihydrate (2.2 gm), 2-methoxyethanol (20 ml) and 1.2 ml of diethanolamine (DEA) are mixed to form a second precursor solution. The mixture was stirred at 50°C for 90 minutes to produce a clear homogeneous solution. Copper doped ZnO/TiO<sub>2</sub> (CZT) sol prepared by mixing of TiO<sub>2</sub> sol and ZnO sol together in a 1:1 molar ratio. The solution was stirred for 30 min at 500 rpm, afterwards, cupric chloride is added to the solution. The final solution was aged for 48 hours to obtain the gel solution. Two type of solutions formed ZnO/TiO<sub>2</sub> and copper doped ZnO/TiO<sub>2</sub>.

Process flow of fabrication of nanocomposite slot waveguide structure shown in Fig. 7.4 (a-e). The piranha cleaning process is used to clean the silicon wafer followed by HF dip that removes all oxides and contaminants from the top silicon surface. Afterward 2% concentrated PMMA mix in the anisole solution. This solution is spin-coated over the silicon surface Fig. 7.4 (a). After coating, the wafer is

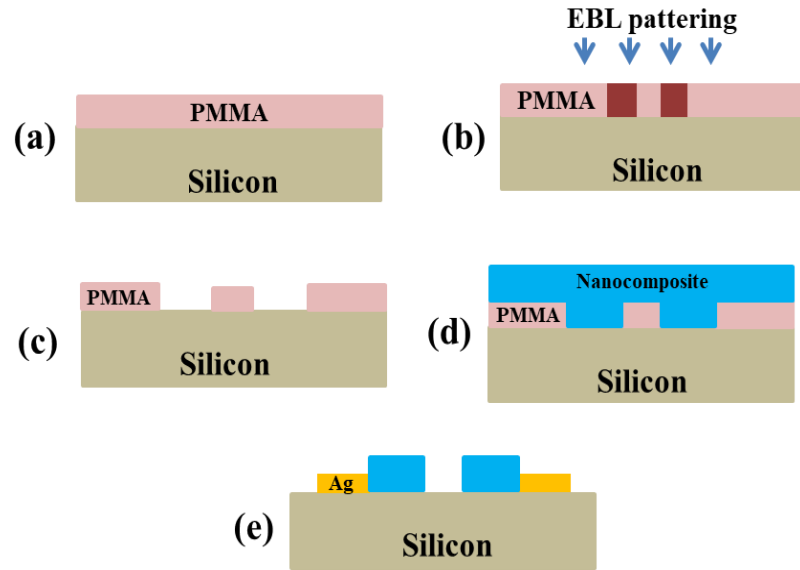


**Figure 7.4.** Process steps for the fabrication of slot waveguide

then baked for 20 min at 200<sup>0</sup>C. Electron beam lithography is used to pattern the PMMA at 10KV with dose exposure of 120 $\mu$ C/cm<sup>2</sup>. After patterning wafer is developed for 1 min to remove the undesired part of resist from the sample as shown in Fig. 7.4 (b). We obtained the active silicon area in the form of two ribs separated by 200 nm width PMMA as shown in Fig. 7.4 (c). Metal oxide sols were spin-coated over the silicon surface at 2000 rpm for 30 seconds as in Fig. 7.4 (d). The coating was first dry at a low temperature of 100 °C for 15 min then after thin films were dried at a high-temperature of 250<sup>0</sup>C for 15 min. The experiment was repeated 3 times to obtain the desired thickness of the films ~ 250 nm. A acetone bath is performed that removes the residual PMMA from the sample to form a slot waveguide of nanocomposite material and silver contacts are formed as shown in Fig. 7.4 (e). The device is annealed at 500<sup>0</sup>C for 2 hours in air at a heating rate of 5<sup>0</sup>C/min to develop a homogeneous and crystalline nano-composite slot waveguide. The spin-coated thin film samples on quartz glass are prepared for morphological and optical characteristics of nanocomposites. The annealing helps the grain growth by the crystallization of the microstructure of nanocomposite material.

#### 7.4 Morphological properties of Nanocomposite

The tauc plot of  $(\alpha h\nu)^2$  vs  $h\nu(\text{eV})$  shows the optical band gap of nanocomposites as shown in Fig. 7.5. The bandgap energy and absorption coefficient can be expressed by :

$$(A h\nu)^n = A h\nu - E_g \quad (7.1)$$

where A is the constant of the film,  $\alpha$  is the absorption coefficient,  $h\nu$  is the photon energy and  $E_g$  is the optical bandgap. For  $(\alpha h\nu)^2$ ,  $n=2$  gives indirect bandgap and when the curve is extrapolating to the energy axis it gives the optical bandgap energy  $E_g$ . The estimated value of the bandgap for spin-coated nanocomposite thin films is 2.8 eV and 2.7 eV,  $\text{TiO}_2/\text{ZnO}$  and  $\text{Cu-TiO}_2/\text{ZnO}$  and nanocomposite thin films deposited on quartz glass respectively.

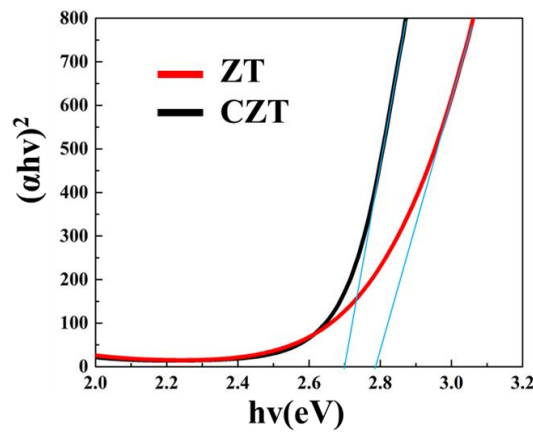


**Figure 7.5.** Bandgap transition energies of  $\text{ZnO}/\text{TiO}_2$  and  $\text{Cu-ZnO}/\text{TiO}_2$  using Tauc model.

The optical transmission spectra of sol-gel derived CZT nanocomposite deposited by spin coating on the quartz substrate is measured at a wavelength range of 200-1000 nm shown in Fig 7.6.

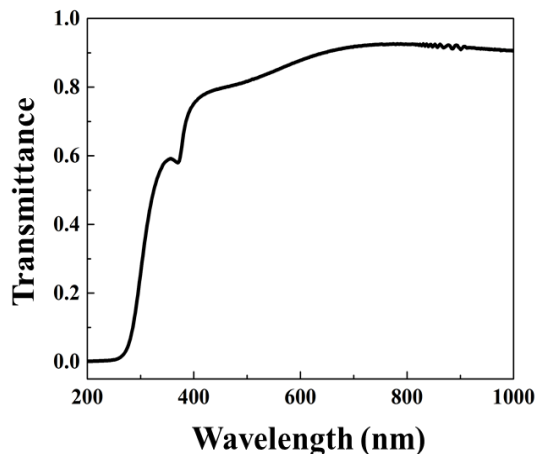


**Figure 7.6.** Transmittance of CZT film deposited on the Pyrex glass substrate.

CZT thin film exhibits high transmission of > 60% in UV to visible region shows the absorption edge around 300 nm.

Photoluminescence analysis is performed to analyze the optical properties, energy transition levels, charge recombination rate of photogenerated charge carriers in nanocomposites. Fig. 7.7 shows the PL spectra of TiO<sub>2</sub>/ZnO and Cu-TiO<sub>2</sub>/ZnO nanocomposite thin films on quartz glass substrate at room temperature. The violet emission at 389 nm is very strong and originates from electron transition in Zn interstitial levels. The graph shows blue-green transition is at 525 nm and weak emission at 600 nm in the visible region. The emission arose from intrinsic defects such as Zinc, Copper and oxygen interstitials in composite films. The emission intensity of Cu doped ZnO/TiO<sub>2</sub> is weaker than ZnO/TiO<sub>2</sub>. It means that doping of Cu in ZnO/TiO<sub>2</sub> suppresses the recombination of photogenerated electron-hole pairs compares to ZnO/TiO<sub>2</sub>. CZT shows strong emission around 400 nm and weak visible emission intensity. Strong UV emission of CZT attributed to the high quality of the film.

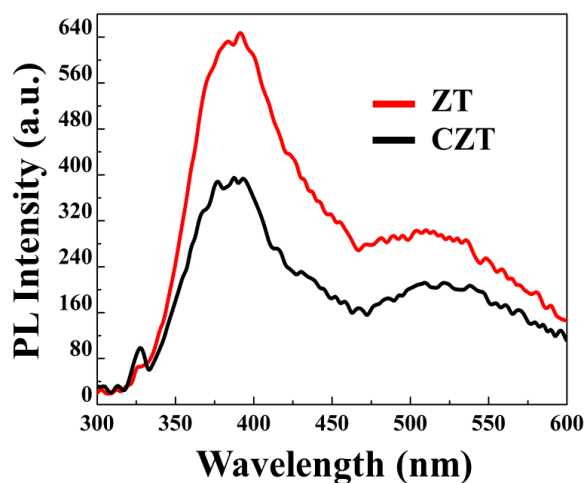


*Figure 7.7. Photoluminescence spectra of ZnO/TiO<sub>2</sub> and Cu-ZnO/TiO<sub>2</sub> of nanocomposite material deposited on quartz substrate annealed at 500°C*

Raman spectroscopy is employed for phase identification of sol-gel synthesized nanocomposite ZnO/TiO<sub>2</sub> and Cu-ZnO/TiO<sub>2</sub> thin films deposited by a spin coating method. The Raman band for the

appearance of peaks for ZnO/TiO<sub>2</sub> at 220 cm<sup>-1</sup>, 300 cm<sup>-1</sup>, 450 cm<sup>-1</sup> are attributed to A<sub>1</sub>(TO), B<sub>1g</sub>, and B<sub>2g</sub>.

The Raman spectra of the annealed nanocomposite thin films of copper and ZnO doped nanocomposites along with their modes are shown in The peaks 300 cm<sup>-1</sup>, 440 cm<sup>-1</sup> are observed for CZT attributed to Eg, E<sub>2</sub>(H) and B<sub>2g</sub>.

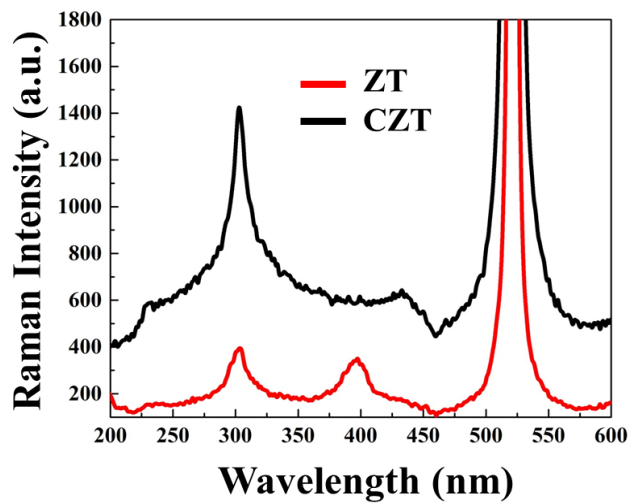


**Figure 7.8.** Raman spectrum of nanocomposites thin films of ZnO/TiO<sub>2</sub> and Cu-ZnO/TiO<sub>2</sub> deposited on silicon substrate.

Fig. 7.9 shows the surface morphology of Cu-ZnO/TiO<sub>2</sub> thin films with an RMS value of 2.052 nm. The nanocomposite layer deposited at 3000 rpm by spin coating process produces uniform thin films. The lower roughness of films represents good homogeneity. As seen from

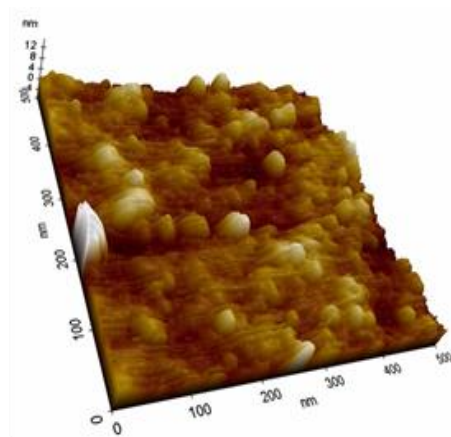


**Figure 7.9.** AFM morphology of Cu-ZnO/TiO<sub>2</sub> thin film spin coated on silicon substrate and calcined at 500°C.

the morphology the roughness of the layer is due to the formation of globular shape particles when ZnO/TiO<sub>2</sub> is doped with copper. The morphology of nanocomposites films shows that thin films are formed with dense and compact structural morphology which makes the film smoother.

## 7.5 Photocatalytic Degradation

The photocatalytic nanocomposite is a crucial part of the device which enables optical absorption to initiate electronic transition across bandgap. On optical excitation, the excited electron drifts from the occupied valence band ( $E_v$ ) at lower energy to the empty conduction band ( $E_c$ ) of the semiconductor [198], [210]. The photogenerated electrons and holes are trapped at surface sites or recombine to generate heat energy. For photocatalysis to occur trapped electrons react with accepting or donating adsorbed species. The top energy level of the semiconductor valence band defines the oxidizing ability of photo-generated holes while the bottom energy level of the conduction band of photo-generated electrons is the reduction potential that determines the semiconductor's ability to go through the oxidations and reductions. The charge transfer rate of electrons and holes using Redox potential levels can be used to find bandgap energy [211], [212]. A semiconductor can donate electrons to holes when the donor level of the redox potential is above the valence band and below the conduction band position in the case of the acceptor. To investigate the photocatalytic property of the nanocomposites we take methyl orange (MO) dye as a pollutant.

Photocatalytic activity of the nanocomposites materials is observed by decolourization of methyl orange (MO) solution at room temperature. In the process of preparing the solution, 0.3 gm MO is dissolved in the vessel of 500 ml of water. Before illumination, a nanocomposite solution is added and constantly stirred in a dark room for 1 hr to attain equilibrium between nanocomposites and methyl orange. After, the solution is illuminated by a UV-VIS light source.

When MO solution is added to the nanocomposite solution, in the presence of light decolourization of MO dye occurs which shows the presence of photocatalytic process.

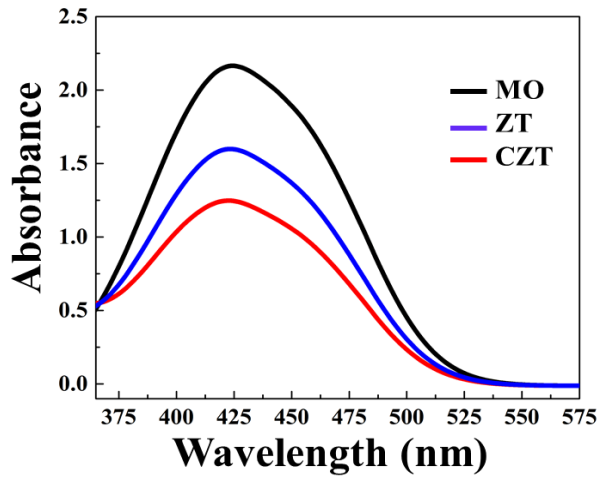


**Figure 7.10.** UV-VIS absorption spectra of MO(Methyl Orange) with ZnO/TiO<sub>2</sub>, Cu-ZnO/TiO<sub>2</sub> nanocomposites solutions.

Fig. 7.10 shows absorption spectra of nanocomposites with methyl orange (MO). From spectral data, we can observe the strong cut off at 425 nm. All nanocomposites show strong absorption at a wavelength range of 350 nm to 500 nm [213]. The degradation of MO after photocatalytic reaction can be observed in the C/C<sub>0</sub> graph with the color of the solution before and after irradiation in Fig. 7.11. The degradation rate is calculated by C/C<sub>0</sub> where, C<sub>0</sub> is taken as the initial

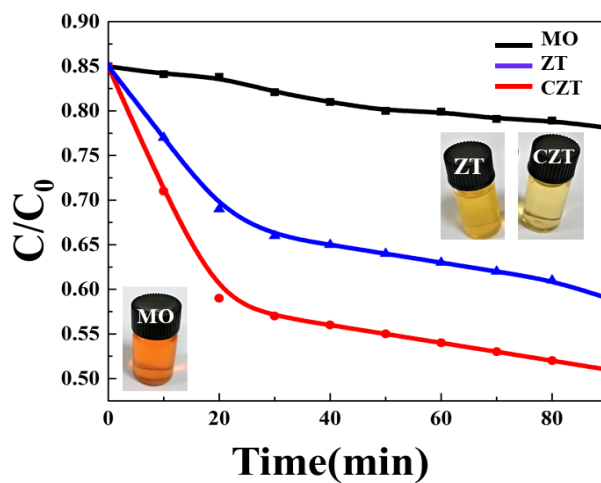


**Figure 7.11.** Plot of C/C<sub>0</sub> with different irradiated time using nanocomposites solution under UV-VIS irradiation in 10 ml ZnO/TiO<sub>2</sub>, Cu-ZnO/TiO<sub>2</sub> nanocomposites solutions. Degradation of MO dye is shown dark orange solution (before irradiation) and light-yellow transparent nanocomposites solutions (after

concentration of the dye,  $C$  is taken as the concentration of MO after irradiation for the time of  $t$  (min). The inset of Fig. 7.11 shows the degradation of MO when mixed with nanocomposite ZnO/TiO<sub>2</sub> and Cu-ZnO/TiO<sub>2</sub>. MO dye degrades very less when illuminated in the absence of nanocomposites. We achieve up to 50% of total MO dye degradation in 90 minutes duration. It is observed that MO dye degrades less in the absence of nanocomposites. Fig. 6711 depicts that the CZT nanocomposite shows higher efficiency in the degradation of MO when compared to other nanocomposites.

## 7.6 Sensing Characteristics

The electrical control in the optical characteristics of the device is enabled by using photocatalytic nanocomposite on applying a voltage. CZT is shown to provide a photocurrent, well above dark current (noise) level, under an applied voltage. The experimental setup of biosensors showing in Fig. 7.12 includes a 20  $\mu$ W Xe lamp visible light source of wavelength 200 nm to 700nm, Keithley source meter and 5 axis motorized stage. A 20  $\mu$ W Xe lamp visible light source with 40 $\times$  microscope objective confined light in butt coupler of 4  $\mu$ m width x 500 nm height which is used as light coupling to slot waveguide.

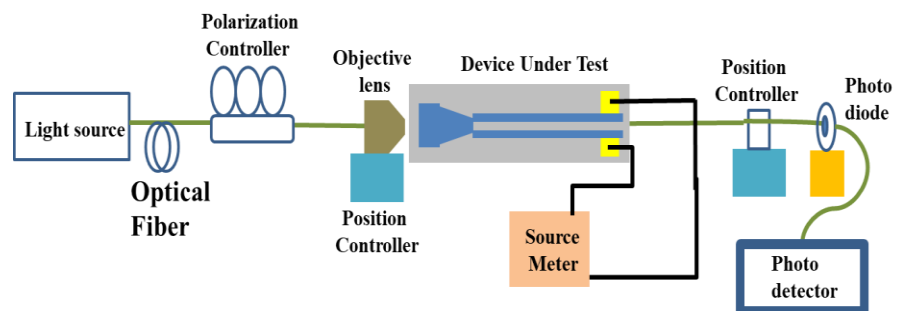


*Figure 7.12. Experimental setup of CZT slot waveguide biosensor*

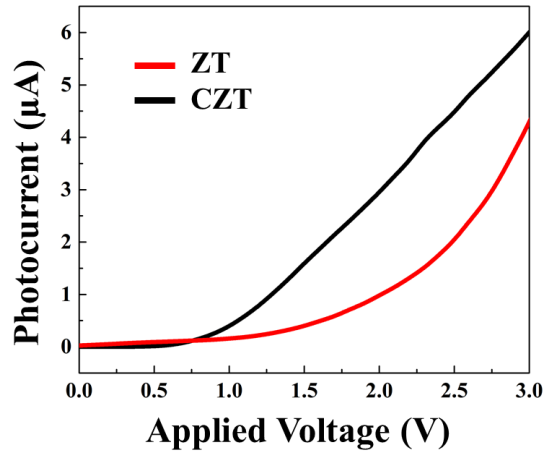


**Figure 7.13.** Photocurrent of ZT and CZT slot waveguide when bias potential is applied.

The 450 nm wavelength gets confined and propagates along the waveguide in the slot region. This UV-VIS light on the nanocomposite material excites the photogenerated charge carriers. The voltage is applied in the range from 0V to 3.5 V from the source meter and the photocurrent is recorded. The ZT and CZT photocurrent with an applied bias potential is shown in Fig.7.13. The higher slope of CZT photocurrent than ZT exhibits more photogenerated charge carriers. The highest current observed is 6  $\mu\text{A}$  for CZT nanocomposite with Cu concentration of 0.01% and 4  $\mu\text{A}$  for ZnO/TiO<sub>2</sub> nanocomposite without copper doping. Small doping of copper in ZnO/TiO<sub>2</sub> affects the generation of charge carriers. The photocurrent response of the CZT slot waveguide is shown in Fig. 7.14.

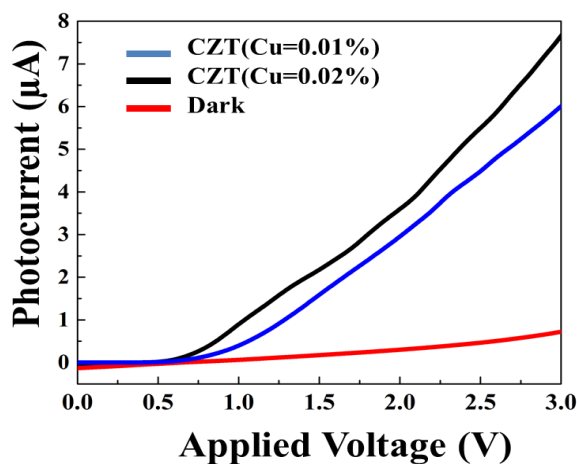


**Figure 7.14.** Photocurrent and dark current in CZT slot waveguide when bias potential is applied.

We observed the dark current of 1  $\mu\text{A}$  under potential bias. When the device is illuminated by light and voltage is applied, the photo charge carriers are generated and constitutes the photocurrent. The silver electrode forms a Schottky interface with nanocomposite. Under the increasing bias voltage to 3V, the photocurrent increases from 1.5  $\mu\text{A}$  to 7.5  $\mu\text{A}$ . The photocurrent increases as the concentration of Cu (wt%) increases from 0.01% to 0.02% in ZnO/TiO<sub>2</sub> nanocomposite. The photocurrent response of nanocomposite slot waveguide with LB media as surrounding medium and E. coli as the analyte is shown in Fig. 7.15. The photocurrent observed at 0.01% Cu concentration is 6.03  $\mu\text{A}$  and 7.5  $\mu\text{A}$  for 0.02% of copper in ZnO/TiO<sub>2</sub>. The photocurrent increases due to the availability of charge carriers that come from the doping of Cu in ZnO/TiO<sub>2</sub> nanocomposite. This doping level leads to the increment of photocurrent in CZT nanocomposite. We take ZT and CZT nanocomposite slot waveguides to analyse the detection of E. coli through the change in photocurrent. In Fig. 7.15 we observed the dark current of 1  $\mu\text{A}$  in ZT (ZnO/TiO<sub>2</sub>). When the device is illuminated by light and a voltage is applied, photocurrent starts rising to 10  $\mu\text{A}$  at a maximum voltage supply of 3.5 V.

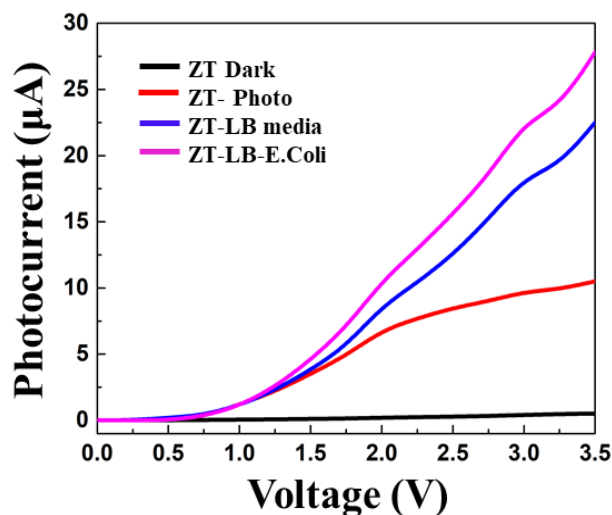


**Figure 7.15.** Photocurrent variation as a function of voltage in ZnO/TiO<sub>2</sub> (ZT) nanocomposite with LB media and E. coli

When the surrounding medium is LB media the photocurrent increases to 22  $\mu\text{A}$ , and when *E. coli* is added as the analyte, photocurrent response increases to 27  $\mu\text{A}$  at the maximum voltage of 3.5 V. We observe the change in photocurrent of 5  $\mu\text{A}$  which authenticates the detection of *E. coli* bacteria in LB media. In the case of CZT in Fig. 6.16 the photocurrent increases due to the availability of extra free

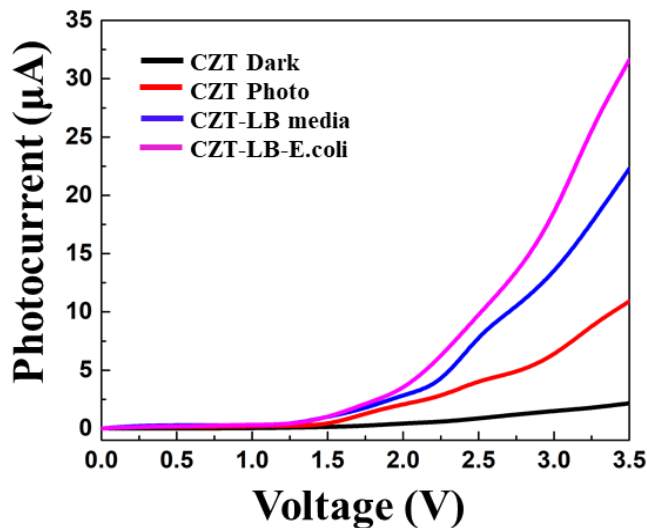


**Figure 7.16.** Photocurrent variation as a function of voltage in Cu-ZnO/TiO<sub>2</sub> (CZT) nanocomposite with LB media and *E. coli*.

charge carriers that come from doping of Cu in ZnO/TiO<sub>2</sub> nanocomposite. This doping level leads to the increment of photocurrent in CZT nanocomposite, due to more availability of more photo-generated charge carriers that leads to large photocurrent than ZT.

The observed dark current in Fig. 7.16 is 2  $\mu\text{A}$ , and after being illuminated by light source photocurrent increases with applied voltage and reaches up to 11  $\mu\text{A}$ . For CZT nanocomposite-based slot waveguide exhibits a photocurrent of 22  $\mu\text{A}$  with LB media which increases to a value of 31  $\mu\text{A}$  in presence of *E. coli* as shown in Fig. 6.16, with a low voltage of 3.5 volts. When we increase the supply voltage by more than 3.5 V, LB media disintegrates and is converted to a white opaque solution. This significant change of 9  $\mu\text{A}$  in photocurrent after the addition of *E. coli* to LB media represents efficient label-free detection. The amount of *E. coli* used as an analyte

to cover the device as cladding is 5  $\mu\text{l}$  which is 5000 CFU/ml concentration taken in proportion to the  $10^6$  per ml total number of E. coli present in solution. Thus, we can conclude that the CZT nanocomposite slot waveguide generates more photocurrent difference in sensing of E. coli compared to ZnO/TiO<sub>2</sub> which makes the sensor bacteria specific.

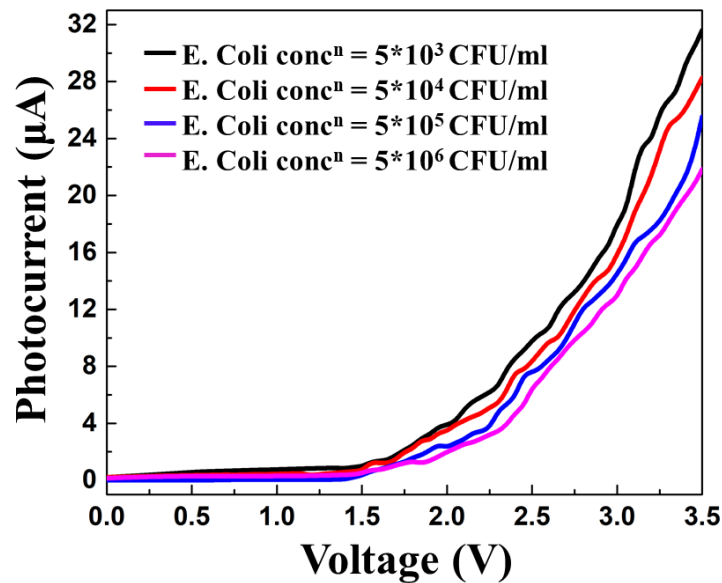


**Figure 7.17.** Photocurrent response of CZT nanocomposite biosensor for varying concentration of E. Coli.

Fig. 7.17 shows the photocurrent response of prepared biosensor CZT for E. Coli concentration varying from  $5 \times 10^3$  CFU/ml to  $5 \times 10^6$  CFU/ml. The volume of E. coli solution is kept at 5  $\mu\text{l}$  for different concentrations in every measurement. It can be observed that photocurrent reduces as the concentration increases. This is due to the formation of immuno-complex after interaction between E. coli and CZT surface. This immune complex of E. Coli and LB media is acts as insulation and obstructs the photogenerated charge carriers transfer from the top surface of CZT nanocomposite. The highest photocurrent of 31  $\mu\text{A}$  obtained at cell concentration of  $5 \times 10^3$  CFU/ml, 28  $\mu\text{A}$  for  $5 \times 10^4$  CFU/ml, 25  $\mu\text{A}$  for  $5 \times 10^5$  CFU/ml and 21  $\mu\text{A}$  for  $5 \times 10^6$  CFU/ml. The limit of detection of the proposed CZT slot waveguide sensing mechanism is turn out to be 5000 CFU/ml.

Selectivity of the nanocomposite slot waveguide photocurrent biosensor for the detection of E. coli is shown in Fig. 7.18 (a) with E.

coli and mixed culture pathogens. Mixed culture includes E. coli and non-pathogenic bacterial solutions. The graph shows photocurrent for cell concentration of  $5 \times 10^4$  cells/ml. Fig.7.18 (b) shows a higher response for E. coli and a low response for mixed culture solution. The mixed culture response is lower as it consists of a smaller number of E. coli cells. Thus, the biosensor shows selective nature towards pathogenic E. coli.

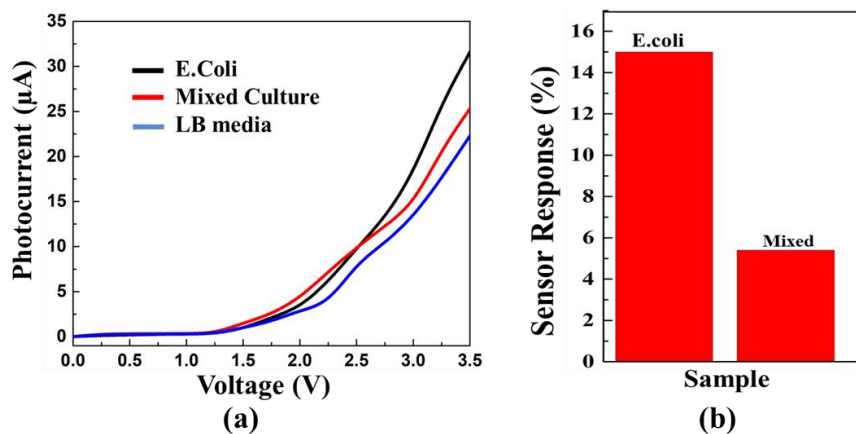


**Figure 7.18.** Photocurrent response of CZT nanocomposite biosensor with *E. coli* and with mixed culture.

Outer membranes of bacteria are formulated of different biomolecules like proteins, glycoproteins, lipopolysaccharides and peptidoglycan and carbohydrates. Due to the charge bearing properties of these biomolecules, bacterial membrane acquired potential. A redox compound expelled by *E. coli* acts as an inter-agent to transfer electrons. Bacterial cells can synthesize redox compounds transport chains. Cytochromes and quinones are the compounds synthesized by bacteria, are electrons carriers [183], [214], [215]. Redox elements in the electrochemistry of *E. coli* perform electron transfers. In LB media amino acids, carbohydrates and oligopeptides are reduced to generate ions and electrons when excited by voltage and optical sources. In the photocatalytic detection process when CZT and other nanocomposites mix with methyl orange or *E. coli*, degradation of dye or organic material starts. The degradation of organic materials in the photocatalytic process is a slow process. Gram-negative bacteria *E. coli* has a double cell wall that makes it less susceptible to surface

damage. It takes more than 90 min to degrade organic material in the presence of light sources and nanocomposite material. *E. coli* has the ability to survive under different environmental redox surroundings by embracing different metabolic rates. Our proposed device sensor takes less than a minute to give a response signal for the detection of *E. coli*. Hence bacteria can be detected much before the anti-bacterial process of photocatalysis starts.

### 7.7 Microfluidics Channel

For an integrated optical biosensing system to work effectively it should utilize less amount of analyte. The microfluidic channel should be designed from inert biological materials. The most common material used for the microfluidic channels is PDMS. Standard photolithography techniques are used to fabricate the PDMS microfluidic channel [216], [217]. The channel is bonded to a device by treating with oxygen plasma. Fig.7.19(a) shows the 3D sketch of the microfluidic channel incorporated over the CZT slot waveguide. The cross-sectional view of the sensing device showing the various layers in device structure are shown in Fig.6.19(b).

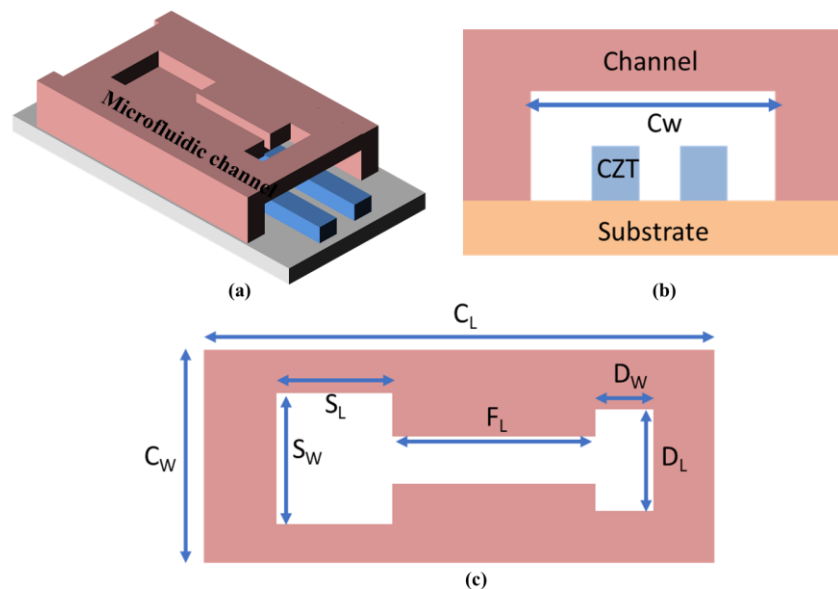


**Figure 7.19.** (a) 3D sketch of microfluidic channel over the slot waveguide. (b) Cross-section view of all layers in the sensing device. (c) Dimensions of microfluidic channel

The width and thickness of the microfluidic channel shown in Fig. 7.19 (c), ( $C_L \times C_W$ ) is kept at 5 mm and 1 mm, to easily accommodate the

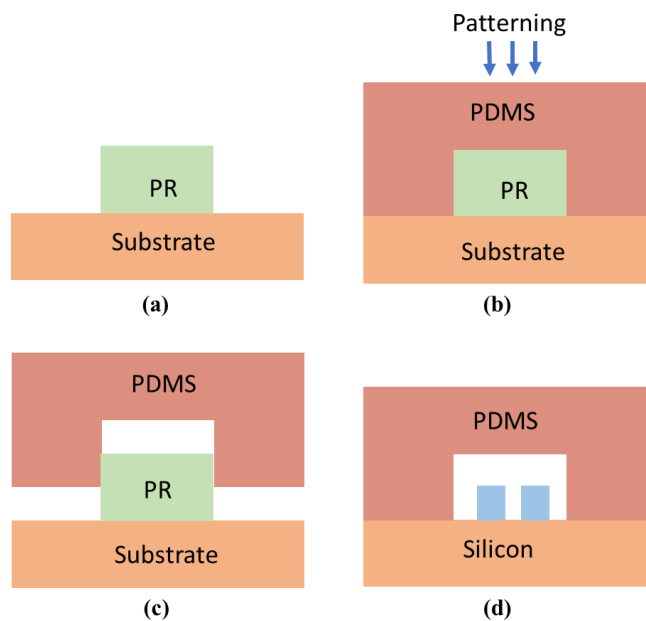


**Figure 7.20.** Process steps for fabrication of PDMS microfluidic channel

samples. The storage of dimension ( $S_L \times S_W$ ) 500  $\mu\text{m}$  by 500  $\mu\text{m}$  and flow channel  $F_L$  of length 2 mm is formed in the middle of the microchannel. The drop area ( $D_L \times D_W$ ) is formed at the end of flow channel length with the dimension of 300  $\mu\text{m}$  by 50  $\mu\text{m}$ , from where the analyte flow over the device.

The objective of designing microfluidic devices is only simple delivery of fluid or analyte. The design requires only a single mold and a single layer of PDMS structure. The processing steps for the fabrication of the microfluidic channel is shown in Fig.7.20. First using standard lithography techniques photoresist molds are prepared as in Fig. 7.20 (a). SU-8 photoresist is the common material used in the developing of molds. PDMS microfluidic channels will be cast by using these photoresist molds. To prepare a fluidic device PDMS is synthesized in the petri dish and pour over the photoresist mold and place in the vacuum chamber. Freshly prepared PDMS contains uncrosslinked polymers that contaminate the devices. To prevent this PDMS channel is kept in toluene, acetone and water for one day each. The PDMS channel then lifts from the substrate and is aligned and pressed into

contact over desired optical device for permanent bonding by oxygen plasma in Fig 7.20 (c) and (d). After baking overnight, the channel is attached to the device.

## 7.8 Summary

A biosensor based on an optical slot waveguide made up of photocatalytic nanocomposite Cu-ZnO/TiO<sub>2</sub> (CZT) is proposed for the label-free detection of *E. coli*. To achieve a high photocurrent doping of copper in ZnO/TiO<sub>2</sub> is considered. AFM and Raman's analysis confirm the uniform film morphology. CZT film exhibited a high transmittance in the visible spectral range. The photocatalytic nature of the CZT offers electrical control over the optical characteristics of the engineered optical waveguide. The proposed novel device design together with the adopted sensing mechanism is shown to efficiently detect the presence of *E. coli* in LB media by measuring the change in photocurrent. The fabricated sensor, under the applied voltage of 3.5 volts, exhibits a 9  $\mu$ A change in the photocurrent in presence of *E. coli* in LB media. The photocatalytic nanocomposite CZT is prepared and processed by a cost-effective sol-gel method and the slot is created by electron beam lithography followed by a lift-off process. The slot structure of the nanocomposite waveguide provides strong optical confinement in a low index region which improves the light-analyte interaction for efficient detection of *E. coli*. The proposed device is able to flexibly detect a change of the order of 0.05 in the refractive index in Lb media and *E. coli*. It is attributed to the better charge transfer property of CZT and *E. coli*. The results obtained to carry the potential for the proposed device to be used as a label-free biosensing platform which provides flexibility with the electric control over optical characteristics opening a whole new class of integrated photonic devices for multidisciplinary applications.

## Chapter 8

### Conclusion and Future Scope

On-chip detection of viral infections on optical sensing systems requires silicon-based sensor design which is compatible with existing CMOS fabrication technology with minimal change. In integrated photonic sensing platforms, tight optical confinement with tailorable characteristics is a primary requirement for detection. On-chip nanophotonic devices where light is confined in slot waveguide structure and this optical energy can be influenced by the presence of the sensing medium to yield a highly sensitive sensor. The introduction of silicon grating in the slot-based waveguide can enhance the sensitivity of the label-free biosensors. The waveguide grating usually composed of silicon blocks or in disk shape are arranged periodically in the direction of propagation having a period smaller than the operating wavelength. By optimizing the pitch, width and duty cycle of the grating, the effective index of the medium can be engineered.

A nanophotonic biosensing device based on a grating loaded slot waveguide is proposed with a sensitivity of 1200 nm/RIU. To increase the biocompatibility and sensitivity overlay of TiO<sub>2</sub> on silicon/air grating is adopted. The gold layer under top SiO<sub>2</sub> is used to suppress the leaky mode in the bottom cladding region. The introduction of the grating with TiO<sub>2</sub> overlay in the slot region provides a quasi-resonance in the low index region where the analyte resides which leads to strong light-analyte interaction. To improve the sensing performance a device based on Fano resonance which consists of a periodic arrangement of two rows of nano-disks and rectangular grating is proposed. The grating waveguide support low-loss optical modes that propagates in the wave-guiding region and enhances the field overlaps with analytes and suppresses reflection. The combination of nano-disk with a grating in the device has a sensitivity of 1463 nm/RIU for refractive index change of 0.02. The proposed device can detect the

refractive index change of 0.0008 in serum. The smaller footprint of Fano resonant nanostructures results in the reduction of fabrication costs. The hybrid plasmonic waveguide is proposed with a double vertical slot and a horizontal slot under a gold cover in the shape of the microchannel. This structure enables the guidance of photonic quasi-TE mode and plasmonic quasi-TM mode. The gold-clad cover increases the bulk sensitivity in TM mode by 1.5 times compared to the photonic device. The proposed device exhibits a better response with the higher change in effective refractive index for surface sensing to detect DNA hybridization, thickness variation of protein A and HBsAg antigen detection.

An optical active method for sensing, which is referred to as an optoelectronic method, is proposed to efficiently detect foodborne pathogens. A combination of slot waveguide and photocatalytic materials can prove to be an effective optoelectronic platform for biosensing applications. The proposed sensing mechanism is based on a change in photo-current originated from the photo-excited carriers, on applying a voltage, in photocatalytic nanocomposite to detect the presence of *E. coli* in Luria Bertani broth (LB) solution. A sol-gel derived photocatalytic nanocomposite CZT is used to create a slot waveguide structure for enhanced light-analyte interaction.

Label-free photocurrent biosensing platform based on ITO/CZT nanocomposite thin film has been demonstrated for the detection of *E. coli* in the buffer. At UV light irradiation, the photocurrent measurements of CZT revealed the favourable properties. A biosensor based on an optical slot waveguide made up of photocatalytic nanocomposite Cu-ZnO/TiO<sub>2</sub> (CZT) is proposed for the label-free detection of *E. coli*. The photocatalytic nature of the CZT offers electrical control over the optical characteristics of the engineered optical waveguide. The fabricated sensor, under the applied voltage of 3.5 volts, exhibits a 9  $\mu$ A change in the photocurrent in presence of *E. coli* in LB media. The photocatalytic

nanocomposite CZT is prepared and processed by a cost-effective sol-gel method and the slot is created by electron beam lithography followed by a lift-off process. The advantage of using a nanocomposite slot waveguide structure is that it provides a higher current density than thin film.

Following are the future scope of the presented work

- The nanocomposite material synthesizes by the hydrothermal process leads to the formation of nanostructures which improve the performance of the device.
- Radius and waveguide dimensions could be more rigorously optimized for finesse and exploration of more sensitive geometries with smaller analytes.
- Investigation of the polymer which combines with the nanocomposite to enhance the photocurrent.
- There is a possibility of athermal slot-waveguide refractive index sensors.
- Microfluidic channels can be designed with the devices for the proper accommodation of analyte solutions.

## REFERENCES

- [1] J. Kirsch, C. Siltanen, Q. Zhou, A. Revzin, and A. Simonian, “Biosensor technology: Recent advances in threat agent detection and medicine,” *Chemical Society Reviews*, vol. 42, no. 22, pp. 8733–8768, 2013, doi: 10.1039/c3cs60141b.
- [2] J. E. Baker, R. Sriram, and B. L. Miller, “Two-dimensional photonic crystals for sensitive microscale chemical and biochemical sensing,” *Lab on a Chip*, vol. 15, no. 4, pp. 971–990, 2015, doi: 10.1039/c4lc01208a.
- [3] B. Mizaikoff, “Waveguide-enhanced mid-infrared chem/bio sensors,” *Chemical Society Reviews*, vol. 42, no. 22, pp. 8683–8699, 2013, doi: 10.1039/c3cs60173k.
- [4] P. Rajapaksha, A. Elbourne, S. Gangadoo, R. Brown, D. Cozzolino, and J. Chapman, “A review of methods for the detection of pathogenic microorganisms,” *Analyst*, vol. 144, no. 2, pp. 396–411, 2019, doi: 10.1039/c8an01488d.
- [5] B. Stephen Inbaraj and B. H. Chen, “Nanomaterial-based sensors for detection of foodborne bacterial pathogens and toxins as well as pork adulteration in meat products,” *Journal of Food and Drug Analysis*, vol. 24, no. 1, pp. 15–28, 2016, doi: 10.1016/j.jfda.2015.05.001.
- [6] K. L. Lee, J. Bin Huang, J. W. Chang, S. H. Wu, and P. K. Wei, “Ultrasensitive biosensors using enhanced fano resonances in capped gold nanoslit arrays,” *Scientific Reports*, vol. 5, pp. 1–9, 2015, doi: 10.1038/srep08547.
- [7] T. Sun, S. Kan, G. Marriott, and C. Chang-Hasnain, “High-contrast grating resonators for label-free detection of disease

- biomarkers,” *Scientific Reports*, vol. 6, no. December 2015, pp. 1–7, 2016, doi: 10.1038/srep27482.
- [8] J. Qin *et al.*, “Fabrication of intelligent photonic crystal hydrogel sensors for selective detection of trace mercury ions in seawater,” *Journal of Materials Chemistry C*, vol. 5, no. 33, pp. 8482–8488, 2017, doi: 10.1039/c7tc02140b.
- [9] C. Danciu *et al.*, “World ’ s largest Science , Technology & Medicine Open Access book publisher New Insights Regarding the Potential Health Benefits of Isoflavones.”
- [10] C. S. Huertas, O. Calvo-Lozano, A. Mitchell, and L. M. Lechuga, “Advanced Evanescent-Wave Optical Biosensors for the Detection of Nucleic Acids: An Analytic Perspective,” *Frontiers in Chemistry*, vol. 7, no. October, pp. 1–25, 2019, doi: 10.3389/fchem.2019.00724.
- [11] P. Damborský, J. Švitel, and J. Katrlík, “Optical biosensors,” *Essays in Biochemistry*, vol. 60, no. 1, pp. 91–100, 2016, doi: 10.1042/EBC20150010.
- [12] K. Baryeh, S. Takalkar, M. Lund, and G. Liu, *Introduction to medical biosensors for point of care applications*. Elsevier Ltd, 2017.
- [13] W. W. Zhao, J. J. Xu, and H. Y. Chen, “Photoelectrochemical enzymatic biosensors,” *Biosensors and Bioelectronics*, vol. 92, no. October 2016, pp. 294–304, 2017, doi: 10.1016/j.bios.2016.11.009.
- [14] M. Pohanka, “Overview of piezoelectric biosensors, immunosensors and DNA sensors and their applications,” *Materials*, vol. 11, no. 3, 2018, doi: 10.3390/ma11030448.
- [15] V. K. T. Ngo *et al.*, “Quartz crystal microbalance (QCM) as biosensor for the detecting of *Escherichia coli* O157:H7,” *Advances in Natural Sciences: Nanoscience and*

*Nanotechnology*, vol. 5, no. 4, 2014, doi: 10.1088/2043-6262/5/4/045004.

- [16] N. Wongkaew, M. Simsek, C. Griesche, and A. J. Baeumner, “Functional Nanomaterials and Nanostructures Enhancing Electrochemical Biosensors and Lab-on-a-Chip Performances: Recent Progress, Applications, and Future Perspective,” *Chemical Reviews*, vol. 119, no. 1, pp. 120–194, Jan. 2019, doi: 10.1021/acs.chemrev.8b00172.
- [17] D. Grieshaber, R. MacKenzie, J. Vörös, and E. Reimhult, “Electrochemical biosensors - Sensor principles and architectures,” *Sensors*, vol. 8, no. 3, pp. 1400–1458, 2008, doi: 10.3390/s8031400.
- [18] Y. Zang, J. Lei, and H. Ju, “Principles and applications of photoelectrochemical sensing strategies based on biofunctionalized nanostructures,” *Biosensors and Bioelectronics*, vol. 96, no. January, pp. 8–16, 2017, doi: 10.1016/j.bios.2017.04.030.
- [19] L. Ge, Q. Liu, N. Hao, and W. Kun, “Recent developments of photoelectrochemical biosensors for food analysis,” *Journal of Materials Chemistry B*, vol. 7, no. 46, pp. 7283–7300, 2019, doi: 10.1039/c9tb01644a.
- [20] W. W. Zhao, M. Xiong, X. R. Li, J. J. Xu, and H. Y. Chen, “Photoelectrochemical bioanalysis: A mini review,” *Electrochemistry Communications*, vol. 38, pp. 40–43, 2014, doi: 10.1016/j.elecom.2013.10.035.
- [21] C. Chen and J. Wang, “Optical biosensors: An exhaustive and comprehensive review,” *Analyst*, vol. 145, no. 5, pp. 1605–1628, 2020, doi: 10.1039/c9an01998g.
- [22] L. Chrostowski *et al.*, “Silicon photonic resonator sensors and devices,” *Laser Resonators, Microresonators, and Beam*

- Control XIV*, vol. 8236, p. 823620, 2012, doi: 10.1117/12.916860.
- [23] A. Syahir, K. Usui, K. Tomizaki, K. Kajikawa, and H. Mihara, “Label and Label-Free Detection Techniques for Protein Microarrays,” *Microarrays*, vol. 4, no. 2, pp. 228–244, 2015, doi: 10.3390/microarrays4020228.
- [24] C. S. Huertas, O. Calvo-Lozano, A. Mitchell, and L. M. Lechuga, “Advanced Evanescent-Wave Optical Biosensors for the Detection of Nucleic Acids: An Analytic Perspective,” *Frontiers in Chemistry*, vol. 7. Frontiers Media S.A., Oct. 25, 2019, doi: 10.3389/fchem.2019.00724.
- [25] R. Peltomaa, B. Glahn-Martínez, E. Benito-Peña, and M. C. Moreno-Bondi, “Optical Biosensors for Label-Free Detection of Small Molecules,” *Sensors (Basel, Switzerland)*, vol. 18, no. 12. NLM (Medline), Nov. 24, 2018, doi: 10.3390/s18124126.
- [26] Z. Shen *et al.*, “A novel enzyme-linked immunosorbent assay for detection of Escherichia coli O157:H7 using immunomagnetic and beacon gold nanoparticles,” *Gut Pathogens*, vol. 6, no. 1, pp. 1–8, 2014, doi: 10.1186/1757-4749-6-14.
- [27] H. H. Nguyen, S. H. Lee, U. J. Lee, C. D. Fermin, and M. Kim, “Immobilized enzymes in biosensor applications,” *Materials*, vol. 12, no. 1, pp. 1–34, 2019, doi: 10.3390/ma12010121.
- [28] Z. Xi *et al.*, “Selection of HBsAg-specific DNA aptamers based on carboxylated magnetic nanoparticles and their application in the rapid and simple detection of hepatitis b virus infection,” *ACS Applied Materials and Interfaces*, vol. 7, no. 21, pp. 11215–11223, 2015, doi: 10.1021/acsami.5b01180.

- [29] B. Byrne, E. Stack, N. Gilmartin, and R. O’Kennedy, “Antibody-based sensors: Principles, problems and potential for detection of pathogens and associated toxins,” *Sensors (Switzerland)*, vol. 9, no. 6, pp. 4407–4445, 2009, doi: 10.3390/s90604407.
- [30] G. Roelkens *et al.*, “III-V-on-silicon photonic devices for optical communication and sensing,” *Photonics*, vol. 2, no. 3, pp. 969–1004, 2015, doi: 10.3390/photonics2030969.
- [31] R. Wang *et al.*, “III–V-on-silicon photonic integrated circuits for spectroscopic sensing in the 2–4  $\mu\text{m}$  wavelength range,” *Sensors (Switzerland)*, vol. 17, no. 8, 2017, doi: 10.3390/s17081788.
- [32] T. Baehr-Jones, M. Hochberg, and A. Scherer, “Photodetection in silicon beyond the band edge with surface states,” *Optics Express*, vol. 16, no. 3, p. 1659, 2008, doi: 10.1364/oe.16.001659.
- [33] J. Gonzalo Wangüemert-Pérez *et al.*, “Evanescent field waveguide sensing with subwavelength grating structures in silicon-on-insulator,” *Optics Letters*, vol. 39, no. 15, p. 4442, 2014, doi: 10.1364/ol.39.004442.
- [34] J. G. Wangüemert-Pérez *et al.*, “Subwavelength structures for silicon photonics biosensing,” *Optics and Laser Technology*, vol. 109, pp. 437–448, 2019, doi: 10.1016/j.optlastec.2018.07.071.
- [35] Y. Chen, J. Liu, Z. Yang, J. S. Wilkinson, and X. Zhou, “Optical biosensors based on refractometric sensing schemes: A review,” *Biosensors and Bioelectronics*, vol. 144, no. September, p. 111693, 2019, doi: 10.1016/j.bios.2019.111693.

- [36] N. Tripathy and D. H. Kim, "Metal oxide modified ZnO nanomaterials for biosensor applications," *Nano Convergence*, vol. 5, no. 1, 2018, doi: 10.1186/s40580-018-0159-9.
- [37] J. Cao, T. Sun, and K. T. V. Grattan, "Gold nanorod-based localized surface plasmon resonance biosensors: A review," *Sensors and Actuators, B: Chemical*, vol. 195. Elsevier B.V., pp. 332–351, May 01, 2014, doi: 10.1016/j.snb.2014.01.056.
- [38] R. F. Oulton, V. J. Sorger, D. A. Genov, D. F. P. Pile, and X. Zhang, "A hybrid plasmonic waveguide for subwavelength confinement and long-range propagation," *Nature Photonics*, vol. 2, no. 8, pp. 496–500, 2008, doi: 10.1038/nphoton.2008.131.
- [39] Y. Tang *et al.*, "Refractive index sensor based on fano resonances in metal-insulator-metal waveguides coupled with resonators," *Sensors (Switzerland)*, vol. 17, no. 4, 2017, doi: 10.3390/s17040784.
- [40] X. Guo, "Surface plasmon resonance based biosensor technique: A review," *Journal of Biophotonics*, vol. 5, no. 7, pp. 483–501, 2012, doi: 10.1002/jbio.201200015.
- [41] T. Claes, J. G. Molera, K. de Vos, E. Schacht, R. Baets, and P. Bienstman, "Label-free biosensing with a slot-waveguide-based ring resonator in silicon on insulator," *IEEE Photonics Journal*, vol. 1, no. 3, pp. 197–204, 2009, doi: 10.1109/JPHOT.2009.2031596.
- [42] W. R. Resonator, "On-Chip Chemical Sensing Using Slot-," vol. 20, no. 11, pp. 5970–5975, 2020.
- [43] P. Steglich *et al.*, "Hybrid-Waveguide Ring Resonator for Biochemical Sensing," *IEEE Sensors Journal*, vol. 17, no. 15, pp. 4781–4790, 2017, doi: 10.1109/JSEN.2017.2710318.

- [44] G. Gao, Y. Zhang, H. Zhang, Y. Wang, Q. Huang, and J. Xia, "Air-mode photonic crystal ring resonator on silicon-on-insulator," *Scientific Reports*, vol. 6, pp. 1–6, 2016, doi: 10.1038/srep19999.
- [45] R. Halir *et al.*, "Waveguide sub-wavelength structures: A review of principles and applications," *Laser and Photonics Reviews*, vol. 9, no. 1, pp. 25–49, 2015, doi: 10.1002/lpor.201400083.
- [46] D. M. Kita, J. Michon, S. G. Johnson, and J. Hu, "Are slot and sub-wavelength grating waveguides better than strip waveguides for sensing?," *Optica*, vol. 5, no. 9, p. 1046, 2018, doi: 10.1364/optica.5.001046.
- [47] J. G. Wangüemert-Pérez *et al.*, "Subwavelength structures for silicon photonics biosensing," *Optics and Laser Technology*, vol. 109, pp. 437–448, 2019, doi: 10.1016/j.optlastec.2018.07.071.
- [48] Q. Liu *et al.*, "Highly sensitive Mach-Zehnder interferometer biosensor based on silicon nitride slot waveguide," *Sensors and Actuators, B: Chemical*, vol. 188, pp. 681–688, 2013, doi: 10.1016/j.snb.2013.07.053.
- [49] Y. W. Baek and Y. J. An, "Microbial toxicity of metal oxide nanoparticles (CuO, NiO, ZnO, and Sb<sub>2</sub>O<sub>3</sub>) to Escherichia coli, Bacillus subtilis, and Streptococcus aureus," *Science of the Total Environment*, vol. 409, no. 8, pp. 1603–1608, 2011, doi: 10.1016/j.scitotenv.2011.01.014.
- [50] R. G. Heideman, R. P. H. Kooyman, and J. Greve, "Performance of a highly sensitive optical waveguide Mach-Zehnder interferometer immunosensor," *Sensors and Actuators: B. Chemical*, vol. 10, no. 3, pp. 209–217, Feb. 1993, doi: 10.1016/0925-4005(93)87008-D.

- [51] A. Crespi *et al.*, “Three-dimensional Mach-Zehnder interferometer in a microfluidic chip for spatially-resolved label-free detection,” *Lab on a Chip*, vol. 10, no. 9, pp. 1167–1173, 2010, doi: 10.1039/b920062b.
- [52] A. Densmore *et al.*, “Silicon photonic wire biosensor array for multiplexed real-time and label-free molecular detection,” 2009.
- [53] B. D. Malhotra and Md. A. Ali, “Nanomaterials in Biosensors,” in *Nanomaterials for Biosensors*, Elsevier, 2018, pp. 1–74.
- [54] P. R. Solanki, A. Kaushik, V. v. Agrawal, and B. D. Malhotra, “Nanostructured metal oxide-based biosensors,” *NPG Asia Materials*, vol. 3, no. 1, pp. 17–24, 2011, doi: 10.1038/asiamat.2010.137.
- [55] L. Lan, Y. Yao, J. Ping, and Y. Ying, “Recent advances in nanomaterial-based biosensors for antibiotics detection,” *Biosensors and Bioelectronics*, vol. 91, pp. 504–514, 2017, doi: <https://doi.org/10.1016/j.bios.2017.01.007>.
- [56] S. Sonawane, “Use of Nanomaterials in the Detection of Food Contaminants,” *European Journal of Nutrition & Food Safety*, vol. 4, no. 4, pp. 301–317, 2014, doi: 10.9734/ejnfs/2014/6218.
- [57] V. R. Almeida, Q. Xu, C. A. Barrios, and M. Lipson, “Guiding and confining light in void nanostructure,” *Optics Letters*, vol. 29, no. 11, p. 1209, 2004, doi: 10.1364/ol.29.001209.
- [58] C. A. Barrios *et al.*, “Label-free optical biosensing with slot-waveguides,” *Optics Letters*, vol. 33, no. 7, p. 708, 2008, doi: 10.1364/ol.33.000708.
- [59] F. Dell’Olio and V. M. Passaro, “Optical sensing by optimized silicon slot waveguides,” *Optics Express*, vol. 15, no. 8, p. 4977, 2007, doi: 10.1364/oe.15.004977.

- [60] F. Qiu *et al.*, “A hybrid electro-optic polymer and TiO<sub>2</sub> double-slot waveguide modulator,” *Scientific Reports*, vol. 5, pp. 1–6, 2015, doi: 10.1038/srep08561.
- [61] R. Sun *et al.*, “Horizontal single and multiple slot waveguides: optical transmission at  $\lambda = 1550$  nm,” *Optics Express*, vol. 15, no. 26, p. 17967, 2007, doi: 10.1364/oe.15.017967.
- [62] D. Ozelik, H. Cai, K. D. Leake, A. R. Hawkins, and H. Schmidt, “Optofluidic bioanalysis: Fundamentals and applications,” *Nanophotonics*, vol. 6, no. 4, pp. 647–661, 2017, doi: 10.1515/nanoph-2016-0156.
- [63] K. Han *et al.*, “Strip-slot direct mode coupler,” *Optics Express*, vol. 24, no. 6, p. 6532, 2016, doi: 10.1364/oe.24.006532.
- [64] C. C. Huang and C. C. Huang, “Ultra-compact and high-performance polarization beam splitter assisted by slotted waveguide subwavelength gratings,” *Scientific Reports*, vol. 10, no. 1, pp. 1–10, 2020, doi: 10.1038/s41598-020-69749-7.
- [65] T. Lin, X. Zhang, G. Zhou, C. F. Siong, and J. Deng, “Design of an ultra-compact slotted photonic crystal nanobeam cavity for biosensing,” *Journal of the Optical Society of America B*, vol. 32, no. 9, p. 1788, 2015, doi: 10.1364/josab.32.001788.
- [66] A. Kargar and C.-Y. Chao, “Design and optimization of waveguide sensitivity in slot microring sensors,” *Journal of the Optical Society of America A*, vol. 28, no. 4, p. 596, 2011, doi: 10.1364/josaa.28.000596.
- [67] I. Khodadad, N. Clarke, M. Khorasaninejad, D. Henneke, and S. S. Saini, “Optimization of multiple-slot waveguides for biochemical sensing,” *Applied Optics*, vol. 53, no. 23, p. 5169, 2014, doi: 10.1364/ao.53.005169.

- [68] G. Yuan, L. Gao, Y. Chen, X. Liu, J. Wang, and Z. Wang, "Improvement of optical sensing performances of a double-slot-waveguide- based ring resonator sensor on silicon-on-insulator platform," *Optik*, vol. 125, no. 2, pp. 850–854, Jan. 2014, doi: 10.1016/j.ijleo.2013.07.088.
- [69] Y. Ishizaka, S. Makino, T. Fujisawa, and K. Saitoh, "A metal-assisted silicon slot waveguide for highly sensitive gas detection," *IEEE Photonics Journal*, vol. 9, no. 1, Feb. 2017, doi: 10.1109/JPHOT.2016.2630308.
- [70] X. Wang *et al.*, "A silicon photonic biosensor using phase-shifted Bragg gratings in slot waveguide," *Journal of Biophotonics*, vol. 6, no. 10, pp. 821–828, 2013, doi: 10.1002/jbio.201300012.
- [71] J. G. Wangüemert-Pérez *et al.*, "Subwavelength structures for silicon photonics biosensing," *Optics and Laser Technology*, vol. 109, pp. 437–448, Jan. 2019, doi: 10.1016/j.optlastec.2018.07.071.
- [72] Í. Molina-Fernández, J. Leuermann, A. Ortega-Moñux, J. G. Wangüemert-Pérez, and R. Halir, "Fundamental limit of detection of photonic biosensors with coherent phase read-out," *Optics Express*, vol. 27, no. 9, p. 12616, 2019, doi: 10.1364/oe.27.012616.
- [73] Z. Wang, X. Xu, D. Fan, Y. Wang, and R. T. Chen, "High quality factor subwavelength grating waveguide micro-ring resonator based on trapezoidal silicon pillars," *Opt. Lett.*, vol. 41, no. 14, pp. 3375–3378, Jul. 2016, doi: 10.1364/OL.41.003375.
- [74] H. Yan *et al.*, "Unique surface sensing property and enhanced sensitivity in microring resonator biosensors based on subwavelength grating waveguides," *Optics Express*, vol. 24, no. 26, p. 29724, 2016, doi: 10.1364/oe.24.029724.

- [75] V. Donzella, A. Sherwali, J. Flueckiger, S. Talebi Fard, S. M. Grist, and L. Chrostowski, "Sub-wavelength grating components for integrated optics applications on SOI chips," *Optics Express*, vol. 22, no. 17, p. 21037, Aug. 2014, doi: 10.1364/oe.22.021037.
- [76] J. Flueckiger *et al.*, "Sub-wavelength grating for enhanced ring resonator biosensor," *Optics Express*, vol. 24, no. 14, p. 15672, 2016, doi: 10.1364/oe.24.015672.
- [77] E. Luan, H. Yun, M. Ma, D. M. Ratner, K. C. Cheung, and L. Chrostowski, "Label-free biosensing with a multi-box sub-wavelength phase-shifted Bragg grating waveguide," *Biomedical Optics Express*, vol. 10, no. 9, p. 4825, Sep. 2019, doi: 10.1364/boe.10.004825.
- [78] V. Donzella, A. Sherwali, J. Flueckiger, S. M. Grist, S. T. Fard, and L. Chrostowski, "Design and fabrication of SOI micro-ring resonators based on sub-wavelength grating waveguides," *Optics Express*, vol. 23, no. 4, p. 4791, Feb. 2015, doi: 10.1364/oe.23.004791.
- [79] Z. Ruan, L. Shen, S. Zheng, and J. Wang, "Subwavelength grating slot (SWGS) waveguide on silicon platform," *Optics Express*, vol. 25, no. 15, p. 18250, Jul. 2017, doi: 10.1364/oe.25.018250.
- [80] J. Milvich, D. Kohler, W. Freude, and C. Koos, "Surface sensing with integrated optical waveguides: a design guideline," *Optics Express*, vol. 26, no. 16, p. 19885, 2018, doi: 10.1364/oe.26.019885.
- [81] H. Fan and P. Berini, "Bulk Sensing Using a Long-Range Surface-Plasmon Dual-Output Mach-Zehnder Interferometer," *Journal of Lightwave Technology*, vol. 34, no. 11, pp. 2631–2638, 2016, doi: 10.1109/JLT.2016.2543138.

- [82] P. Berini, “Bulk and surface sensitivities of surface Plasmon waveguides,” *New Journal of Physics*, vol. 10, 2008, doi: 10.1088/1367-2630/10/10/105010.
- [83] S. Grandi *et al.*, “Hybrid plasmonic waveguide coupling of photons from a single molecule,” *APL Photonics*, vol. 4, no. 8, 2019, doi: 10.1063/1.5110275.
- [84] X. Sun, D. Dai, L. Thylén, and L. Wosinski, “High-sensitivity liquid refractive-index sensor based on a Mach-Zehnder interferometer with a double-slot hybrid plasmonic waveguide,” *Optics Express*, vol. 23, no. 20, p. 25688, 2015, doi: 10.1364/oe.23.025688.
- [85] H. Okamoto, S. Kamada, M. Haraguchi, and T. Okamoto, “Design of a hybrid plasmonic waveguide device using a trench structure,” *Journal of Physics Communications*, vol. 4, no. 9, pp. 1–8, 2020, doi: 10.1088/2399-6528/abb985.
- [86] C. Chen, X. Hou, and J. Si, “Protein analysis by Mach-Zehnder interferometers with a hybrid plasmonic waveguide with nano-slots,” *Optics Express*, vol. 25, no. 25, p. 31294, 2017, doi: 10.1364/oe.25.031294.
- [87] X. Sun, L. Thylén, and L. Wosinski, “Hollow hybrid plasmonic Mach–Zehnder sensor,” *Optics Letters*, vol. 42, no. 4, p. 807, 2017, doi: 10.1364/ol.42.000807.
- [88] M. Z. Alam, F. Bahrami, J. S. Aitchison, and M. Mojahedi, “Analysis and optimization of hybrid plasmonic waveguide as a platform for biosensing,” *IEEE Photonics Journal*, vol. 6, no. 4, 2014, doi: 10.1109/JPHOT.2014.2331232.
- [89] X. Sun, D. Dai, L. Thylén, and L. Wosinski, “High-sensitivity liquid refractive-index sensor based on a Mach-Zehnder interferometer with a double-slot hybrid plasmonic waveguide,”

- Optics Express*, vol. 23, no. 20, p. 25688, 2015, doi: 10.1364/oe.23.025688.
- [90] M. A. Butt, S. N. Khonina, and N. L. Kazanskiy, “Highly sensitive refractive index sensor based on hybrid plasmonic waveguide microring resonator,” *Waves in Random and Complex Media*, vol. 30, no. 2, pp. 292–299, Apr. 2020, doi: 10.1080/17455030.2018.1506191.
- [91] M. F. O. Hameed, A. S. Saadeldin, E. M. A. Elkaramany, and S. S. A. Obayya, “Label-Free Highly Sensitive Hybrid Plasmonic Biosensor for the Detection of DNA Hybridization,” *Journal of Lightwave Technology*, vol. 35, no. 22, pp. 4851–4858, 2017, doi: 10.1109/JLT.2017.2733720.
- [92] C. Chen, X. Hou, and J. Si, “Protein analysis by Mach-Zehnder interferometers with a hybrid plasmonic waveguide with nano-slots,” *Optics Express*, vol. 25, no. 25, p. 31294, 2017, doi: 10.1364/oe.25.031294.
- [93] E. Chatzianagnostou *et al.*, “Scaling the Sensitivity of Integrated Plasm-Photonic Interferometric Sensors,” *ACS Photonics*, vol. 6, no. 7, pp. 1664–1673, 2019, doi: 10.1021/acsp Photonics.8b01683.
- [94] Y. Zhang *et al.*, “High-quality-factor multiple Fano resonances for refractive index sensing,” *Optics Letters*, vol. 43, no. 8, p. 1842, 2018, doi: 10.1364/ol.43.001842.
- [95] M. F. Limonov, M. V Rybin, A. N. Poddubny, and Y. S. Kivshar, “Fano resonances in photonics,” *Nature Publishing Group*, vol. 11, no. 9, pp. 543–554, 2017, doi: 10.1038/nphoton.2017.142.
- [96] C. Zheng *et al.*, “RSC Advances Theoretical study on narrow Fano resonance of nanocrescent for the label-free detection of

- single molecules and single nanoparticles,” *RSC Advances*, vol. 8, pp. 3381–3391, 2018, doi: 10.1039/C7RA12666B.
- [97] “Double-layer Fano resonance photonic-crystal- slab-based sensor for label-free detection of different size analytes,” vol. 36, no. 2, pp. 215–222, 2019.
- [98] J. N. Anker, W. P. Hall, O. Lyandres, N. C. Shah, J. Zhao, and R. P. Van Duyne, “Biosensing with plasmonic nanosensors,” *Nanoscience and Technology: A Collection of Reviews from Nature Journals*, vol. 7, no. June, pp. 308–319, 2009, doi: 10.1142/9789814287005\_0032.
- [99] F. Hao, Y. Sonnefraud, P. Van Dorpe, S. A. Maier, N. J. Halas, and P. Nordlander, “Symmetry breaking in plasmonic nanocavities: Subradiant LSPR sensing and a tunable Fano resonance,” *Nano Letters*, vol. 8, no. 11, pp. 3983–3988, 2008, doi: 10.1021/nl802509r.
- [100] D. J. Cai *et al.*, “Fano resonances generated in a single dielectric homogeneous nanoparticle with high structural symmetry,” *Journal of Physical Chemistry C*, vol. 119, no. 8, pp. 4252–4260, 2015, doi: 10.1021/jp512003b.
- [101] M. F. Limonov, M. V Rybin, A. N. Poddubny, and Y. S. Kivshar, “Fano resonances in photonics,” *Nature Publishing Group*, vol. 11, no. 9, pp. 543–554, 2017, doi: 10.1038/nphoton.2017.142.
- [102] C. Blanchard, J. P. Hugonin, and C. Sauvan, “Fano resonances in photonic crystal slabs near optical bound states in the continuum,” *Physical Review B*, vol. 94, no. 15, pp. 1–9, 2016, doi: 10.1103/PhysRevB.94.155303.
- [103] W. Wang *et al.*, “Broken symmetry theta-shaped dielectric arrays for a high Q-factor Fano resonance with anapole

excitation and magnetic field tunability,” *OSA Continuum*, vol. 2, no. 2, p. 507, 2019, doi: 10.1364/osac.2.000507.

- [104] B. Luk’Yanchuk *et al.*, “The Fano resonance in plasmonic nanostructures and metamaterials,” *Nature Materials*, vol. 9, no. 9, pp. 707–715, 2010, doi: 10.1038/nmat2810.
- [105] Y. Yang, I. I. Kravchenko, D. P. Briggs, and J. Valentine, “All-dielectric metasurface analogue of electromagnetically induced transparency,” *Nature Communications*, vol. 5, 2014, doi: 10.1038/ncomms6753.
- [106] Y. Yang, I. I. Kravchenko, D. P. Briggs, and J. Valentine, “All-dielectric metasurface analogue of electromagnetically induced transparency,” *Nature Communications*, vol. 5, pp. 1–7, 2014, doi: 10.1038/ncomms6753.
- [107] Y. Zhang *et al.*, “High-quality-factor multiple Fano resonances for refractive index sensing,” *Optics Letters*, vol. 43, no. 8, p. 1842, Apr. 2018, doi: 10.1364/ol.43.001842.
- [108] X. Zhang, Y. Qi, P. Zhou, H. Gong, B. Hu, and C. Yan, “Refractive Index Sensor Based on Fano Resonances in Plasmonic Waveguide With Dual Side-Coupled Ring Resonators,” vol. 8, no. 4, pp. 367–374, 2018, doi: 10.1007/s13320-018-0509-6.
- [109] C. Wu *et al.*, “Spectrally selective chiral silicon metasurfaces based on infrared Fano resonances,” *Nature Communications*, vol. 5, no. May, pp. 1–9, 2014, doi: 10.1038/ncomms4892.
- [110] W. Zhao, X. Leng, and Y. Jiang, “with efficient linewidth tuning Fano resonance in all-dielectric binary nanodisk array realizing optical filter with efficient linewidth tuning,” no. October 2018, 2015, doi: 10.1364/OE.23.006858.
- [111] K. E. Chong *et al.*, “Refractive index sensing with Fano resonances in silicon oligomers Subject Areas :,” 2017.

- [112] M. G. Valdés, A. C. V. González, J. A. G. Calzón, and M. E. Díaz-García, “Analytical nanotechnology for food analysis,” *Microchimica Acta*, vol. 166, no. 1–2, pp. 1–19, 2009, doi: 10.1007/s00604-009-0165-z.
- [113] P. Pashazadeh, A. Mokhtarzadeh, M. Hasanzadeh, M. Hejazi, M. Hashemi, and M. de la Guardia, “Nano-materials for use in sensing of salmonella infections: Recent advances,” *Biosensors and Bioelectronics*, vol. 87, pp. 1050–1064, 2017, doi: 10.1016/j.bios.2016.08.012.
- [114] P. J. Vikesland and K. R. Wigginton, “Nanomaterial enabled biosensors for pathogen monitoring - A review,” *Environmental Science and Technology*, vol. 44, no. 10, pp. 3656–3669, May 15, 2010, doi: 10.1021/es903704z.
- [115] F. C. Dudak and I. H. Boyaci, “Rapid and label-free bacteria detection by surface plasmon resonance (SPR) biosensors,” *Biotechnology Journal*, vol. 4, no. 7, pp. 1003–1011, 2009, doi: 10.1002/biot.200800316.
- [116] S. Jain, “Development of an Antibody Functionalized Carbon Nanotube Biosensor for Foodborne Bacterial Pathogens,” *Journal of Biosensors & Bioelectronics*, vol. 01, no. S11, 2012, doi: 10.4172/2155-6210.s11-002.
- [117] J. Joo *et al.*, “A facile and sensitive detection of pathogenic bacteria using magnetic nanoparticles and optical nanocrystal probes,” *Analyst*, vol. 137, no. 16, pp. 3609–3612, 2012, doi: 10.1039/C2AN35369E.
- [118] F. Chen, J. Zhou, F. Luo, A.-B. Mohammed, and X.-L. Zhang, “Aptamer from whole-bacterium SELEX as new therapeutic reagent against virulent *Mycobacterium tuberculosis*,” *Biochemical and Biophysical Research Communications*, vol. 357, no. 3, pp. 743–748, 2007, doi: <https://doi.org/10.1016/j.bbrc.2007.04.007>.

- [119] C. García-Aljaro *et al.*, “Carbon nanotubes-based chemiresistive biosensors for detection of microorganisms,” *Biosensors & bioelectronics*, vol. 26, no. 4, p. 1437–1441, Dec. 2010, doi: 10.1016/j.bios.2010.07.077.
- [120] Y. Teng *et al.*, “Optimized ferrocene-functionalized ZnO nanorods for signal amplification in electrochemical immunoassay of *Escherichia coli*,” *Biosensors & bioelectronics*, vol. 26, no. 12, p. 4661–4666, Aug. 2011, doi: 10.1016/j.bios.2011.04.017.
- [121] K. Y. Chan *et al.*, “Ultrasensitive detection of *E. coli* O157:H7 with biofunctional magnetic bead concentration via nanoporous membrane based electrochemical immunosensor,” *Biosensors and Bioelectronics*, vol. 41, pp. 532–537, 2013, doi: <https://doi.org/10.1016/j.bios.2012.09.016>.
- [122] N. Massad-Ivanir, G. Shtenberg, A. Tzur, M. A. Krepker, and E. Segal, “Engineering nanostructured porous SiO<sub>2</sub> surfaces for bacteria detection via ‘direct cell capture,’” *Analytical Chemistry*, vol. 83, no. 9, pp. 3282–3289, 2011, doi: 10.1021/ac200407w.
- [123] S. Tokonami *et al.*, “Label-free and selective bacteria detection using a film with transferred bacterial configuration,” *Analytical Chemistry*, vol. 85, no. 10, pp. 4925–4929, 2013, doi: 10.1021/ac3034618.
- [124] R. Narang *et al.*, “Sensitive, Real-time and Non-Intrusive Detection of Concentration and Growth of Pathogenic Bacteria using Microfluidic-Microwave Ring Resonator Biosensor,” *Scientific Reports*, vol. 8, no. 1, pp. 1–10, 2018, doi: 10.1038/s41598-018-34001-w.
- [125] Z. Wang, X. Xu, D. Fan, Y. Wang, H. Subbaraman, and R. T. Chen, “Geometrical tuning art for entirely subwavelength

- grating waveguide based integrated photonics circuits,” *Scientific Reports*, vol. 6, May 2016, doi: 10.1038/srep24106.
- [126] A. A. Siraji and Y. Zhao, “High-sensitivity and high-Q-factor glass photonic crystal cavity and its applications as sensors,” *Opt. Lett.*, vol. 40, no. 7, pp. 1508–1511, Apr. 2015, doi: 10.1364/OL.40.001508.
- [127] J.-N. Yih *et al.*, “Optical waveguide biosensors constructed with subwavelength gratings,” *Appl. Opt.*, vol. 45, no. 9, pp. 1938–1942, Mar. 2006, doi: 10.1364/AO.45.001938.
- [128] R. Méjard, H. J. Griesser, and B. Thierry, “Optical biosensing for label-free cellular studies,” *TrAC - Trends in Analytical Chemistry*, vol. 53. Elsevier B.V., pp. 178–186, Jan. 01, 2014, doi: 10.1016/j.trac.2013.08.012.
- [129] M. Cooper, “Signal transduction profiling using label-free biosensors,” *Journal of Receptors and Signal Transduction*, vol. 29, pp. 224–233, 2009.
- [130] S. E. McBirney, D. Chen, A. Scholtz, H. Ameri, and A. M. Armani, “Rapid Diagnostic for Point-of-Care Malaria Screening,” *ACS Sensors*, vol. 3, no. 7, pp. 1264–1270, May 2018, doi: 10.1021/acssensors.8b00269.
- [131] Y. S. Hong, C. H. Cho, and H. K. Sung, “Design parameter optimization of a silicon-based grating waveguide for performance improvement in biochemical sensor application,” *Sensors (Switzerland)*, vol. 18, no. 3, Mar. 2018, doi: 10.3390/s18030781.
- [132] M. S. Luchansky and R. C. Bailey, “High-Q Optical Sensors for Chemical and Biological Analysis,” *Analytical Chemistry*, vol. 84, no. 2, pp. 793–821, Nov. 2011, doi: 10.1021/ac2029024.

- [133] W. Zhang and J. Yao, “A fully reconfigurable waveguide Bragg grating for programmable photonic signal processing,” *Nature Communications*, vol. 9, no. 1, Dec. 2018, doi: 10.1038/s41467-018-03738-3.
- [134] S. Yan, M. Zhang, X. Zhao, Y. Zhang, J. Wang, and W. Jin, “Refractive index sensor based on a metal–insulator–metal waveguide coupled with a symmetric structure,” *Sensors (Switzerland)*, vol. 17, no. 12, Dec. 2017, doi: 10.3390/s17122879.
- [135] J. Xavier, S. Vincent, F. Meder, and F. Vollmer, “Advances in optoplasmonic sensors - Combining optical nano/microcavities and photonic crystals with plasmonic nanostructures and nanoparticles,” *Nanophotonics*, vol. 7, no. 1. Walter de Gruyter GmbH, pp. 1–38, Jan. 01, 2018, doi: 10.1515/nanoph-2017-0064.
- [136] Y. Li, X. Tao, H. Chen, and W. Y. Tam, “Q-factor enhancement in a one-dimensional photonic crystal cavity with embedded planar plasmonic metamaterials,” *J. Opt. Soc. Am. A*, vol. 28, no. 3, pp. 314–317, Mar. 2011, doi: 10.1364/JOSAA.28.000314.
- [137] Y. S. Hong, J. Kim, and H. K. Sung, “Characterization of a functional hydrogel layer on a silicon-based gratingwaveguide for a biochemical sensor,” *Sensors (Switzerland)*, vol. 16, no. 6, Jun. 2016, doi: 10.3390/s16060914.
- [138] M. S. Diware *et al.*, “Label-free detection of hepatitis B virus using solution immersed silicon sensors,” *Biointerphases*, vol. 12, no. 1, p. 01A402, 2017, doi: 10.1116/1.4977075.
- [139] V. M. N. Passaro, F. Dell’Olio, C. Ciminelli, and M. N. Armenise, “Efficient chemical sensing by coupled slot SOI waveguides,” *Sensors*, vol. 9, no. 2, pp. 1012–1032, Feb. 2009, doi: 10.3390/s90201012.

- [140] R. Ge, J. Xie, B. Yan, E. Liu, W. Tan, and J. Liu, "Refractive index sensor with high sensitivity based on circular photonic crystal," *J. Opt. Soc. Am. A*, vol. 35, no. 6, pp. 992–997, Jun. 2018, doi: 10.1364/JOSAA.35.000992.
- [141] T. Li, Z. Wang, D. Gao, and X. Zhang, "High Q one-dimensional photonic crystal slot nanobeam cavity for high-sensitivity refractive index sensing," in *2015 Opto-Electronics and Communications Conference (OECC)*, 2015, pp. 1–3, doi: 10.1109/OECC.2015.7340282.
- [142] E. Luan, H. Shoman, D. M. Ratner, K. C. Cheung, and L. Chrostowski, "Silicon photonic biosensors using label-free detection," *Sensors (Switzerland)*, vol. 18, no. 10. MDPI AG, Oct. 18, 2018, doi: 10.3390/s18103519.
- [143] Z. Zhang *et al.*, "Plasmonic refractive index sensor with high figure of merit based on concentric-rings resonator," *Sensors (Switzerland)*, vol. 18, no. 1, Jan. 2018, doi: 10.3390/s18010116.
- [144] Y. Feng, Y. Liu, and J. Teng, "Design of an ultrasensitive SPR biosensor based on a graphene-MoS<sub>2</sub> hybrid structure with a MgF<sub>2</sub> prism," *Appl. Opt.*, vol. 57, no. 14, pp. 3639–3644, May 2018, doi: 10.1364/AO.57.003639.
- [145] M. F. Limonov, M. v. Rybin, A. N. Poddubny, and Y. S. Kivshar, "Fano resonances in photonics," *Nature Photonics*, vol. 11, no. 9, pp. 543–554, Sep. 2017, doi: 10.1038/NPHOTON.2017.142.
- [146] D. J. Cai *et al.*, "Fano resonances generated in a single dielectric homogeneous nanoparticle with high structural symmetry," *Journal of Physical Chemistry C*, vol. 119, no. 8, pp. 4252–4260, Feb. 2015, doi: 10.1021/jp512003b.

- [147] I. Staude *et al.*, “Tailoring directional scattering through magnetic and electric resonances in subwavelength silicon nanodisks,” *ACS Nano*, vol. 7, no. 9, pp. 7824–7832, 2013, doi: 10.1021/nm402736f.
- [148] F. Dell’Olio and V. M. Passaro, “Optical sensing by optimized silicon slot waveguides,” *Optics Express*, vol. 15, no. 8, p. 4977, 2007, doi: 10.1364/oe.15.004977.
- [149] Z. Ruan *et al.*, “Subwavelength grating slot ( SWGS ) waveguide at 2  $\mu$  m for chip-scale data transmission,” vol. 7, no. 5, pp. 865–871, 2018.
- [150] L. Torrijos-Morán and J. García-Rupérez, “Single-channel bimodal interferometric sensor using subwavelength structures,” *Optics Express*, vol. 27, no. 6, p. 8168, 2019, doi: 10.1364/oe.27.008168.
- [151] W. H. Gerlich, U. Wend, and D. Glebe, “Quantitative Assay of Hepatitis B Surface Antigen in Serum or Plasma Using Laurell Electrophoresis,” vol. 95, pp. 57–63.
- [152] M. G. Hossain and K. Ueda, “Investigation of a novel hepatitis B virus surface antigen (HBsAg) escape mutant affecting immunogenicity,” *PLoS ONE*, vol. 12, no. 1, pp. 1–22, 2017, doi: 10.1371/journal.pone.0167871.
- [153] E. Reuschel, W. Jilg, B. Seelbach-Goebel, and L. Deml, “Comparative purification and characterization of hepatitis B virus-like particles produced by recombinant vaccinia viruses in human hepatoma cells and human primary hepatocytes,” *PLoS ONE*, vol. 14, no. 2, pp. 1–18, 2019, doi: 10.1371/journal.pone.0212800.
- [154] J. Hänisch, K. Hinrichs, and J. Rappich, “Surface Functionalization toward Biosensing via Free-Standing Si-OH Bonds on Nonoxidized Silicon Surfaces,” *ACS Applied*

- Materials and Interfaces*, vol. 11, no. 34, pp. 31434–31440, 2019, doi: 10.1021/acsami.9b03583.
- [155] S. Schmidt *et al.*, “Improving the performance of silicon photonic rings, disks, and Bragg gratings for use in label-free biosensing,” *Biosensing and Nanomedicine VII*, vol. 9166, p. 91660M, 2014, doi: 10.1117/12.2062389.
- [156] S. Rajput, V. Kaushik, S. Jain, and M. Kumar, “Slow light enhanced phase shifter based on low-loss silicon-ITO hollow waveguide,” *IEEE Photonics Journal*, vol. 11, no. 1, pp. 1–8, 2019, doi: 10.1109/JPHOT.2019.2895699.
- [157] S. Liu, Z. Deng, J. Li, J. Wang, and N. Huang, “Measurement of the refractive index of whole blood and its components for a continuous spectral region,” *Journal of Biomedical Optics*, vol. 24, no. 03, p. 1, 2019, doi: 10.1117/1.jbo.24.3.035003.
- [158] B. Negahdari, M. Darvishi, and A. A. Saeedi, “Gold nanoparticles and hepatitis B virus,” *Artificial Cells, Nanomedicine and Biotechnology*, vol. 47, no. 1, pp. 469–474, 2019, doi: 10.1080/21691401.2018.1546185.
- [159] E. N. L. Uan *et al.*, “Label-free biosensing with a multi-box sub-wavelength phase-shifted Bragg grating waveguide,” vol. 10, no. 9, pp. 4825–4838, 2019.
- [160] Z. T. U. Hengrui, D. I. G. Ao, M. E. Z. Hang, and D. A. Z. Hang, “High-sensitivity complex refractive index sensing based on Fano resonance in the subwavelength grating waveguide micro-ring resonator,” vol. 25, no. 17, pp. 20911–20922, 2017.
- [161] E. Lazareva and V. Tuchin, “Blood refractive index modelling in the visible and near infrared spectral regions,” *Journal of Biomedical Photonics & Engineering*, vol. 4, no. 1, p. 010503, 2018, doi: 10.18287/jbpe18.04.010503.

- [162] A. B. J. Groeneveld, “Albumin and artificial colloids in fluid management: Where does the clinical evidence of their utility stand?,” *Critical Care*, vol. 4, no. SUPPL. 2, 2000, doi: 10.1186/cc965.
- [163] T. T. Niemi, R. Miyashita, and M. Yamakage, “Colloid solutions: A clinical update,” *Journal of Anesthesia*, vol. 24, no. 6, pp. 913–925, 2010, doi: 10.1007/s00540-010-1034-y.
- [164] X. Xu, R. K. Wang, J. B. Elder, and V. V. Tuchin, “Effect of dextran-induced changes in refractive index and aggregation on optical properties of whole blood,” *Physics in Medicine and Biology*, vol. 48, no. 9, pp. 1205–1221, 2003, doi: 10.1088/0031-9155/48/9/309.
- [165] E. PONDER and R. V. PONDER, “The interaction of dextran with serum albumin, gamma globulin, and fibrinogen.,” *The Journal of general physiology*, vol. 43, no. 1955, pp. 753–758, 1960, doi: 10.1085/jgp.43.4.753.
- [166] S. Rajput, V. Kaushik, S. Jain, P. Tiwari, A. K. Srivastava, and M. Kumar, “Optical Modulation in Hybrid Waveguide Based on Si-ITO Heterojunction,” *Journal of Lightwave Technology*, vol. 38, no. 6, pp. 1365–1371, Mar. 2020, doi: 10.1109/JLT.2019.2953690.
- [167] Q. Xiang, J. Huang, H. Huang, W. Mao, and Z. Ye, “A label-free electrochemical platform for the highly sensitive detection of hepatitis B virus DNA using graphene quantum dots,” *RSC Advances*, vol. 8, no. 4, pp. 1820–1825, 2018, doi: 10.1039/c7ra11945c.
- [168] X. Wang *et al.*, “Gold nanorod-based localized surface plasmon resonance biosensor for sensitive detection of hepatitis B virus in buffer, blood serum and plasma,” *Biosensors and Bioelectronics*, vol. 26, no. 2, pp. 404–410, 2010, doi: 10.1016/j.bios.2010.07.121.

- [169] D. Yang *et al.*, “High sensitivity and high Q -factor nanoslot parallel quadrabeam photonic crystal cavity for real-time and label-free sensing,” *Applied Physics Letters*, vol. 105, no. 6, 2014, doi: 10.1063/1.4867254.
- [170] J. Milvich, D. Kohler, W. Freude, and C. Koos, “Surface sensing with integrated optical waveguides: a design guideline,” *Optics Express*, vol. 26, no. 16, p. 19885, 2018, doi: 10.1364/oe.26.019885.
- [171] H. Sun, A. Chen, and L. R. Dalton, “Enhanced evanescent confinement in multiple-slot waveguides and its application in biochemical sensing,” *IEEE Photonics Journal*, vol. 1, no. 1, pp. 48–57, 2009, doi: 10.1109/JPHOT.2009.2025602.
- [172] V. T. Hoang, G. Stępniewski, K. H. Czarnecka, and R. Kasztelanica, “Optical Properties of Buffers and Cell Culture Media for Optofluidic and Sensing Applications,” pp. 1–11, doi: 10.3390/app9061145.
- [173] T. H. Talukdar, G. D. Allen, I. Kravchenko, and J. D. Ryckman, “Single-mode porous silicon waveguide interferometers with unity confinement factors for ultra-sensitive surface adlayer sensing,” *Optics Express*, vol. 27, no. 16, p. 22485, 2019, doi: 10.1364/oe.27.022485.
- [174] J. Tang, Y. Huang, Y. Cheng, L. Huang, J. Zhuang, and D. Tang, “Two-dimensional MoS<sub>2</sub> as a nano-binder for ssDNA: Ultrasensitive aptamer based amperometric detection of Ochratoxin A,” *Microchimica Acta*, vol. 185, no. 3, pp. 1–8, 2018, doi: 10.1007/s00604-018-2706-9.
- [175] T. Dar, J. Homola, B. M. A. Rahman, and M. Rajarajan, “Label-free slot-waveguide biosensor for the detection of DNA hybridization,” *Applied Optics*, vol. 51, no. 34, pp. 8195–8202, 2012, doi: 10.1364/AO.51.008195.

- [176] C. Viphavakit, M. Komodromos, C. Themistos, W. S. Mohammed, K. Kalli, and B. M. Azizur Rahman, "Optimization of a horizontal slot waveguide biosensor to detect DNA hybridization," *Applied Optics*, vol. 54, no. 15, p. 4881, 2015, doi: 10.1364/ao.54.004881.
- [177] P. Kannan, P. Subramanian, T. Maiyalagan, and Z. Jiang, "Cobalt Oxide Porous Nanocubes-Based Electrochemical Immunobiosensing of Hepatitis B Virus DNA in Blood Serum and Urine Samples," *Analytical Chemistry*, vol. 91, no. 9, pp. 5824–5833, 2019, doi: 10.1021/acs.analchem.9b00153.
- [178] Y. Sato, N. Ishikawa, and T. Takagi, "High-performance size-exclusion chromatography and molar mass measurement of low-angle laser light scattering of recombinant yeast-derived human hepatitis B virus surface antigen vaccine particles," *Journal of Chromatography A*, vol. 507, no. C, pp. 25–31, 1990, doi: 10.1016/S0021-9673(01)84177-7.
- [179] R. S. Burlage and J. Tillmann, "Biosensors of bacterial cells," *Journal of Microbiological Methods*, vol. 138, pp. 2–11, 2017, doi: 10.1016/j.mimet.2016.12.023.
- [180] M. B. Maas, W. J. Perold, and L. M. T. Dicks, "Biosensors for the detection of escherichia coli," *Water SA*, vol. 43, no. 4, pp. 707–721, 2017, doi: 10.4314/wsa.v43i4.17.
- [181] Y. Cheng *et al.*, "Combining biofunctional magnetic nanoparticles and ATP bioluminescence for rapid detection of Escherichia coli," *Talanta*, vol. 77, no. 4, pp. 1332–1336, 2009, doi: 10.1016/j.talanta.2008.09.014.
- [182] B. Ge, S. Zhao, R. Hall, and J. Meng, "A PCR-ELISA for detecting Shiga toxin-producing Escherichia coli," *Microbes and Infection*, vol. 4, no. 3, pp. 285–290, 2002, doi: 10.1016/S1286-4579(02)01540-X.

- [183] A. Ahmed, J. V. Rushworth, N. A. Hirst, and P. A. Millner, “Biosensors for whole-cell bacterial detection,” *Clinical Microbiology Reviews*, vol. 27, no. 3, pp. 631–646, 2014, doi: 10.1128/CMR.00120-13.
- [184] S. Y. Wu, J. Hulme, and S. S. A. An, “Recent trends in the detection of pathogenic *Escherichia coli* O157:H7,” *Biochip Journal*, vol. 9, no. 3, pp. 173–181, 2015, doi: 10.1007/s13206-015-9208-9.
- [185] O. Lazcka, F. J. Del Campo, and F. X. Muñoz, “Pathogen detection: A perspective of traditional methods and biosensors,” *Biosensors and Bioelectronics*, vol. 22, no. 7, pp. 1205–1217, 2007, doi: 10.1016/j.bios.2006.06.036.
- [186] J. Chen *et al.*, “Electrochemical nanoparticle-enzyme sensors for screening bacterial contamination in drinking water,” *Analyst*, vol. 140, no. 15, pp. 4991–4996, 2015, doi: 10.1039/c5an00637f.
- [187] N. Dhull *et al.*, “Label-free amperometric biosensor for *Escherichia coli* O157:H7 detection,” *Applied Surface Science*, vol. 495, no. July, 2019, doi: 10.1016/j.apsusc.2019.143548.
- [188] S. Qiu *et al.*, “Highly selective colorimetric bacteria sensing based on protein-capped nanoparticles,” *Analyst*, vol. 140, no. 4, pp. 1149–1154, 2015, doi: 10.1039/c4an02106a.
- [189] E. Yilmaz, D. Majidi, E. Ozgur, and A. Denizli, “Whole cell imprinting based *Escherichia coli* sensors: A study for SPR and QCM,” *Sensors and Actuators, B: Chemical*, vol. 209, pp. 714–721, 2015, doi: 10.1016/j.snb.2014.12.032.
- [190] N. Zaraee *et al.*, “Highly sensitive and label-free digital detection of whole cell *E. coli* with Interferometric Reflectance Imaging,” *Biosensors and Bioelectronics*, vol. 162, no. Who 2015, 2020, doi: 10.1016/j.bios.2020.112258.

- [191] M. Janik, M. Koba, A. Celebańska, W. J. Bock, and M. Śmietana, “Live E. coli bacteria label-free sensing using a microcavity in-line Mach-Zehnder interferometer,” *Scientific Reports*, vol. 8, no. 1, pp. 4–11, 2018, doi: 10.1038/s41598-018-35647-2.
- [192] M. Xu, R. Wang, and Y. Li, “Electrochemical biosensors for rapid detection of Escherichia coli O157:H7,” *Talanta*, vol. 162, no. August 2016, pp. 511–522, 2017, doi: 10.1016/j.talanta.2016.10.050.
- [193] H. M. Chen, K. R. Jheng, and A. D. Yu, “Direct, label-free, selective, and sensitive microbial detection using a bacteriorhodopsin-based photoelectric immunosensor,” *Biosensors and Bioelectronics*, vol. 91, no. November 2016, pp. 24–31, 2017, doi: 10.1016/j.bios.2016.12.032.
- [194] S. Brosel-Oliu *et al.*, “Novel impedimetric aptasensor for label-free detection of Escherichia coli O157:H7,” *Sensors and Actuators, B: Chemical*, vol. 255, pp. 2988–2995, 2018, doi: 10.1016/j.snb.2017.09.121.
- [195] L. Sun *et al.*, “Gold nanoparticles modified ZnO nanorods with improved photocatalytic activity,” *Journal of Colloid and Interface Science*, vol. 363, no. 1, pp. 175–181, 2011, doi: 10.1016/j.jcis.2011.07.005.
- [196] U. Siripatrawan, “Rapid differentiation between E. coli and Salmonella Typhimurium using metal oxide sensors integrated with pattern recognition,” *Sensors and Actuators, B: Chemical*, vol. 133, no. 2, pp. 414–419, 2008, doi: 10.1016/j.snb.2008.02.046.
- [197] S. M. Dizaj, F. Lotfipour, M. Barzegar-Jalali, M. H. Zarrintan, and K. Adibkia, “Antimicrobial activity of the metals and metal oxide nanoparticles,” *Materials Science and*

- Engineering C*, vol. 44, pp. 278–284, 2014, doi: 10.1016/j.msec.2014.08.031.
- [198] K. Siwińska-Stefańska *et al.*, “TiO<sub>2</sub>-ZnO binary oxide systems: Comprehensive characterization and tests of photocatalytic activity,” *Materials*, vol. 11, no. 5, pp. 1–19, 2018, doi: 10.3390/ma11050841.
- [199] M. Zhong, L. Chai, and Y. Wang, “Core-shell structure of ZnO@TiO<sub>2</sub> nanorod arrays as electron transport layer for perovskite solar cell with enhanced efficiency and stability,” *Applied Surface Science*, vol. 464, no. July 2018, pp. 301–310, 2019, doi: 10.1016/j.apsusc.2018.09.080.
- [200] S. Y. Yu *et al.*, “Fast electrochemical deposition of CuO/Cu<sub>2</sub>O heterojunction photoelectrode: Preparation and application for rapid cathodic photoelectrochemical detection of L-cysteine,” *Sensors and Actuators, B: Chemical*, vol. 290, no. March, pp. 312–317, 2019, doi: 10.1016/j.snb.2019.03.104.
- [201] T. M. Chen, G. Y. Xu, H. Ren, H. Zhang, Z. Q. Tian, and J. F. Li, “Synthesis of Au@TiO<sub>2</sub> core-shell nanoparticles with tunable structures for plasmon-enhanced photocatalysis,” *Nanoscale Advances*, vol. 1, no. 11, pp. 4522–4528, 2019, doi: 10.1039/c9na00548j.
- [202] J. F. S. Fernando *et al.*, “Photocatalysis with Pt-Au-ZnO and Au-ZnO Hybrids: Effect of Charge Accumulation and Discharge Properties of Metal Nanoparticles,” *Langmuir*, vol. 34, no. 25, pp. 7334–7345, 2018, doi: 10.1021/acs.langmuir.8b00401.
- [203] M. S. Diware *et al.*, “Ultrasensitive, label-free detection of cardiac biomarkers with optical SIS sensor,” *Biosensors and Bioelectronics*, vol. 87, pp. 242–248, 2017, doi: 10.1016/j.bios.2016.08.049.

- [204] R. S. Moirangthem, Y.-C. Chang, and P.-K. Wei, "Ellipsometry study on gold-nanoparticle-coated gold thin film for biosensing application," *Biomedical Optics Express*, vol. 2, no. 9, p. 2569, 2011, doi: 10.1364/boe.2.002569.
- [205] U. Pant, S. Mohapatra, and R. S. Moirangthem, "Total internal reflection ellipsometry based SPR sensor for studying biomolecular interaction," *Materials Today: Proceedings*, no. xxxx, pp. 1–4, 2020, doi: 10.1016/j.matpr.2020.01.602.
- [206] M. Varshney and Y. Li, "Interdigitated array microelectrode based impedance biosensor coupled with magnetic nanoparticle-antibody conjugates for detection of Escherichia coli O157:H7 in food samples," *Biosensors and Bioelectronics*, vol. 22, no. 11, pp. 2408–2414, 2007, doi: 10.1016/j.bios.2006.08.030.
- [207] Y. Wang, Z. Ye, and Y. Ying, "New trends in impedimetric biosensors for the detection of foodborne pathogenic bacteria," *Sensors*, vol. 12, no. 3, pp. 3449–3471, 2012, doi: 10.3390/s120303449.
- [208] Y. Chen *et al.*, "Synthesis of porous ZnO/TiO<sub>2</sub> thin films with superhydrophilicity and photocatalytic activity via a template-free sol-gel method," *Surface and Coatings Technology*, vol. 258, no. 2013, pp. 531–538, 2014, doi: 10.1016/j.surfcoat.2014.08.042.
- [209] A. M. Ferrari-Lima, R. P. De Souza, S. S. Mendes, R. G. Marques, M. L. Gimenes, and N. R. C. Fernandes-Machado, "Photodegradation of benzene, toluene and xylenes under visible light applying N-doped mixed TiO<sub>2</sub> and ZnO catalysts," *Catalysis Today*, vol. 241, no. PA, pp. 40–46, 2015, doi: 10.1016/j.cattod.2014.03.042.
- [210] J. Yang, Y. L. Jiang, L. J. Li, E. Muhire, and M. Z. Gao, "High-performance photodetectors and enhanced photocatalysts of two-dimensional TiO<sub>2</sub> nanosheets under UV light

- excitation,” *Nanoscale*, vol. 8, no. 15, pp. 8170–8177, 2016, doi: 10.1039/c5nr09248e.
- [211] D. Nunes *et al.*, “Enhanced UV Flexible Photodetectors and Photocatalysts Based on TiO<sub>2</sub> Nanoplatfoms,” *Topics in Catalysis*, vol. 61, no. 15–17, pp. 1591–1606, 2018, doi: 10.1007/s11244-018-0968-4.
- [212] O. Carp, C. L. Huisman, and A. Reller, “Photoinduced reactivity of titanium dioxide,” *Progress in Solid State Chemistry*, vol. 32, no. 1–2, pp. 33–177, 2004, doi: 10.1016/j.progsolidstchem.2004.08.001.
- [213] B. Tryba, M. Toyoda, A. W. Morawski, R. Nonaka, and M. Inagaki, “Photocatalytic activity and OH radical formation on TiO<sub>2</sub> in the relation to crystallinity,” *Applied Catalysis B: Environmental*, vol. 71, no. 3–4, pp. 163–168, 2007, doi: 10.1016/j.apcatb.2005.12.036.
- [214] C. T. Bot and C. Prodan, “Quantifying the membrane potential during E. coli growth stages,” *Biophysical Chemistry*, vol. 146, no. 2–3, pp. 133–137, 2010, doi: 10.1016/j.bpc.2009.11.005.
- [215] Y. Qiao, C. M. Li, S. J. Bao, Z. Lu, and Y. Hong, “Direct electrochemistry and electrocatalytic mechanism of evolved Escherichia coli cells in microbial fuel cells,” *Chemical Communications*, no. 11, pp. 1290–1292, 2008, doi: 10.1039/b719955d.
- [216] S. K. Tiwari, S. Bhat, and K. K. Mahato, “Design and Fabrication of Low-cost Microfluidic Channel for Biomedical Application,” *Scientific Reports*, vol. 10, no. 1, Jun. 2020, doi: 10.1038/s41598-020-65995-x.
- [217] M. Flegler and A. Neyer, “PDMS microfluidic chip with integrated waveguides for optical detection,” *Microelectronic*

*Engineering*, vol. 83, no. 4, pp. 1291–1293, 2006, doi:  
<https://doi.org/10.1016/j.mee.2006.01.086>.